Enhancing Long-Range Satellite-Based Entanglement Distribution through High-Dimensional Information Encoding

MSc Thesis
Marc Calvin Dijksman

Delft University of Technology

TU Delft

TU Delft

MSc thesis APPLIED PHYSICS

Enhancing Long-Range Satellite-Based Entanglement Distribution through High-Dimensional Information Encoding

MARC CALVIN DIJKSMAN
4677188

Delft University of Technology

Supervisors

Dr. J. Borregaard

V. Dominguez Tubio

Other committee members

Prof. Dr. S. Gröblacher

Dr. M. Blaauboer

13th June 2023

Delft

An electronic version of this thesis is available at: https://github.com/mcalvind/Master_Thesis_Calvin_Dijksman

Abstract

The distribution of multiple entangled pairs plays a vital role in various applications, such as quantum metrology, blind quantum computing, quantum key distribution, and quantum teleportation. While qubit-based protocols exist, they are often limited by short coherence times in quantum memories and the need for individual pair generation, leading to inefficiencies and reduced fidelity. To address these challenges, this thesis focuses on the development and analysis of a comprehensive theoretical framework for satellite-based entanglement distribution using high-dimensional qudits. By employing high-dimensional qudit encoding, which enables the simultaneous entanglement of multiple pairs, we aim to enhance the capacity and efficiency of entanglement distribution schemes.

The objectives of this research are twofold, first, to compare the performance of the qudit-based protocol with a similar qubit-based protocol, particularly in a satellite-based context, and second, to investigate the feasibility and potential advantages of employing high-dimensional qudit encoding for near-term long-range entanglement distribution. The theoretical framework encompasses various elements, including a single photon pair source, lossy transmission, mapping of qudit states to qubit memories, and heralding measurements.

Through various simulations, we evaluate the impact of different parameters on the performance of the proposed protocol. Our findings reveal that high-dimensional encoding significantly alleviates memory requirements, making it suitable for current technologies with low memory coherence times. Multiplexing techniques further enhance the achievable distances and transmission rates, highlighting their importance for realistic implementations. However, we note that higher-dimensional protocols introduce additional experimental challenges and errors, warranting further research and optimisation. Furthermore, we explore the effect of reducing dark count rates in detectors and analyse its influence on the overall performance. Our investigations underscore the need for substantial detector improvements, as current dark count probabilities are on the same order of magnitude as channel losses.

By advancing our understanding of satellite-based entanglement distribution using qudits, this research contributes to the development of practical and secure quantum communication networks. The results presented herein lay the groundwork for future advancements in quantum communication technologies, fostering the realisation of global-scale quantum networks.

Acknowledgements

I would first like to sincerely thank Assistant Prof. Dr. Johannes Borregaard for giving me the opportunity to work on a project within his research group. I would also like to express my admiration for his profound expertise and his remarkable ability to think on his feet. Johannes's ability to quickly analyse complex challenges and provide insightful solutions has been instrumental in advancing my research. His remarkable capacity to address problems with precision and creativity has not only facilitated my research progress but also inspired me to think critically and approach challenges with a similar mindset.

A special appreciation goes to Vicky, for her role as my day-to-day supervisor. Her willingness to brainstorm ideas, provide insightful feedback, and offer guidance at every step has been invaluable. I am grateful for her expertise, enthusiasm, and genuine commitment towards my thesis project. Working alongside Vicky has been a privilege, and I am truly fortunate to have had her as my supervisor. I'm very happy to have received this opportunity to conduct my Master's thesis research with such encouraging and patient supervisors. I would also like to thank the research group for providing an inspiring environment with a wide variety of projects and for the group discussions.

I extend my sincere appreciation to Prof. Dr. S. Gröblacher and Associate Prof. Dr. M. Blaauboer for their involvement as members of the assessment committee for this thesis. I would also like to thank Phoenix, for her unwavering support and understanding during this challenging and stressful period. Finally, I would like to express my gratitude towards my parents for supporting me with everything that I do and for making my academic development possible. Their encouragement and sacrifices have played a significant role in my academic journey, and I am forever grateful.

Thank you all for being a part of my academic and personal growth.

Contents

1 Introduction

In recent decades, quantum information science has emerged as a fascinating field with the potential to revolutionise various aspects of information processing, communication, and computation [1]. One of the fundamental elements of quantum information is entanglement, a unique property that allows the creation of non-classical correlations between distant quantum systems. Harnessing entanglement for practical applications is a key goal in the field of quantum communication [2]. Traditional quantum communication protocols primarily rely on qubits, which are two-level quantum systems, for encoding and transmitting information. However, information encoding using high-dimensional quantum systems called "qudits" can significantly increase the amount of information that can be encoded and transmitted per attempt.

The demand for multiple entangled pairs arises across various domains, encompassing quantum metrology for precise sensing ([3]), blind quantum computing ([4, 5]), quantum key distribution ([6],[7]), and quantum teleportation ([8, 9]), among others. In these applications, the distribution of entangled pairs plays a pivotal role, aiming to establish a global quantum network [10, 11]. While certain qubit-based protocols have been developed, they typically rely on a sequential ([12]) or parallel ([13, 14]) approach to individually generate entangled pairs. However, these methods are significantly impacted by the limited coherence times of quantum memories, as stored pairs must wait until all desired entangled pairs are successfully generated. The required coherence time of the quantum memories is therefore dependent on the transmission probability. To address this challenge, a protocol utilising high-dimensional qudit encoding to simultaneously entangle multiple pairs was introduced ([15, 16]). This novel approach forms the foundation of our thesis, where we aim to explore its advantages over qubit-based protocols within the context of a satellite-based scheme. By harnessing the power of high-dimensional encoding, we seek to overcome the limitations imposed by short coherence times and enable the distribution of entangled pairs over long distances. Our chosen encoding scheme is time-bin encoding, which allows for efficient manipulation and detection of qudits using well-established techniques [17]. This type of encoding offers inherent resilience against various types of noise during transmission. Moreover, the use of satellites in entanglement distribution offers an important advantage over terrestrial-based approaches as they can bypass the limitations imposed by optical fibres, such as high attenuation and loss [18], which leads to an exponential decrease in rate with distance. Satellites thus provide a platform for long-distance quantum communication, enabling the distribution of entangled qudits over global distances [19].

The primary objective of this thesis is to develop a comprehensive theoretical framework for satellite-based entanglement distribution using qudits in order to compare the performance of the protocol to a similar qubit-based protocol. We aim to investigate the feasibility and performance gain of employing higher-order information encoding to enhance the capacity of entanglement distribution schemes. To achieve this, we will delve into the mechanics of creating multiple entangled pairs at two different ground stations. The model consists of four main components: a single photon pair source, transmission, mapping the high-dimensional qudit state to a register of qubit memories, and a heralding measurement. While our goal is to provide a general model without assuming specific hardware, we will consider the use of a spontaneous parametric down-conversion (SPDC) source, which has shown promising experimental results. Notably, the experiment by Yin et al., demonstrated entanglement distribution over a ground distance of 1200 km [20]. For the transmission probability, we will utilise a model developed by Janice van Dam [21]. To implement the mapping of the qudit state to the memory register several possible hardware types will be proposed, although the analytical model will assume a perfect mapping. To ensure a non-invasive heralding measurement that avoids collapsing the entangled state into a non-entangled product state, we will employ a generalised X-measurement. In our analysis, we will assume the multi-mode quantum Fourier transform (QFT) interferometer to be perfect, providing accurate measurements. Incorporating different hardware options and refining the assumptions based on experimental implementations can lead to a more practical and realistic protocol with potentially fewer errors.

The simulations verify the anticipated alleviation of memory requirements through the use of high-dimensional encoding. This substantiates the recommendation to employ high-dimensional encoding for near-term long-range entanglement distribution, particularly when confronted with the constraints imposed by low memory coherence times associated with current technologies. By adopting a dimensionality that corresponds to the desired number of entangled pairs, the memories only need to retain

the entangled pairs for the duration of classical communication between two ground stations needed for the heralding step. However, it is important to note that the advantages of qudits diminish in scenarios with extended coherence times, especially when high-fidelity pairs are required. In our model, this observation primarily stems from the use of an SPDC source, which introduces additional errors when higher-dimensional encodings are employed. The simulations moreover demonstrate that the incorporation of multiplexing techniques enables the attainment of significantly longer distances, and to some extent, multiplexing becomes essential for practical implementations. It should be acknowledged that the realisation of a higher-dimensional protocol is likely to entail a more complex experimental setup and a higher susceptibility to errors due to the increased number of components involved. Furthermore, we explore the impact of reducing the dark count rate of detectors within our scheme. Our findings show that achieving significant results necessitates a substantial improvement in detector performance, as the current achievable dark count rate is still on the same order of magnitude as the channel loss. Enhancing detectors to achieve lower dark count rates is crucial for reducing errors and improving the overall fidelity of entanglement distribution.

Through our analysis and comparison with a qubit-based protocol, we aim to demonstrate the superiority of high-dimensional qudit protocols for long-range implementations with near-term hardware. Our study specifically focuses on the satellite-based paradigm, highlighting its immense potential for establishing robust quantum networks. By leveraging qudits and their inherent capabilities, we aim to push the boundaries of long-range entanglement distribution and pave the way for the practical implementation of satellite-based quantum networks. These networks hold the promise of revolutionising secure communication, enabling advanced quantum computing paradigms, and unlocking new frontiers in various scientific and technological domains. This research contributes to the growing body of knowledge in the field of quantum communication and aids in establishing a solid foundation for the practical implementation of satellite-based quantum networks using qudits. Through our efforts to combat lossy transmission and short coherence times, we strive to enable the distribution of high-fidelity entangled pairs at a high rate. By doing so, we aim to accelerate the development of secure and scalable quantum communication technologies, ultimately shaping the future of global communication and information exchange.

In the subsequent chapters, this thesis will unfold as follows. In §2 we will present the necessary theoretical background for modelling entanglement distribution. The model utilised for our simulations will be explained in detail in §3, while the results obtained will be presented in §4. In §5 we delve into a comprehensive discussion of our findings, offering insights into potential improvements, implementation methods, and avenues for future research. Finally, in §6, we will conclude the thesis with a concise recapitulation of the key findings. For further reference, the appendix includes additional information such as the pseudo-code (A.2), detailed calculations for a 4-dimensional qudit protocol demonstrating the creation of two entangled pairs (A.1), and a list of parameters (A.3).

For the interested reader, the full code used for the simulations in this thesis can be found at: https://github.com/mcalvind/Master_Thesis_Calvin_Dijksman.

2 Theory

In this section, the theoretical background for the method used in this thesis is presented. We begin by introducing the notations used throughout this thesis. Understanding entanglement is a fundamental part of this work so we will delve into this concept here. Additionally, the spontaneous parametric down-conversion (SPDC) source will be presented, a key component that enables the implementation of our entanglement protocol. Notably, previous experiments conducted with similar settings have successfully demonstrated the utility of this source [20, 22, 23]. The presence of loss in quantum communication systems necessitates careful consideration of the medium used for transmission. This leads us to consider the motivation behind the use of satellites over optical fibre while we discuss the modelling of photon transmission through free space and the atmosphere. Additionally, we discuss the process of mapping photonic qudits to quantum memories (QM) and the heralding of photon arrival. While we outline a possible implementation, it is important to note that there are multiple variations and setups that can be employed in practical applications. We conclude this section by explaining the phenomenon of decoherence, which significantly impacts the fidelity of our entangled pairs and plays a crucial role in our theoretical simulations. By providing a comprehensive theoretical foundation, this section sets the stage for the subsequent chapters, where we go into the simulation model and interpretation of the results.

2.1 Nomenclature

In quantum physics, we use a wave function to predict how systems behave. These wave functions depict the state of the system under consideration and provide the probabilities associated with various measurement outcomes. To describe states, we often utilise vectors, adopting a notation specific to the field of quantum mechanics known as the 'bra-ket' or Dirac notation. In this notation, we represent states using "kets", denoted as column vectors. For instance, $|0\rangle = \begin{pmatrix} 1 \\ 0 \end{pmatrix}$ represents the state labelled as "0". Conversely, we have "bras", which are represented as row vectors. For example, $\langle 0| = \begin{pmatrix} 1 & 0 \end{pmatrix}$ and can be considered as the complex conjugate of the corresponding "ket". This notation allows us to conveniently work with complex Hilbert spaces, where the vectors represent the different states of the system. By adopting the 'bra-ket' notation, we can effectively describe and manipulate quantum states within this framework. In quantum computation and information, we often use the analogy of classical computation as a template. Therefore, information is usually encoded in zeros and ones. This can be done by finding a physical system and constraining the possible states to only two, such that we have a two-level system. For photons two common realisations of such a two-level system is to use polarisation or time-bin encoding. In this thesis, we will moreover consider higher dimensional information encoding in the form of so-called qudits. These can be in more than two states, characterised by their dimensionality, and our choice of encoding will be time-bin encoding. The state $|l\rangle$ will thus denote that the photon is in the l-th time-bin. To take care of the fact that the source of entangled photons employed might send multi-photon pairs instead of single-photon pairs we will write such a state in the Fock basis as $|n\rangle_l$ where n tells us the number of photons present and l denotes the time-bin.

If we are talking about a system of multiple individual quantum objects we can describe them using one 'ket' as follows: $|\Psi\rangle_{A,B} = |\psi_A, \psi_B\rangle = |\psi_A\rangle \otimes |\psi_B\rangle$, where $|\psi_A\rangle$ and $|\psi_B\rangle$ denote the states that objects A and B are in, respectively. Throughout this thesis, we will sometimes refer to A and B as Alice and Bob as is the usual convention in quantum physics.

Up till now, we have considered pure states, meaning that we know the precise state of a system. If the state of a system is in some mixed state determined by a statistical ensemble of various states we will need a different representation, namely the density matrix. A density matrix is defined by:

$$\rho = \sum_j p_j \, |\psi_j\rangle \, \langle \psi_j| \, . \tag{2.1}$$

The diagonal terms of this equation tell us the probabilities to be in any state and the off-diagonal terms express information about coherence or quantum correlations between different states. These arise when superpositions exist between basis states or there is entanglement. When a state is in a superposition it means that a system can coexist in multiple basis states at the same time. The meaning of entanglement

will be explained further in this section in §2.2. The density matrix is non-unique and depends on the choice of basis, in one basis a state might be in a superposition while in another it might not. For instance, if we look at the following state: $\frac{1}{\sqrt{2}}(|0\rangle + |1\rangle)$, this can be represented in the X-basis as $|+\rangle$ while $\frac{1}{\sqrt{2}}(|0\rangle - |1\rangle)$ can be represented by $|-\rangle$, forming an orthogonal basis to the common computational basis. A density matrix can be used to describe the general state of any quantum system and allows for the calculation of the outcomes of any measurement performed on this system. If the state is pure it is straightforwardly represented by:

$$\rho_{pure} = |\psi\rangle \langle\psi| . \tag{2.2}$$

The purity, given by $\mathrm{Tr}(\rho^2) \leq 1$, provides a measure of how pure a state is. If $\mathrm{Tr}(\rho^2) = \mathrm{Tr}(\rho) = 1$, we are dealing with a pure state, while for mixed states this value is less than 1.

In this thesis, we focus on a satellite-based entangled photon source situated at a midpoint. To provide a visual representation, we show the single satellite downlink setup considered in this thesis in Fig. 2.1. Some of the parameters that will be used later on in the model are also illustrated. Considering this isosceles triangle allows for ease of calculations, although different arm lengths could be considered as well.

Additionally, a list of parameters and their meaning can be found in Appendix 3.

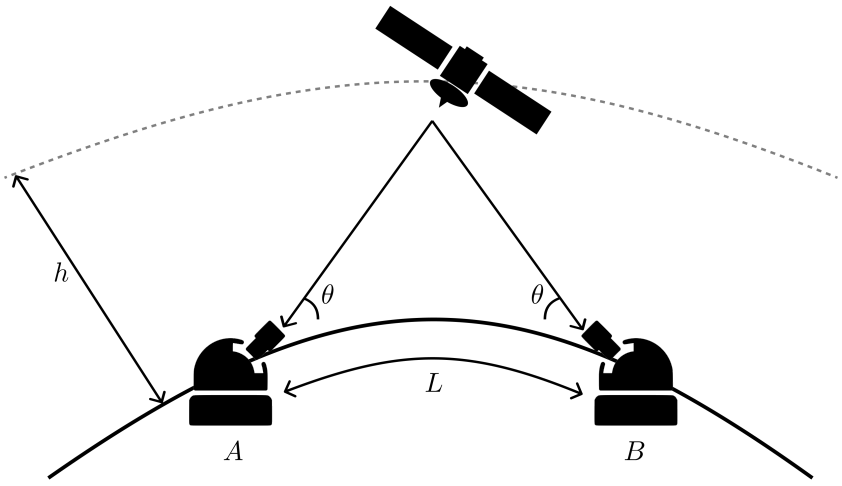

Fig. 2.1: Visual representation of the overall setup considered in this thesis. Note that we consider a midpoint satellite such that both arms of the transmitted entangled photons are equal in length as indicated by the equal angles θ. We denote the ground distance between Alice and Bob by L and the height of the satellite by h.

2.2 Entanglement

If the quantum state of an individual part of a multipartite quantum system becomes correlated in such a way that it can not be described separately without mentioning the others, we call them entangled. This correlation is characterised by a mathematical entangled state, where the properties of the individual particles are intertwined, leading to a non-separable composite system. Let us consider the following two-qubit state: $|\Psi\rangle_{A,B} = \frac{|00\rangle_{A,B} + |11\rangle_{A,B}}{\sqrt{2}}$. This state has the remarkable property that it cannot be written in a product state, that is, no individual single qubit states for Alice and Bob can be found such that $|\Psi\rangle_{A,B} = |a\rangle \otimes |b\rangle$ if this is the case for any two-qubit state we call it entangled [2]. The entangled state exhibits unique features, such as non-locality and non-classical correlations, which defy classical intuitions and play a crucial role in various applications, including quantum information processing [24], quantum communication [6, 7], and quantum computing[25]. Let us consider two entangled qubits. If we perform measurements on them we will find that we get correlated outcomes. A generally accepted way to determine entanglement in an experiment is by checking whether the CHSH is violated (as in the paper by Hensen et al.[26]) or using another variation of a Bell test. In such tests, correlations are

measured and compared with the maximum possible amount of correlation that a classical theory can provide. If this is exceeded it can generally be appointed to quantum effects.

Entanglement can be viewed as a real physical resource and as such should be quantifiable. In other words, entanglement can be stronger or weaker. Multiple entanglement measures exist that can tell us how strong the entanglement is. If we can transform the pure state of a two-qudit system by only using local unitary transformations to

$$\left|\Psi_d^+\right\rangle = \frac{|0,0\rangle + |1,1\rangle + \cdots + |d-1,d-1\rangle}{\sqrt{d}}, \tag{2.3}$$

then the state is maximally entangled [27]. If, on the other hand, a state is separable there is no entanglement. Any measure of entanglement for a pure state $|\psi\rangle\langle\psi|$ reduces to the entropy of entanglement $E(|\psi\rangle\langle\psi|) \coloneqq S(\mathrm{Tr}_A |\psi\rangle\langle\psi|) = S(\mathrm{Tr}_B |\psi\rangle\langle\psi|)$, where $S(\rho) = -\mathrm{Tr}(\rho \log_2 \rho)$. For mixed states, there is no universal measure of entanglement and it becomes a bit more tricky to compute [27]. The target state in this thesis will be a pure state however.

When an entangled pair undergoes quantum operations and is exposed to the environment during transmission and storage, it is expected that the entanglement may undergo changes, particularly if decoherence occurs due to undesired interactions with the environment. To assess the preservation of our entangled pair after these operations, we employ fidelity as a metric, defined as:

$$F = \langle\psi| \rho |\psi\rangle, \tag{2.4}$$

where $|\psi\rangle$ denotes the maximally entangled target state and ρ represents the density matrix of our system after all operations. The fidelity provides a quantification of the similarity between the original and final states, offering insight into the extent of entanglement preservation. In this thesis, we use a Bell state as the target state. There are four Bell states which are each maximally entangled and form the basis of a 4-dimensional Hilbert space of 2 qubits. The Bell states are given by:

$$\begin{aligned}
\left|\Phi^+\right\rangle &= \frac{1}{\sqrt{2}}(|00\rangle + |11\rangle) \\
\left|\Phi^-\right\rangle &= \frac{1}{\sqrt{2}}(|00\rangle - |11\rangle) \\
\left|\Psi^+\right\rangle &= \frac{1}{\sqrt{2}}(|01\rangle + |10\rangle) \\
\left|\Psi^-\right\rangle &= \frac{1}{\sqrt{2}}(|01\rangle - |10\rangle)
\end{aligned} \tag{2.5}$$

We will use $|\Phi^+\rangle$ as the target state in our protocol, but any of the four Bell states could in principle be obtained by applying minor changes to the protocol.

2.3 Spontaneous parametric down-conversion

In this thesis, spontaneous parametric down-conversion (SPDC) is used as an entangled photon source. SPDC sources have gained popularity in experiments as a reliable method for generating entanglement. Notably, the Micius satellite used by Yin et al. ([20]) in their state-of-the-art experiments employs this type of source. One of the advantages of SPDC setups is their ability to operate at room temperature, making them practical and accessible for various applications. Additionally, the components of SPDC setups can be easily modified to explore different experimental scenarios. Considering these factors, it seems sensible to incorporate SPDC as the source in our theoretical model, allowing us to align with previous experiments conducted using similar satellite setups. It must be noted that although we chose to use the SPDC source alternative entangled photon sources may be employed.

The phenomenon of spontaneous parametric down-conversion arises from the action of a squeezing operator on vacuum modes. In the context of three-wave mixing, this process generates what is known as two-mode squeezed vacuum states (TMSV). Such squeezed vacuum states are obtained by pumping

a nonlinear crystal during the SPDC process. In the photon number basis, the two-mode squeezed vacuum state resulting from pumping the non-linear crystal can be represented as [28]:

$$|\Psi\rangle = \sqrt{1-\lambda^2}\sum_{n=0}^{\infty}\lambda^n |n,n\rangle\,, \tag{2.6}$$

where $\lambda \in (0,1)$ denotes the squeezing parameter. The generation of the TMSV state results from the interaction with the second-order nonlinearity present in certain optical materials, which is described by the corresponding susceptibility, $\chi^{(2)}$. The Hamiltonian governing the down-conversion can be expressed as [29]:

$$\hat{H} = \hbar\omega_a \hat{a}^\dagger\hat{a} + \hbar\omega_b \hat{b}^\dagger\hat{b} + \hbar\omega_p \hat{c}^\dagger\hat{c} + i\hbar\chi^{(2)}(\hat{a}\hat{b}\hat{c}^\dagger - \hat{a}^\dagger\hat{b}^\dagger\hat{c}), \tag{2.7}$$

where $\hat{a}$ and $\hat{b}$ represent the annihilation operators for the signal and idler modes, respectively, $\hat{c}$ represents the annihilation operator for the pump field, and ω_a, ω_b, and ω_p denote the corresponding frequencies. We can now make the parametric approximation where we assume the pump field to be in a strong coherent classical field $\gamma e^{i\omega_p t}$, which is strong enough to remain undepleted of photons over the relevant time scale. Neglecting constant terms, we can approximate the operators $\hat{c}$ and $\hat{c}^\dagger$ by $\gamma e^{-i\omega_p t}$ and $\gamma e^{i\omega_p t}$, respectively. Consequently, the Hamiltonian can be expressed as:

$$\hat{H}^{(PA)} = \hbar\omega_a \hat{a}^\dagger\hat{a} + \hbar\omega_b \hat{b}^\dagger\hat{b} + i\hbar(\eta^* e^{i\omega_p t}\hat{a}\hat{b} - \eta e^{-i\omega_p t}\hat{a}^\dagger\hat{b}^\dagger) \tag{2.8}$$

where $\eta = \chi^{(2)}\gamma$. In this parametric approximation, the interaction term characterises the down-conversion process, with η representing the effective coupling strength between the signal and idler modes induced by the second-order nonlinearity and the amplitude of the pump field.

In the interaction picture where we adjust the pump field frequency such that $\omega_p = \omega_a + \omega_b$ obtaining the time-independent interaction Hamiltonian

$$\hat{H}_I = i\hbar(\eta^*\hat{a}\hat{b} - \eta\hat{a}^\dagger\hat{b}^\dagger). \tag{2.9}$$

Through this process, a single pump beam photon can be converted into two optical photons in two spatially separated modes which are historically referred to as the "signal" and "idler" beams (although their names are arbitrary, see Fig.2.2). The initial state of the system, where the pump beam has many photons and the signal and idler modes are in vacuum states, undergoes the following conversion:

$$|n\rangle_p |0\rangle_s |0\rangle_i \implies |n-1\rangle_p |1\rangle_s |1\rangle_i\,. \tag{2.10}$$

Since the signal and idler modes were initially in vacuum states we call this process "spontaneous".

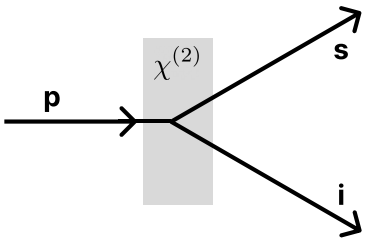

Fig. 2.2: Schematic showing how the pump beam is split into two separate signal and idler beams with spatial separation.

Some conditions must be satisfied for the down-conversion process to occur, specifically, we must have a conservation of energy and of momentum.

$$\hbar\omega_p = \hbar\omega_s + \hbar\omega_i \tag{2.11}$$

$$\hbar\mathbf{k}_p = \hbar\mathbf{k}_s + \hbar\mathbf{k}_i \tag{2.12}$$

These are called the *phase matching* requirements. Several techniques exist for obtaining this phase matching and their implementation depends on the intended application. For our purpose, the exact

experimental details are not required. Instead, we will focus on the general output of the TMSVS, given by Eq. 2.6, in our simulations. Mathematically, we can represent the process by allowing the vacuum signal and idler states to evolve under the influence of the interaction Hamiltonian described in Eq. 2.9. The state vector evolves according to the well-known evolution

$$|\Psi((t)\rangle = e^{-it\hat{H}_I/\hbar} |0\rangle_s |0\rangle_i . \tag{2.13}$$

This can be expanded up to the second order in time to arrive at the approximate state:

$$|\Psi(t)\rangle \approx \left[1 - it\hat{H}_I/\hbar + \frac{1}{2}(-1t\hat{H}_I/\hbar)^2\right] |0\rangle_s |0\rangle_i . \tag{2.14}$$

After some derivations we arrive at the approximate expression for the two-mode squeezed state:

$$|\Psi(t)\rangle \approx \sqrt{1-\lambda^2}\left[|0\rangle_s |0\rangle_i + \lambda |1\rangle_s |1\rangle_i + \lambda^2 |2\rangle_s |2\rangle_i + \mathcal{O}(\lambda^3)\right] . \tag{2.15}$$

Where λ represents the interaction parameter and controls the amount of squeezing. If we consider $\lambda \in (0, 0.1)$ we know that less than 1% of all emission events will contain more than one photon pair and it can therefore be considered a good pumping regime for our purposes. The truncation error that emerges from neglecting higher-order terms will also be bounded by $1 - (1-\lambda^2)(1+\lambda^2+\lambda^4)$ which is smaller than 10^{-6} for $\lambda < 0.1$.

Following a similar setup to the paper by Brendel et al. [30] we can produce time-bin entangled photons. We start with a pump laser to send a short pulse. In their implementation, the pulse is coupled to a Mach-Zehnder interferometer to create two well-separated individual pulses. A delay loop is then used to make the two pulses indistinguishable, thus forming a superposition $\alpha |E\rangle + \beta |L\rangle$ as shown in Fig. 2.3. Here $|\alpha| + |\beta| = 1$ and $|E\rangle$ and $|L\rangle$ represent early and late time-bins respectively.

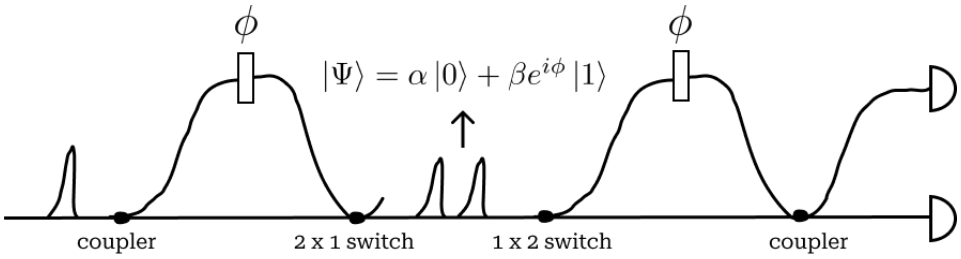

Fig. 2.3: Schematics of how to use a laser source and an unbalanced interferometer to make a coherent superposition of time-bin encoded qubits.

For our purpose, we could use a more straightforward way to implement time-bin entanglement by using a pulsed pump laser that sends pulses at a certain frequency defining the different time bins, $\frac{1}{\sqrt{2^m}} \sum_{l=0}^{2^m-1} |\psi_p\rangle_l$, where l denotes the time bin of the emitted state and 2^m represents the dimension of the qudit. The nonlinear crystal will be pumped with pulses at these different time bins to generate the time-bin entangled TMSV states that can be guided towards the two ground stations. The ideal state that we want to produce by using this source is represented by:

$$\frac{1}{\sqrt{2^m}} \sum_{l=0}^{2^m-1} |1_s\rangle_l |1_i\rangle_l . \tag{2.16}$$

However, the source is not ideal since it emits nothing with the largest probability and there is also a small probability of unwanted higher-order emissions as shown in Eq. 2.15. Hence, after pulsing the nonlinear crystal in different time bins defining the qudit, the full state can be represented by:

$$\begin{aligned} |\Psi\rangle_{A,B} &= \bigotimes_{l=0}^{2^m-1} \sqrt{1-\lambda^2} \sum_{n=0}^{\infty} \lambda^n |n_l, n_l\rangle_{A,B} \\ &\approx (1-\lambda^2)^{2^{m-1}} \left[|0,0\rangle_{A,B} + \lambda \sum_{l=0}^{2^m-1} |1_l, 1_l\rangle_{A,B} + \lambda^2 \sum_{l=0}^{2^m-1} \sum_{j\geq l}^{2^m-1} |1_l 1_j, 1_l 1_j\rangle_{A,B} + \mathcal{O}(\lambda^3)\right]. \end{aligned} \tag{2.17}$$

Here the subscripts l and j denote the time bins that the states are in. The photons that arrive at the receiver stations will be coupled to a memory register consisting of qubit memories and will then be measured by a generalised X measurement to herald the successful arrival at both stations as shown in Fig. 2.4. This will be explained in more detail in §2.5. Of course, more pulses can be sent and more interferometers and delay loops could be used to interfere a higher dimensional superposition of time bins. This high-dimensional encoding will be the basis of the time-bin qudit used in our entanglement distribution protocol. Since we use time bins as our qudit space and their coherence is formed by carefully controlling the timing of the pump laser pulses to ensure that they are well-separated, there is no restriction on the coherence of the laser pulse and thus any standard laser can be used [30]. As one can imagine, the size and weight of the payload on a satellite are very restricted. Compact sources may present additional challenges to the implementation of the protocol, however, these can be met by state-of-the-art designs [31].

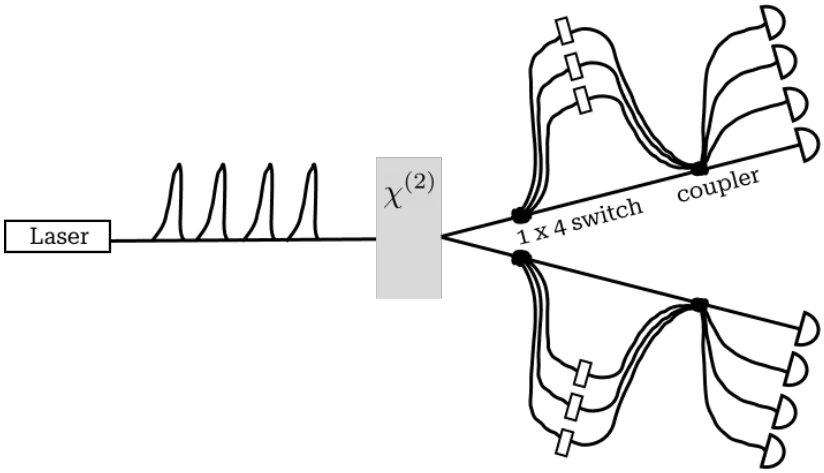

Fig. 2.4: Schematic of the proposed setup for a 4-dimensional qudit. Four well-separated pulses are sent by the laser defining the different time-bins. After interaction with the nonlinear crystal the signal and idler beams are spatially separated and individually sent to the two ground stations. There the different pulses are coupled to the memory register, made indistinguishable by different delay loops and measured in the X-basis. This setup can be generalised for higher dimensional qudits by adding more interferometers.

2.4 Loss

During the transmission of photonic quantum information, the photons are plagued by interactions with the environment that can lead to the complete loss of photons. In fibre-based transmission, the loss is so high even that it is considered infeasible to create a global quantum network solely using optical fibres. The loss of photons in optical fibre scales exponentially with the transmission distance. In a recent experiment, Wengerowsky et al. reported the optical fibre deployed distribution of polarisation entanglement over a distance of 192 km [32]. Long-distance fibre-based photonic time-bin entanglement has also been experimentally shown by Inagaki et al., where they even reported entanglement over a distance of 300 km [33]. Although, it must be noted that their rate was very low and to reach a secret key rate of 1 bit/s they could only reach 220 km even though they used a GHz frequency source. Furthermore, they used a midpoint source and thus each photon only has to travel half the distance. The lowest loss reported for optical fibres is 0.142 dB/km [18]. In classical communication, this loss is circumvented by the use of amplifiers, but due to the no-cloning theorem such amplification of quantum states is impossible using similar technology [34]. Either quantum repeaters can be used or another mode of transport with lower loss must be considered to obtain entanglement at large terrestrial distances. Satellite-based communication provides such a low loss medium as demonstrated by the low total loss of only 0.053 dB/km for the entanglement distribution over 1200 km by Yin et al. [20]. The loss in free

space is dominated by the divergence of light beams and therefore scales quadratically with distance instead of exponentially. Once the photons pass through the atmosphere the loss becomes exponential again [11]. This can be modelled by taking into account factors such as scattering, absorption by atmospheric constituents and the path length of the light through the atmosphere [35]. Luckily the atmospheric transmission only constitutes the final 10-20 km of the total transmission distance and is therefore not very dominant compared to the diffraction in free-space [11, 36]. Additionally, the distance for transmission through satellites is limited by their line of sight, higher satellites can thus transmit further, but at a lower rate due to more losses. A good balance must therefore be struck. The complete modelling of this transmission is very complex and hence we choose to model the loss as a beam splitter with a certain probability of transmittance. We utilise the model by Janice van Dam [21], to find the suitable transmission probability, denoted as p_T, for the distance between ground stations and the height of the satellite considered. This model takes into account many of the intricacies of space-based optical communication, including the effects of beam diffraction, pointing error, atmospheric turbulence, and absorption.

In modelling the loss using a beam splitter we also take into account the loss that occurs at the detector due to the detector's efficiency, we denote this efficiency as η. The basic beam splitter that we use to model the loss can be expressed in terms of creation and annihilation operators as follows:

$$a^\dagger |0\rangle \xrightarrow{\not\quad p_T\eta} \left(\sqrt{p_T\eta}a^\dagger + \sqrt{1-p_T\eta}l^\dagger\right)|0\rangle, \tag{2.18}$$

where the photon is either detected with a probability given by $p_T\eta$ or it is lost during transmission or detection. The detection efficiency is set to 0.5 which is found to be realistically achievable [37]. Moreover, for efficient collection of the photons transmitted by the satellite at both ground stations, a setup akin to the one used in Ref.[20] could be adopted. In their experiments, a high-precision acquiring, pointing and tracking (APT) technology was utilised to enhance the link efficiency. This APT system involves two beacon lasers of different wavelengths pointing at each other. This configuration enables precise alignment of the entangled signal beams with their respective receiving telescopes, thereby significantly boosting the link efficiency.

2.5 Mapping to memory and heralding

For the detection and mapping to the memory, we will use an adaptation to the method outlined in Ref. [15]. The protocol is based on storing the incoming time bin photons by flipping stationary qubit memories at both receivers [38]. We will mathematically provide the high-level protocol here. The time-bin entangled qudit source sends a state ideally represented by:

$$|\Psi\rangle = \frac{1}{\sqrt{2^m}} \sum_{l=0}^{2^m-1} |l\rangle_A |l\rangle_B , \tag{2.19}$$

where the two single photons traverse separate paths corresponding to the two arms of the isosceles triangle that is formed between the two ground stations and the satellite and l again denotes the time bin. The time-bin qudits are then first collected at the two ground stations and switched to interact with the qubit memories. The switching occurs according to the binary encoding of the high-dimensional time bin qudit. The decimal encoding of the single 2^m-dimensional qudits will thus be transformed into the corresponding binary encoding of m qubits to determine the switching pattern. A 2^m-dimensional qudit state represented by $|l\rangle$ ($l = 0, 1, \ldots, 2^m - 1$) can be changed to binary encoding by the following conversion: $[l]_{10} = [l_{m-1} \cdots l_k \cdots l_1 l_0]$. The number 5_{10} will for example be mapped to 101_2 in binary encoding. The m-qubit register will be initialised in the $|0\rangle^{\otimes m}$ state and the photon will be switched to flip the qubits corresponding to the binary encoding as depicted in Fig. 2.5, where the control nodes represent the switches. Many different types of hardware can be used here as long as the photonic qudit information can be stored in multiple qubits for a long time and the interface must enable the hybrid coupling between the photon and the qubit memory of choice. The resulting state after mapping the photonic qudit state to the memory qubits at both ground stations is given by:

$$|\psi\rangle = \frac{1}{\sqrt{2^m}} \sum_{l=0}^{2^m-1} |l\rangle_{A,ph} |l\rangle_{B,ph} |1_l\rangle_A |1_l\rangle_B , \tag{2.20}$$

where $|1_l\rangle = |l_{m-1}\rangle\,|l_{m-2}\rangle\cdots|l_1\rangle\,|l_0\rangle$, which represents the state of the multi-qubit register in binary encoding. The memory register should encode the same state as the incoming qudit state.

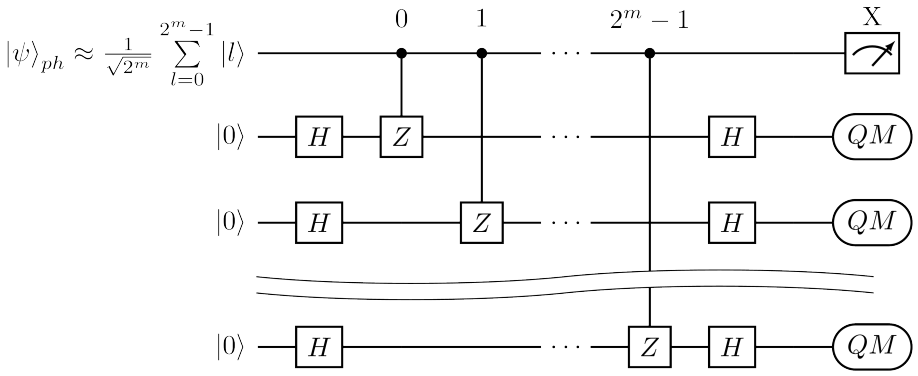

Fig. 2.5: Quantum circuit illustrating a plausible implementation of the protocol at one ground station. This implementation is identical at both receiving ends of the entanglement distribution protocol. The control nodes represent optical switches that route the incoming time-bin pulses to the corresponding quantum memories based on their binary encoding. These memories store the pulses after undergoing an entangling gate, such as the CZ-gate shown here. To remain in the computational basis, Hadamard gates are applied. After interaction at both ground stations, the incoming photons are subjected to a final X-basis measurement, which serves to herald the arrival of a photonic qudit while erasing the photonic information. This measurement projects the quantum memories onto multiple Bell pairs.

After mapping the qudit information to the memory register the photonic qudit undergoes the quantum Fourier transform (QFT) to facilitate a generalised X-basis measurement. In order to perform this QFT the photonic qudit is first switched towards different optical paths corresponding to each specific time bin. To align all time bins to the same temporal mode, the length of the delay loop traversed by each time bin photon is inversely proportional to its time bin number. Earlier time bins, with lower bin numbers, will thus pass through longer delay loops, while the latest time bin avoids any delay loop altogether. The time-bin encoding has then been converted into a spatial-mode encoding allowing us to use a multi-mode interferometer to interfere the various spatial states implementing a quantum Fourier transform as shown in Fig. 2.6 [39–43]. The multi-mode QFT matrix is defined by:

$$QFT = \frac{1}{\sqrt{2^m}} \begin{bmatrix} 1 & 1 & 1 & \dots & 1 \\ 1 & \omega & \omega^2 & \dots & \omega^{2^m-1} \\ 1 & \omega^2 & \omega^4 & \dots & \omega^{2(2^m-1)} \\ \vdots & \vdots & \vdots & \ddots & \vdots \\ 1 & \omega^{2^m-1} & \omega^{2(2^m-1)} & \dots & \omega^{(2^m-1)(2^m-1)} \end{bmatrix}, \tag{2.21}$$

where $\omega = e^{2i\pi/2^m}$.

After this, they are detected in an X-basis measurement, deleting the photonic information and subsequently projecting the spin states to the Bell state (up to some correctable phases). This measurement technique serves to confirm the arrival of the photon without extracting its specific time-bin information, thereby avoiding the collapse of the state of the two m-qubit registers into a non-entangled product state. The X-measurement basis resulting from the QFT can be described as:

$$|X_k\rangle = \frac{1}{\sqrt{2^m}} \sum_{l=0}^{2^m-1} \omega^{kl}\,|l\rangle\,. \tag{2.22}$$

The set $|X_k\rangle$ for $k \in \{0, 1, \dots, 2^m - 1\}$ forms a complete, orthogonal basis with respect to the original time-bin encoding. To perform the measurement after applying the QFT to the photon at both ground

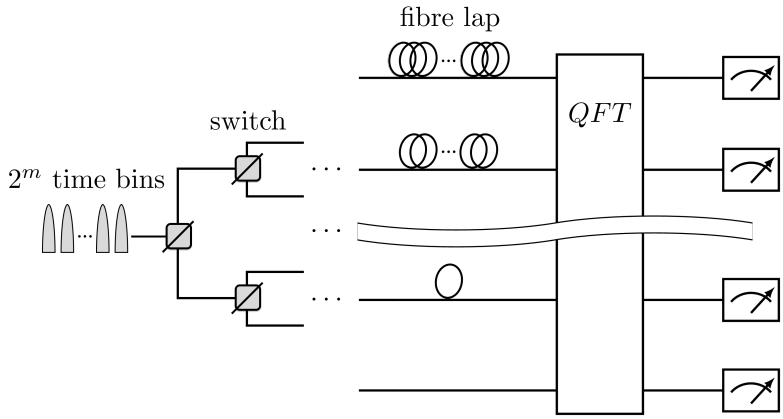

Fig. 2.6: The scheme showing a proposed implementation of the X-basis measurement on the time-bin photonic qudit. Switches route the time-bins to different spatial modes where they are subjected to a number of fibre laps inversely proportional to their time-bin number. This converts the temporal mode qudit into a spatial mode qudit allowing us to apply a multi-mode interferometer to interfere the different spatial states, hence implementing a quantum Fourier transform (QFT). Note that this requires the use of $2^m - 1$ optical switches, while the QFT will even require $m2^{m-1}$ beam splitters in the most straightforward setup.

stations, we write the qudit state in this orthogonal basis:

$$|\psi'\rangle = \frac{1}{2^{3m/2}} \sum_{l=0}^{2^m-1} \sum_{k=0}^{2^m-1} \sum_{m=0}^{2^m-1} \omega^{-klm} |X_k\rangle_{A,ph} |X_m\rangle_{B,ph} |1_l\rangle_A |1_l\rangle_B . \tag{2.23}$$

The photonic qudits are then measured in this basis on both sides. If the measurement outcome is $|X_k\rangle_A \otimes |X_m\rangle_B$ we have successfully erased the photonic information and the memory registers will be projected onto:

$$\begin{aligned} |\psi_{k,m}\rangle &= \sum_{l=0}^{2^m-1} \omega^{-klm} |1_l\rangle_A |1_l\rangle_B \\ &= \sum_{l=0}^{2^m-1} \omega^{-klm} |l_{m-1} \cdots l_k \cdots l_1 l_0\rangle_A |l_{m-1} \cdots l_k \cdots l_1 l_0\rangle_B \end{aligned} \tag{2.24}$$

Which can be reordered to:

$$\begin{aligned} |\psi_{k,m}\rangle = &\frac{1}{\sqrt{2^m}} \big(|0\rangle_A |0\rangle_B + \omega^{-km} |1\rangle_A |1\rangle_B\big) \otimes \big(|0\rangle_A |0\rangle_B + \omega^{-2km} |1\rangle_A |1\rangle_B\big) \otimes \\ &\big(|0\rangle_A |0\rangle_B + \omega^{-4km} |1\rangle_A |1\rangle_B\big) \otimes \cdots \otimes \big(|0\rangle_A |0\rangle_B + \omega^{-2^{m-1}km} |1\rangle_A |1\rangle_B\big). \end{aligned} \tag{2.25}$$

The additional phases can be corrected at both stations by applying single-qubit RZ-gates on the corresponding memory qubits. After applying these phase corrections we retrieve the Bell states that we set out to distribute:

$$|\psi\rangle = \frac{1}{\sqrt{2}} \Big(|0\rangle_A |0\rangle_B + |1\rangle_A |1\rangle_B\Big)^{\otimes m}. \tag{2.26}$$

The fidelity of the entangled pairs that we will find when using our erroneous SPDC source and after the lossy transmission and detection will not be perfect. How we model this to find the fidelity is explained in §3.

To implement the protocol described above many different types of hardware might be used that possess the required functionalities. Some memory candidates include using trapped atoms [44–46], spin qubits in a quantum dot [47] or solid-state qubits [48] which can even be used to couple to a long-lived neutron

spin allowing coherence times of up to a minute [49]. These memory candidates can all be trapped inside a cavity system to enable the optical interactions needed to perform the spin-photon entangling gates [50–52]. The entangling gate between the memory qubits and the photonic qudits can be done inside one-sided optical cavities, where a controlled phase gate can flip the state $|+\rangle \rightarrow |-\rangle$. We could therefore alternatively initialise our quantum memories in the $|+\rangle$ state and create Bell states in the X-basis, thereby requiring fewer gates. Or we apply the Hadamard gates as shown in Fig. 2.5 to stay in the computational basis. Additionally, a multitude of detectors can be used in principle, we will consider the general case of non-number resolving detectors. However, if photon number resolving detectors are utilised a post-selection process can be used to decrease the error caused by multi-photon pairs emitted from our imperfect source. Our primary aim is, however, to evaluate the performance of the qudit protocol in comparison to the qubit protocol. Therefore, the eventual hardware choice is considered to be of minor importance in our simulations, as long as it does not introduce an unfair advantage to either protocol.

2.6 Decoherence

Decoherence is a fundamental concept in quantum physics, referring to the loss of coherence and quantum properties over time as a system interacts with the environment. In the quantum realm, particles can exist in multiple states simultaneously, thanks to the phenomenon of superposition. Coherence refers to the ability of these states to maintain their integrity and evolve in a predictable and undisturbed manner. However, when a quantum system interacts with its environment, such as through random interactions with other particles or electromagnetic fields, the delicate quantum nature becomes entangled with the environment, leading to decoherence. The stored quantum states in the quantum memories also suffer from such unwanted interactions with the environment. Therefore, they degrade over time, making it challenging to maintain the quantum information accurately.

Since the decoherence in the quantum memory leads to a degradation of entanglement it is important to model this effect when calculating the fidelity of our entangled pairs. Many models exist to describe decoherence, some common models include the depolarising channel, amplitude damping channel and the phase damping channel [2]. Each of these models captures different aspects of decoherence and types of noise. The phase damping channel describes a loss of quantum information without loss of energy, for example by random scattering or interaction with distant electrical charges that result in an accumulation of a phase. The amplitude damping channel, on the other hand, might be used to describe energy dissipation due to for instance spontaneous emissions or attenuation of photons in a cavity. Considering both amplitude and phase damping channels it is possible to accurately describe specific decoherence processes. A more general form of noise or decoherence affecting all aspects of the quantum state can be represented by a depolarising channel. This channel is commonly used to capture the overall loss of coherence without the knowledge of the specific underlying cause. The depolarising channel encompasses a broad range of noise sources and describes an extreme form of decoherence where all coherence is destroyed and the system becomes completely mixed. The actual decoherence of the model could be more complex and nuanced, but assuming a depolarising channel can represent a worst-case scenario.

In our case, the hardware used is not specifically known, let alone the specific details of the decoherence mechanism that will affect the stored quantum information. Therefore, the choice of a more general and robust description of decoherence seems in place. The depolarising channel will thus be the model of choice, simultaneously providing a more general and computationally simpler implementation of the noise model. In the description of the decoherence of stored qubits, we are after the fidelity of our entangled pairs compared to the target state. We thus need to apply the depolarising channel to both of the memory qubits to capture their decoherence. A general decoherence channel for two qubits can be described as follows:

$$\begin{aligned}\bar{\rho} = \quad & p_1p_2\rho + p_2(1-p_1)[\epsilon_x(\mathbb{X}\otimes\mathbb{1})\rho(\mathbb{X}\otimes\mathbb{1}) + \epsilon_y(\mathbb{Y}\otimes\mathbb{1})\rho(\mathbb{Y}\otimes\mathbb{1}) + \epsilon_z(\mathbb{Z}\otimes\mathbb{1})\rho(\mathbb{Z}\otimes\mathbb{1}) + \epsilon_1\rho] \\ & + p_1(1-p_2)[\epsilon_x(\mathbb{1}\otimes\mathbb{X})\rho(\mathbb{1}\otimes\mathbb{X}) + \epsilon_y(\mathbb{1}\otimes\mathbb{Y})\rho(\mathbb{1}\otimes\mathbb{Y}) + \epsilon_z(\mathbb{1}\otimes\mathbb{Z})\rho(\mathbb{1}\otimes\mathbb{Z}) + \epsilon_1\rho] \\ & + (1-p_1)(1-p_2)[\epsilon_x^2(\mathbb{X}\otimes\mathbb{X})\rho(\mathbb{X}\otimes\mathbb{X}) + \epsilon_x\epsilon_y(\mathbb{Y}\otimes\mathbb{X})\rho(\mathbb{Y}\otimes\mathbb{X}) + \epsilon_x\epsilon_z(\mathbb{Z}\otimes\mathbb{X})\rho(\mathbb{Z}\otimes\mathbb{X}) \\ & + \epsilon_1\epsilon_x(\mathbb{1}\otimes\mathbb{X})\rho(\mathbb{1}\otimes\mathbb{X}) + \epsilon_y\epsilon_x(\mathbb{X}\otimes\mathbb{Y})\rho(\mathbb{X}\otimes\mathbb{Y}) + \epsilon_y^2(\mathbb{Y}\otimes\mathbb{Y})\rho(\mathbb{Y}\otimes\mathbb{Y}) + \epsilon_y\epsilon_z(\mathbb{Z}\otimes\mathbb{Y})\rho(\mathbb{Z}\otimes\mathbb{Y}) \\ & + \epsilon_1\epsilon_y(\mathbb{1}\otimes\mathbb{Y})\rho(\mathbb{1}\otimes\mathbb{Y}) + \epsilon_z\epsilon_x(\mathbb{X}\otimes\mathbb{Z})\rho(\mathbb{X}\otimes\mathbb{Z}) + \epsilon_z\epsilon_y(\mathbb{Y}\otimes\mathbb{Z})\rho(\mathbb{Y}\otimes\mathbb{Z}) + \epsilon_z^2(\mathbb{Z}\otimes\mathbb{Z})\rho(\mathbb{Z}\otimes\mathbb{Z}) \\ & + \epsilon_z\epsilon_1(\mathbb{1}\otimes\mathbb{Z})\rho(\mathbb{1}\otimes\mathbb{Z}) + \epsilon_1\epsilon_x(\mathbb{X}\otimes\mathbb{1})\rho(\mathbb{X}\otimes\mathbb{1}) + \epsilon_1\epsilon_y(\mathbb{Y}\otimes\mathbb{1})\rho(\mathbb{Y}\otimes\mathbb{1}) + \epsilon_1\epsilon_z(\mathbb{Z}\otimes\mathbb{1})\rho(\mathbb{Z}\otimes\mathbb{1}) + \epsilon_1^2\rho].\end{aligned} \tag{2.27}$$

Here $p_1 = e^{-t/T_A}$ and $p_2 = e^{-t/T_B}$ and $\epsilon_x+\epsilon_y+\epsilon_z+\epsilon_1 = 1$, these give the probabilities for each unitary operation to happen. Depending on the choice of these probabilities we can apply various decoherence models. Setting each unitary operation probability to $\epsilon_x = \epsilon_y = \epsilon_z = \epsilon_1 = \frac{1}{4}$ models the depolarising channel that we will use in our simulations, while setting $\epsilon_z = \epsilon_1 = \frac{1}{2}$ yields the dephasing channel. The decoherence times given by T_A and T_B can be considered equal since we will use one type of hardware for our quantum memories, we will refer to it as T_d.

We are interested in the decoherence of the stored state after the X-measurement has projected the state onto the multiple Bell states and the phases are corrected, given by:

$$|\psi\rangle = \frac{1}{\sqrt{2^m}}\Big(|0\rangle_A|0\rangle_B + |1\rangle_A|1\rangle_B\Big)^{\otimes m}. \tag{2.28}$$

If we write this as a density matrix and trace out all pairs except for one, we can find the density matrix of one Bell pair from which we can derive the time-dependent evolution under decoherence by applying the channel as given in Eq. 2.27. This density matrix is straightforwardly represented by:

$$\begin{aligned}\mathrm{Tr}_{\{A_i,B_i\}_{i\neq 1}}(|\psi\rangle\langle\psi|) = \frac{1}{2}\Big(& |0,0\rangle_{A,B}\langle 0,0|_{A,B} + |0,0\rangle_{A,B}\langle 1,1|_{A,B} \\ & + |1,1\rangle_{A,B}\langle 0,0|_{A,B} + |1,1\rangle_{A,B}\langle 1,1|_{A,B}\Big).\end{aligned} \tag{2.29}$$

Passing this state through the depolarising channel and calculating the fidelity with respect to the target Bell state we find that only the terms with the same error on both qubits will result in a non-zero contribution. After some linear algebra, we will find that the fidelity is given by:

$$\begin{aligned}\langle\Phi^+|\,\bar{\rho}\,|\Phi^+\rangle =& \frac{1}{2}\Big((p_1+(1-p_1)\epsilon_1)(p_2+(1-p_2)\epsilon_1) + (1-p_1)(1-p_2)(\epsilon_x^2+\epsilon_y^2+\epsilon_z^2)\Big) \\ =& \frac{1}{2}\Big((e^{-t/T_A}+(1-e^{-t/T_A})\epsilon_1)(e^{-t/T_B}+(1-e^{-t/T_B})\epsilon_1) \\ & + (1-e^{-t/T_A})(1-e^{-t/T_B})(\epsilon_x^2+\epsilon_y^2+\epsilon_z^2)\Big).\end{aligned} \tag{2.30}$$

In §3, you will find that there is another factor in front since the states were not normalised in order to retain their probability amplitudes. In that context, we will normalise the calculated fidelity by dividing it by the success probability associated with the heralded pair.

3 Model

In this section, we will provide a description of our model for simulating entanglement distribution using a satellite-based high-dimensional protocol. We will begin by reviewing the protocol itself and then delve into the calculation of the entanglement distribution rate, which becomes non-trivial when multiple entangled pairs are desired and there is a limited amount of memory modes. We will initially focus on the calculation for the simplest case of entangling a single pair and subsequently expand our analysis to incorporate a parallel scheme involving multiple entangled pairs. Additionally, we will explore the incorporation of multiplexing techniques to increase the rate and improve the overall fidelity of the protocol. Lastly, we will outline a method for calculating the average fidelity of all entangled pairs, accounting for the potential decoherence of successful pairs when stored in quantum memories.

3.1 Entanglement distribution protocol

In our model, we aim to maintain a high level of generality by not focusing on a specific type of hardware or setup for the protocol's operations. However, it is important to note that we do consider the use of an SPDC source in our model. This choice is motivated by the successful implementation of SPDC-based setups in state-of-the-art experiments, such as the Micius satellite experiment, which achieved entanglement between ground stations over significant distances [20]. SPDC sources offer several advantages, including their accessibility, suitability for room temperature operation, and their flexibility for customisation in various implementation scenarios. By incorporating an SPDC source into our model, we align with the capabilities demonstrated in previous experiments while maintaining a broader scope for the rest of the hardware and operations in our protocol. The protocol starts with the SPDC source as our probabilistic source of entangled photonic qudits. We have a laser and a non-centrosymmetric medium that utilises its second order ($\chi^{(2)}$) non-linearity to enable three electromagnetic fields to interact (three-wave mixing) as explained in the theory section, §2. In the case of spontaneous parametric down-conversion, the two lower energy fields are initially in vacuum modes and the medium obeys the conservation of energy and momentum. After one laser pulse is used to pump the nonlinear crystal, the state emitted can be written as follows:

$$|\Psi\rangle_{A,B} = \sqrt{1-\lambda^2}\sum_{n=0}^{\infty}\lambda^n |n,n\rangle_{A,B} \approx \sqrt{1-\lambda^2}\left[|0,0\rangle_{A,B} + \lambda|1,1\rangle_{A,B} + \lambda^2|2,2\rangle_{A,B} + \mathcal{O}(\lambda^3)\right]. \quad (3.1)$$

Here the left and right parts of the 'ket' correspond to two different spatial modes directed toward the ground stations of Alice and Bob respectively and the states are written in the number state basis ($|n\rangle$) where n denotes the number of photons present. This is a two-mode squeezed vacuum state and it can be seen as a probabilistic source of photon pairs. We assume that the source has been tuned appropriately in order to reduce the probability of higher-order excitations, we thus assume $\lambda \ll 1$. The multi-pair events happen with a strong dependency on the pump power and as such they can be tuned down to low probabilities by considering a weak-pump regime [53]. The most probable term will be the vacuum state, $|0,0\rangle_{A,B}$, with a probability of $1-\lambda^2$. Meanwhile, the desired single photon pairs, $|1,1\rangle_{A,B}$, are only emitted with a probability of $\lambda^2 - \lambda^4$. It is therefore difficult to find a regime in which the rate of single photon pairs is large enough without getting too many higher-order emissions that will result in an error.

Consider the scenario where we incorporate multiple pulses into well-defined time bins from the source. This enables us to generate time-bin encoded states. By using 2^m pulses, we can create 2^m-dimensional qudit states, where the information is encoded in time bins of duration τ_{rep}, corresponding to a single pulse set by the pump laser's frequency. The state can be expressed as:

$$\begin{aligned}|\Psi\rangle_{A,B} &= \bigotimes_{l=0}^{2^m-1}\sqrt{1-\lambda^2}\sum_{n=0}^{\infty}\lambda^n|n_l,n_l\rangle_{A,B} \\ &\approx (1-\lambda^2)^{2^{m-1}}\left[|0,0\rangle_{A,B} + \lambda\sum_{l=0}^{2^m-1}|1_l,1_l\rangle_{A,B} + \lambda^2\sum_{l=0}^{2^m-1}\sum_{j\geq l}^{2^m-1}|1_l1_j,1_l1_j\rangle_{A,B} + \mathcal{O}(\lambda^3)\right].\end{aligned} \quad (3.2)$$

Here, the subscripts denote the time bins of the respective photons. For example, the state $|1_l 1_j, 1_l 1_j\rangle_{A,B}$, indicates that Alice and Bob both have one photon in time bin l and one in time bin j. Considering the 2^m time bins, the rate of qudit generation is $\tau_c = 2^m \tau_{rep}$. The emitted photon pairs exhibit strong correlations in the temporal mode, indicating entanglement. As higher-order emissions occur with low probability, we can assume that detected photons are part of a single photon pair most of the time. If we observe a photon in a particular time bin, we can infer that the other photon is also in the same time bin. Therefore, we have a probabilistic entangled photon source, where the squeezing parameter determines the probability of obtaining an entangled photon pair.

As explained in §2, the state emitted from the satellite is affected by loss during transmission through space to the two ground stations. The state is effectively passed through a beam splitter with one output mode being the loss mode and the other being the transmitted mode. Upon arrival at a detector the state again effectively passes through a beam splitter with one loss mode and a successfully detected mode. Together this equates to an effective transmittance of $\sqrt{p_T \eta}$, where η represents the detector efficiency and p_T denotes the probability of transmission for which the value is determined using a theoretical model developed by Janice van Dam [21]. Here, the parameters used have been heuristically tuned to match our transmission probability with the reported transmission loss at 1200 km in Ref. [20]. We apply the beam splitter equation to Eq. 3.2 which is truncated at $\mathcal{O}(\lambda^3)$ to make the calculations more manageable. Additionally, the detectors can suffer from dark counts. With some probability (p_{dark}) the detector will measure a photon even though the state is in vacuum, thus resulting in the mapping $|0\rangle \rightarrow \sqrt{p_{dark}}\,|click\rangle$. For the purpose of finding the fidelity, we don't care about the exact mapping but just the probabilities corresponding to all the possible states. In the end, the desired state is the following:

$$|\Psi\rangle = \frac{1}{\sqrt{2^m}} \sum_{l=0}^{2^m-1} |l\rangle_A |l\rangle_B \,, \tag{3.3}$$

where we want to have only one photon in each of the time bins denoted by l. Upon arrival at the ground stations, the incoming state is mapped to a (multi-)qubit state in two m-qubit registers. To preserve the entanglement and avoid collapsing the state into a product state, a measurement is performed in the generalised X-basis. This measurement, which prevents the extraction of time-bin information, is implemented by applying a quantum Fourier transform. Successful detection in any of the Fourier basis states signifies the occurrence of the entangling operation and is utilised to prepare the two-qubit registers in the $|\Phi^+\rangle$ state:

$$\frac{1}{\sqrt{2}}(|0,0\rangle_{A,B} + |1,1\rangle_{A,B})^{\otimes m}, \tag{3.4}$$

as was described in depth in §2. There are different types of detectors that can be employed, namely photon-number-resolving and non-number-resolving detectors. Photon-number-resolving detectors have the capability to determine the number of photons incident on the detector upon successful detection. This information can be used to enhance the fidelity of the detected state by post-selecting based on the detection of only one photon on either side. On the other hand, non-number-resolving detectors are more commonly used but do not allow for such post-selection. In our model, we consider the use of non-number-resolving detectors to maintain generality. However, it should be noted that employing number-resolving detectors could potentially offer a greater advantage for the qudit protocol as it could mitigate the primary drawback of increased higher-order errors. In the high-loss regime, this advantage might fade since the detection of multiple pairs will not happen frequently. In order to confirm the success of both sides, the measurement outcomes must be communicated between Alice and Bob. Any form of classical communication can be employed for this purpose, and we assume it to be error-free. However, during the communication process, the stored qubits experience decoherence due to interactions with the environment. This heralding time will be referred to as τ_h. If, in addition, the goal is to entangle more than m pairs the heralded pairs also need to wait until all desired pairs have been successfully entangled. We will denote the number of desired pairs as n_p. During this waiting time, the stored pairs also decohere. Taking into account the effects of decoherence and considering the use of non-number-resolving detectors, the average fidelity of a transmitted state can be expressed as follows:

$$
\begin{aligned}
F_{A,B} &= \frac{\langle \Phi^+ | \, \rho_{pair} \, | \Phi^+ \rangle}{\mathrm{Tr}(\rho_{total})} \\
&= \frac{\begin{array}{l} 2^m p_T^2 \eta^2 \lambda^2 ((e^{-t/T_A} + (1-e^{-t/T_A})\epsilon_1)(e^{-t/T_B} + (1-e^{-t/T_B})\epsilon_1) \\ + (1-e^{-t/T_A})(1-e^{-t/T_B})(\epsilon_x^2 + \epsilon_y^2 + \epsilon_z^2)) \end{array}}{\begin{array}{l} 2^m p_T^2 \eta^2 \lambda^2 + 2^{m-1}(2^m+1) p_T^4 \lambda^4 \eta^4 + 2^{m+1} p_T \eta (1 - p_T \eta) \lambda^2 p_{dark} \\ + 2^m (2^m+1) p_T^2 \eta^2 (1-p_T\eta)^2 \lambda^4 \Big(p_{dark} + 2 \Big) \\ + 2^{m+1}(2^m+1) \Big(p_T^3 \eta^3 (1-p_T\eta)\lambda^4 + p_T \eta (1-p_T\eta)^3 \lambda^4 p_{dark} \Big) \\ + p_{dark}^2 \Big(2^{m-1}(2^m+1)(1-p_T\eta)^4 \lambda^4 + 2^m (1-p_T\eta)^2 \lambda^2 + 1 \Big) + \mathcal{O}(\lambda^6). \end{array}}
\end{aligned} \tag{3.5}
$$

Here, ρ_{pair} is the reduced density matrix of a single pair of entangled quantum memories after the X-measurement, obtained by tracing out all other pairs. The denominator represents the trace over the total density matrix and is applied to normalise the fidelity. This gives us the success probability for detecting a photon at both ground stations and hence we are calculating the fidelity of a heralded pair. Furthermore, p_T represents the transmission probability, η denotes the detection efficiency, λ is the squeezing parameter, t represents the waiting time for successful entanglement of all desired pairs, T_A and T_B denote the coherence times of both memory registers, and ϵ_1,ϵ_x, ϵ_y, and ϵ_z represent the error rates for Pauli errors in the I, X, Y, and Z bases, respectively. In our simulations, we set both decoherence times to $T_A = T_B = T_d$. The factor $2^m p_T^2 \eta^2 \lambda^2$ in the numerator stems from the combined effect of different aspects of the protocol. The term λ^2 corresponds to the probability of the creation of a single pair from the SPDC source. The factor 2^m arises from the encoding of a 2^m-dimensional qudit. Lastly, $p_T^2 \eta^2$ accounts for the successful transmission and detection of the entangled pairs. An illustration of the full mathematical state propagation throughout the protocol is provided in Appendix 1 for the case of entangling two pairs with a 4-dimensional qudit.

We will now initiate our analysis by focusing on the rate calculation of the protocol. First, we will examine the scenario where a single source transmits photonic qudits to a pair of receivers. Once we grasp the fundamentals of this setup, we will proceed to investigate the case involving multiple sources attempting to entangle the desired number of pairs. Moreover, we will explore the concept of multiplexing, wherein a surplus of qubit memories is available, enabling multiple sources to concurrently attempt the entanglement of n_p memory pairs. Once we establish a clear understanding of the rate calculation, we will follow a similar approach to determine the average fidelity across the various schemes.

3.2 Rate

In this section, the method for calculating the rate of the protocol in different schemes is explained in depth. We begin by deriving the theoretical value for the rate in a non-parallel scheme. To do this we follow the method used in Ref. [54]. For the case where we have only one source, the total probability of successfully preserving the qudit, accounting for all inefficiencies at both receivers and the channel loss, is denoted as p_{suc}, which is given by the denominator of the fidelity calculation (Eq. 3.5). We start by considering the instance where we attempt to entangle a single pair using a single source. The timing diagram in Fig. 3.2 illustrates how this scheme works in practice. A photonic qudit is transmitted to both ground stations with a repetition time of τ_c, this also denotes the period of attempting to generate entanglement. This cycle time is calculated by taking into account the rate of the pump laser and the number of time bins needed to form a qudit, as depicted schematically in Fig. 3.1. The cycle time is given by $\tau_c = 2^m \tau_{rep}$, where τ_{rep} equals the repetition rate of the pump laser that defines the duration of the time bins.

Each time a qudit is sent the receivers can either detect the qudit or not, due to atmospheric loss or a faulty detection. If a qudit is detected the receiver will close its detector and send a heralding signal to the other ground station. During this time it will keep its detector closed and therefore will not be able to detect any new qudits. Suppose no signal has been received from the other side after the heralding time τ_h has elapsed. In that case, the memory will immediately reset itself and the detector will be

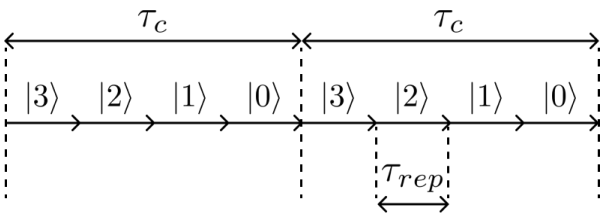

Fig. 3.1: Cycle time diagram depicting the total time per repetition cycle for a 2^2-dimensional photonic qudit, each time-bin takes τ_{rep}, so the cycle time for a general qudit is $\tau_c = 2^m \tau_{rep}$. Here τ_{rep} denotes the repetition rate of the source.

opened simultaneously to receive new qudits again. If during this heralding time, the other receiver had a successful detection, it will also reset its memory and open its detector once the heralding signal corresponding to an earlier time bin arrives from the other side. A successful entanglement will only happen when both receivers are open and detect a qudit at the same instance so that they both receive a heralding signal simultaneously, shown in Fig. 3.2b.

Now, along the same lines as Ref. [54], we can model this detection scheme using a Markov chain as shown in Fig. 3.3. To determine the average rate of entanglement we assume everything that happens in both arms to be symmetric in our simulations. To calculate how many cycles can maximally pass by during the heralding step we define $n = \lceil \tau_h / \tau_c \rceil$. In the Markov chain, a notation is used where there are a total of $3n + 1$ different states to be in. These are represented by a notation (i, j), where i and j denote how many remaining cycles the left and right sides will be closed. Both receivers are open is thus indicated by $(0, 0)$; $\{(i, 0)\}_{i=1}^{n}$, represents that the left had a successful detection and will be closed for i more attempts; $\{(0, i)\}_{i=1}^{n}$, analogously this represents a successful detection at the right and it will be closed for i more cycles; lastly $\{(i, i)\}_{i=1}^{n}$ represents both detectors had a successful detection at some point (although they need not be simultaneous) and they will both be closed for i more entanglement attempts. We further assume our classical communication to be error-free and at the speed of light so that $\tau_h = L/c$, where L is the distance between the two ground stations. The control protocol is as follows: a detector is closed by a controller whenever we have a successful detection and will automatically reopen after n cycles or whenever it receives a heralding signal from the other ground station. In the case where a successful detection took place and the station subsequently receives a heralding signal from the other station corresponding to a different time bin, we know that the protocol was unsuccessful and the memory is reset and the detectors are both opened again. This control scheme together with the probability of transmitting and receiving a photon, determines the probability of transitions in a Markov chain as shown in Fig. 3.3a. We denote the steady-state probability of being in state $(0, 0)$ as $\pi_{(0,0)}$. To calculate the rate, we want to find the probability of a successful entanglement which happens when both detectors are open and have a successful detection, given by $p_{suc}\pi_{(0,0)}$. The rate will then be

$$R_1 = p_{suc}\pi_{(0,0)}/\tau_c. \tag{3.6}$$

Here, p_{suc} is again given by the denominator of Eq. 3.5. We will now define the probability of a successful detection by $p_{ent} = p_{suc}\pi_{(0,0)}$. From Fig. 3.3b we can derive the steady state equation for the probability distribution by substituting p with $\sqrt{p_{suc}}$ and calculating the probability to be in the steady state, which yields:

$$\pi_{(0,0)} = 1/(1 + n(2\sqrt{p_{suc}} - p_{suc})). \tag{3.7}$$

3.2.1 Parallel scheme

In a parallel scheme, we consider multiple sources that try to entangle pairs at multiple receivers in parallel. If the goal is to generate n_p pairs, a qubit-based protocol would necessitate n_p sources, each paired with its corresponding receiver stations. Each source would transmit to two distinct ground stations, forming what we can refer to as an "entanglement generation unit", as illustrated in Fig. 2.1. When high-dimensional qudits are used, however, a ground station maps the received state onto multiple qubit memories, reducing the number of detections needed to entangle multiple pairs. To determine the number of entanglement generation units required in this parallel scheme, we calculate $N = \lceil n_p/m \rceil$,

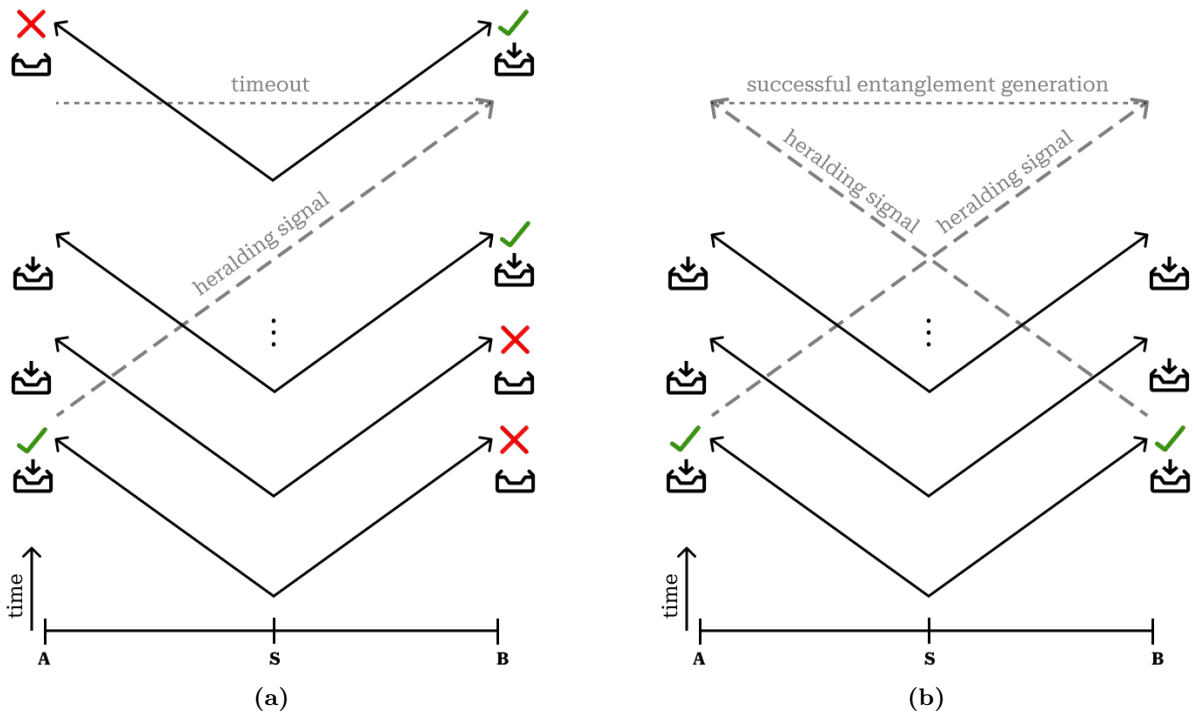

Fig. 3.2: Timing diagrams showing the entanglement generation protocol with a satellite (**S**) sending photonic qudit pairs to Alice (**A**) and Bob (**B**). (a) A number of trials are shown which are all unsuccessful since the qubit registers at Alice's side are all closed due to a successful detection at the beginning. Bob's successful detection is thrown away when he receives the heralding signal from Alice corresponding to a different time. At the timeout, all registers at both sides are immediately reset and opened in order to receive new oncoming qudits. (b) The timing diagram for a successful entanglement generation, here both receivers need to have a successful detection at the same time. They then send their heralding signal and both receive the signal at the same time which tells them they have a successful entanglement generation. They can then choose to keep the stored qubits in their register or reset and run the protocol again.

where m again corresponds to the number of pairs that can be entangled using one 2^m-dimensional qudit. To calculate the rate in this instance we therefore need to consider all possible scenarios in which different entanglement generation units can be successful. Each pair can in principle take infinitely many trials before succeeding and they could succeed in many orders. To capture this we should find the rate by calculating:

$$R = 1/\langle n \rangle \tau_c, \tag{3.8}$$

where $\langle n \rangle$ is the average number of trials needed to get all pairs successfully entangled and τ_c denotes the time per attempt again. The average number of attempts needed for the completion of the protocol can be calculated along the lines of Ref. [55, 56]. There, a function, $\mathcal{Z}_{l,N}(p)$, is defined which calculates the average number of attempts needed to get at least l successes if we have access to N entanglement generation units which all make their attempts simultaneously. If one is successful it is saved until all l receivers are successful, meaning that we have found m entangled pairs. In our parallel scheme, the average number of attempts would thus be $\mathcal{Z}_{N,N}(p)$ which is given as [56]:

$$\mathcal{Z}_{N,N}(p) = \sum_{k=1}^{N} \binom{N}{k} \frac{(-1)^{k+1}}{1-(1-p)^k}. \tag{3.9}$$

Such a compact solution for arbitrary l, N does not exist for the function $\mathcal{Z}_{l,N}(p)$. Therefore, in the upcoming calculations for the multiplexing scheme, we need to approximate this function in the limit where each success always happens at a different time to make the calculations computationally

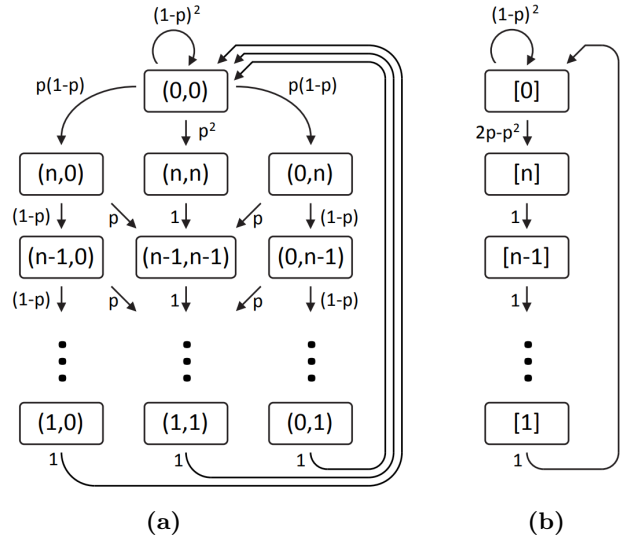

Fig. 3.3: (a) The Markov chain connected to the entanglement distribution protocol for one source and one pair of receivers, as shown in Fig. 3.2. The probability p in this figure denotes the probability of success for an individual arm of the protocol. Since we assume symmetric loss, $p = \sqrt{p_{suc}}$. (b) Diagram illustrating the reduced Markov chain that is derived from (a). Figure taken from Ref. [54].

tractable. Additionally, the same approximation is needed to make our fidelity calculations feasible. We will employ the same approximation for our calculation here (instead of Eq. 3.9) to maintain consistency throughout our analysis. In the approximation where each success is consecutive, we end up with a product of infinite sums where the amount of sums corresponds to the number of entanglement generation units needed to entangle n_p pairs. Note that in principle we are now calculating a conditional expectation value, the expected number of trials needed under the condition that all successes are at different times. We want to approximate the expected value for the number of trials needed, $E(X) = \langle n \rangle$. By the law of total expectation, we have $E(X) = E(X|A)P(A) + E(X|A^c)P(A^c)$ [57]. Here A represents some condition, for our purpose, it will be the condition that all successes occur at different trials. We can use the definition of conditional expectations to write $E(X|A) = \sum_x \frac{xP(X=x\cap A)}{P(A)}$ and find $E(X) = \sum_x P(X = x \cap A) + P(X = x \cap A^c)$. The probability of simultaneous success can be assumed to be very low in the case of a small success probability, p_{ent}. We can therefore neglect the terms with simultaneous successes ($P(X = x \cap A^c)$) and bound the error that we make by considering the sum of probabilities that we are taking into account. We end up calculating:

$$\begin{aligned} E(X|A) &= \frac{N! p_{ent}^N}{p_{approx}} \sum_{i_1=0}^{\infty} \cdots \sum_{i_N > i_{N-1}}^{\infty} \Big(i_1 + 1 + \sum_{k=2}^{N} (i_k - i_{k-1})\Big) (1-p_{ent})^{\sum_{k=1}^{N} i_k} \\ &= \frac{N! p_{ent}^N (1-p_{ent})^{\sum_{k=1}^{N-1} k}}{p_{approx}} \sum_{i_1=0}^{\infty} \cdots \sum_{i_N=0}^{\infty} \left(\sum_{k=1}^{N} (i_k + 1) \right) (1-p_{ent})^{\sum_{k=1}^{N} (N+1-k) i_k} \\ &= N + \sum_{k=1}^{N} \frac{(1-p_{ent})^{N+1-k}}{1-(1-p_{ent})^{N+1-k}} \approx \langle n \rangle_p. \end{aligned} \tag{3.10}$$

Here p_{approx} is given by:

$$p_{approx} = N! p_{ent}^N (1-p_{ent})^{\sum_{k=1}^{N-1} k} \sum_{i_1=0}^{\infty} \cdots \sum_{i_N=0}^{\infty} (1-p_{ent})^{\sum_{k=1}^{N} (N+1-k) i_k}, \tag{3.11}$$

which represents the sum of probabilities for each combination to happen. This can be seen as the weight of our approximation and in case the probability of simultaneous successes is small this sum will tend to one. The variable i_k represents the number of attempts required for pair $k \in 1, \ldots, N$ to achieve

successful entanglement. To account for all possible combinations where there are no simultaneous successes, we sum over these combinations with the condition $i_k > i_{k-1}$ to make sure that each pair needs a different number of attempts. The subscript for $\langle n \rangle_p$ is used to denote that we are using the parallel scheme. We convert all sums to start from zero so we can apply the geometric series solution to all of them. The approximation in Eq. 3.10 can be justified for small p_{ent} and small numbers for N since then we can be sure that with only a very slight probability simultaneous entanglements will occur as given by the error probability:

$$p_{error} = 1 - p_{approx}. \tag{3.12}$$

Since we are neglecting terms with simultaneous successes we know that our calculated average number of trials will be slightly higher than the true average (since on average fewer trials will be needed if simultaneous successes are allowed). The error in our approximation of $\langle n \rangle$ will therefore be upper bounded by $p_{error} \cdot \langle n \rangle_p$. The equation used to calculate the rate in the parallel scheme is given by:

$$R = 1/\langle n \rangle_p \tau_c \tag{3.13}$$

Note that the error made in our approximation propagates through the rate calculation. An upper bound on the absolute error can be estimated by using the functional approach for error propagation [58].

$$\begin{aligned} \alpha_R &= |R(\langle n \rangle_p - p_{error}\langle n \rangle_p) - R(\langle n \rangle_p)| \\ &= p_{error}/\big(\langle n \rangle_p \tau_c (1 - p_{error})\big), \end{aligned} \tag{3.14}$$

where we write the rate as a function of our approximated number of trials. To get the relative error we could calculate

$$\alpha_R / R(\langle n \rangle_p) = \frac{p_{error}}{1 - p_{error}}. \tag{3.15}$$

In our simulations, we can set a certain precision that we want to achieve and check whether we are always operating within that precision.

To compare this scheme utilising multiple sources with a scheme that employs only one source, it is essential to devise an effective strategy for generating multiple entangled pairs with a single source that sends to numerous receiver pairs. Considering that the heralding time should be significantly larger than the repetition time of each qudit ($\tau_c < \tau_h < T_d$), an efficient approach would be to entangle each pair in a cyclic manner, leveraging the heralding time to initiate the generation of new pairs. In this strategy, the source would transmit the photonic qudit to each pair of receivers sequentially, cycling through each pair. This cyclic scheme is akin to the parallel scheme, but with an extended cycle period of $N\tau_c$, as each detector can receive a qudit only after completing a full cycle. Modelling the scenario with only one available source can thus be accomplished using the same model as the parallel source model described above by modifying the cycle period accordingly. It is important to note that in this scheme, which involves only one source, we do not make the approximation that no pairs are simultaneously successful. Instead, the nature of the scheme inherently leads to non-simultaneous successes.

3.2.2 Multiplexing scheme

To calculate the rate in the case of multiplexing we need to take into account that there will be more entanglement generation units present than there are needed. We introduce a new variable, M, that indicates how many times we multiplex. To calculate how many entanglement generation units there are in the multiplexing scheme we then multiply M and N to get the total amount of generation units present, $D = M \cdot N$. The interpretation of multiplexing in our context is illustrated in Figure 3.4, where the concept of combining and processing multiple extra signals to find a small set of entangled pairs is shown. The total number of qubit memories present will then be equal to $D \cdot m$. In the qubit protocol, more entanglement generation units are required since only one pair can be generated per successful attempt (Fig. 3.4b). On the other hand, the qudit protocol can simultaneously entangle multiple pairs with just one successful attempt, resulting in fewer entanglement generation units needed (Fig. 3.4a). In our simulations, we will consider a qudit protocol with a dimensionality such that the number of desired pairs is divisible by m ($n_p \bmod m = 0$). This ensures that both the qubit and qudit protocols have an equal number of memory modes, as illustrated in Fig. 3.4. Now to calculate the rate, we again

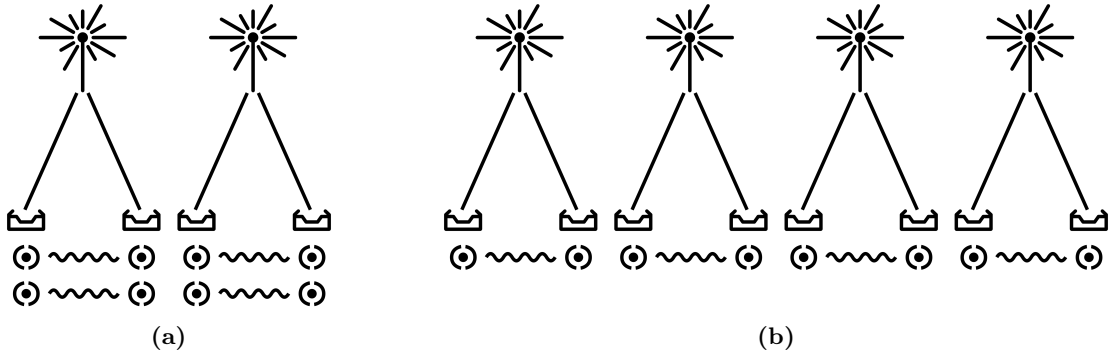

Fig. 3.4: Diagrams illustrating the incorporation of multiplexing in our simulations. The entanglement generation units comprise a source emitting photonic qudit or qubit pairs, along with two receivers. The diagram showcases the generation of two entangled pairs ($n_p = 2$) using two-times multiplexing ($M = 2$). (a) The diagram for illustrating multiplexing in the qudit scheme with a 4-dimensional qudit ($m = 2$). Each receiver maps the incoming qudit state to a register of 2 memory qubits, corresponding to the qudit dimensionality m. To achieve two times multiplexing, two high-dimensional entanglement generation units are employed which will attempt to generate entangled pairs in parallel. (b) The diagram for illustrating multiplexing in the qubit scheme. Each entanglement generation unit maps the received state to one memory qubit and generates one entangled pair. To match the memory resources of the qudit scheme and enable the generation of 2 pairs in the parallel scheme, a minimum of two units is needed (given by N). As we are multiplexing two times, a total of 4 entanglement generation units are required.

need to calculate the approximate number of attempts needed in this scheme as we did for the parallel scheme.

$$\begin{aligned}\langle n\rangle_M &\approx \frac{D!}{(D-N)!\,p_{approx}} p_{ent}^N \sum_{i_1=0}^{\infty}\cdots\sum_{i_N>i_{N-1}}^{\infty}\big(i_1+1+\sum_{k=2}^{N}(i_k-i_{k-1})\big)(1-p_{ent})^{(D-N+1)i_N+D-N+\sum_{k=1}^{N-1}i_k}\\ &= \frac{D!}{(D-N)!\,p_{approx}} p_{ent}^N (1-p_{ent})^{\sum_{k=0}^{N-1}(D-N+k)}\sum_{i_1=0}^{\infty}\cdots\sum_{i_N=0}^{\infty}\left(\sum_{k=1}^{N}(i_k+1)\right)(1-p_{ent})^{\sum_{k=1}^{N}(D+1-k)i_k}\\ &= N+\sum_{k=1}^{N}\frac{(1-p_{ent})^{D+1-k}}{1-(1-p_{ent})^{D+1-k}}\end{aligned} \tag{3.16}$$

Here the subscript M is used to denote that we are in the multiplexing scheme. The error made can again be estimated by considering how much of the total probabilities this expression covers.

$$p_{error} = 1-\frac{D!}{(D-N)!}p_{ent}^N(1-p_{ent})^{\sum_{k=0}^{N-1}(D-N+k)}\sum_{i_1=0}^{\infty}\cdots\sum_{i_N=0}^{\infty}(1-p_{ent})^{\sum_{k=1}^{N}(D+1-k)i_k} \tag{3.17}$$

As long as this error is sufficiently small we can justify our approximation and we can accept the outcome within a small error margin. The rate in this multiplexing scheme can similarly be written as

$$R = 1/\langle n\rangle_M \tau_c. \tag{3.18}$$

3.3 Fidelity

In this section, we present the derived equations for the average fidelity of entangling multiple pairs, taking into account the effects of decoherence during the waiting period for all pairs to become successfully entangled. For the fidelity of the parallel and multiplexing scheme, we employ the same approximation

as before, assuming that each success occurs at different times. This allows us to apply a similar error analysis of our approximation.

3.3.1 Non-parallel scheme

In the non-parallel scheme, we know that since we have one source, simultaneous successes are impossible. After each success, the entangled pair needs to be stored until the last pair has successfully been heralded. In this context, successful attempts naturally occur at different times, allowing us to calculate them accurately without resorting to any approximations. As mentioned earlier, we adjust the cycle period (τ_c) of our source to $N\tau_c$ to accommodate the strategy of sequentially sending photonic qudits to the available receiver pairs.

$$\langle F(t)\rangle_{non-parallel} \approx \frac{p_{ent}^N}{N\, p_{approx}} \sum_{i_1=0}^{\infty} \cdots \sum_{i_N=0}^{\infty} (1-p_{ent})^{\sum_{k=1}^{N} i_k} \left(F(\tau_h)+F(\tau_h+i_N N\tau_c)+\cdots+F(\tau_h+N\tau_c \sum_{k=2}^{N} i_k) \right) \tag{3.19}$$

Here, we assume i_N to be the last pair that gets entangled, consequently, it only decoheres for the heralding time τ_h. In the sum of fidelities that we average over you see that the first pair (i_1) has to wait the longest, namely for $\tau_h + \sum_{k=2}^{N} i_j$ attempts. Where each i_k represents the number of entanglement attempts that were needed for the k^{th} pair to be successfully entangled. The parameter, p_{approx}, is still given by Eq. 3.11.

The entangled qudits are emitted by the source at a rate of τ_c and are directed cyclically towards different receiver pairs. This ensures that each receiver pair can receive the qudits at intervals of $N\tau_c$. Every time these qudits arrive an attempt is made to entangle the ground stations. A successful attempt, however, can only be achieved if both receivers are open and free to detect a qudit this is represented in p_{ent} by the probability $\pi_{(0,0)}$. The fidelities in Eq. 3.19 are calculated by taking into account the corresponding waiting times for which the stored qubit pairs decohere for each pair. In principle, a complicated Markov chain computation should be used to find the various times that certain pairs need to wait in all the different scenarios governed by whether a detector is open or not. Considering that at each cycle of τ_c the probability that the detector is open is given by $\pi_{(0,0)}$ the above gives us a very good approximation of the actual waiting times without the need to calculate the Markov chain. For very high dimensional qudits the cycle time can even become larger than the heralding time so that the detectors are always open.

3.3.2 Parallel scheme

In the parallel scheme, a slight adjustment has to be made to Eq. 3.19. Now we have $N = \lceil n_p/2^m \rceil$ sources individually trying to entangle the qubit memories coupled to an equal number of detectors in parallel. Therefore there are now myriad combinations for the order in which the memories are entangled. So we need to take into account these orders. Additionally, each of the sources is firing continuously in parallel and this needs to be reflected in the infinite sums. In principle there can be simultaneous successes, however, taking all these combinations into account for arbitrary N becomes computationally infeasible since the number of combinations scales like 2^{N-1}. We, therefore, choose to consider only the biggest contribution, which is the case where each entanglement is successful independently and at different times. By doing so, we maintain consistency with our approximations. The average fidelity in this scheme can be represented by:

$$\begin{aligned}
\langle F(t)\rangle_{parallel} &\approx \frac{(N-1)!p_{ent}^N}{p_{approx}} \sum_{i_1=0}^{\infty} \cdots \sum_{i_N > i_{N-1}}^{\infty} \Big[(1-p_{ent})^{\sum_{k=1}^{N} i_k} \\
&\qquad \big(F(\tau_h) + F(\tau_h + (i_N - i_{N-1})\tau_c) + \cdots + F(\tau_h + (i_N - i_1)\tau_c)\big)\Big] \\
&= \frac{(N-1)!p_{ent}(1-p_{ent})^{\sum_{k=1}^{N-1} k}}{p_{approx}} \sum_{i_1=0}^{\infty} \cdots \sum_{i_N=0}^{\infty} \Big[(1-p_{ent})^{\sum_{k=1}^{N} (N+1-k) i_k} \\
&\qquad \big(F(\tau_h) + F(\tau_h + (i_N+1)\tau_c) + \cdots + F(\tau_h + \tau_c \sum_{j=2}^{N} (i_j+1))\big)\Big].
\end{aligned} \tag{3.20}$$

3.3.3 Multiplexing scheme

In the multiplexing scheme, we employ an abundance of entanglement generation units, given by $D = M \cdot N$, surpassing the required number in the parallel scheme. This surplus of units contributes to an enhanced success probability in entangling the desired number of pairs. To accommodate the surplus of entanglement generation units in the multiplexing scheme, we make a slight adjustment to the equation derived for the parallel scheme (Eq. 3.20). This adjustment takes into account the fact that we now have more units than the number of successful attempts needed to entangle all desired pairs. Again we apply the approximation that each successful entanglement happens at different times in order to make the calculation computationally feasible. We arrive at:

$$\begin{aligned}\langle F(t)\rangle_{multi} \approx & \frac{D!}{N\cdot(D-N)!\,p_{approx}} p_{ent}^{N} \sum_{i_1=0}^{\infty}\cdots\sum_{i_N>i_{N-1}}^{\infty}\Big[(1-p_{ent})^{(D-N+1)i_N+D-N+\sum_{k=1}^{N-1} i_k} \\ & \big(F(\tau_h)+F(\tau_h+(i_N-i_{N-1})\tau_c)+\cdots+F(\tau_h+(i_N-i_1)\tau_c)\big)\Big] \\ = & \frac{D!}{N\cdot(D-N)!\,p_{approx}} p_{ent}^{N}(1-p_{ent})^{\sum_{k=0}^{N-1} D-N+k} \sum_{i_1=0}^{\infty}\cdots\sum_{i_N=0}^{\infty}\Big[(1-p_{ent})^{\sum_{k=1}^{N}(D+1-k)i_k} \\ & \big(F(\tau_h)+F(\tau_h+(i_N+1)\tau_c)+\cdots+F(\tau_h+\tau_c\sum_{j=2}^{N}(i_j+1))\big)\Big].\end{aligned} \tag{3.21}$$

This equation gives the most general form since we can retrieve the parallel scheme expression by setting $M = 1$.

4 Results

In this section, we present the results obtained from our simulations, providing insights into the performance gain achievable by utilising qudits instead of qubits in our entanglement scheme. It is important to note that our model offers flexibility in selecting various parameters, and the chosen parameters in this analysis serve as indicative examples rather than definitive values. While it is possible to explore different dimensions for the qudits, it is worth considering that employing extremely high-dimensional qudits may have associated trade-offs, such as increased higher-order excitations and a lower cycle rate. It is worth noting that a qubit can be regarded as a 2^1-dimensional qudit, with m equal to 1.

We expect less stringent memory requirements for higher-dimensional qudits, therefore it seems interesting to examine the impact of varying the memory coherence times. To investigate this effect, we analyse the rate of heralded entanglement (as discussed in §3.2) at different distances. Due to losses and information leakage to the environment, the entanglement can be of very bad quality leading to imperfect fidelity. To address this, we focus on the rate at which the fidelity exceeds a specified minimum value. For our initial plots, we take this minimal fidelity threshold to be 0.8. As the distance increases, the transmission probability decreases, and the heralding time lengthens, both contributing to a decline in fidelity.

The fidelity of our entanglement scheme is influenced by various parameters associated with the environment and hardware employed. One significant parameter is the squeezing parameter λ, which can be easily adjusted, allowing us to fix other governing parameters at realistic values corresponding to common hardware types. We can then find for which λ we get a fidelity greater than 0.8 and since we know that the rate increases with λ due to larger pump power, we select the greatest value for which this holds. Utilising these parameters, we calculate the rate at different distances, generating the rate-distance plots displayed below. Each plot includes the transmission probability p_T for various distances, as specified in Table A1, considering a Low Earth Orbit (LEO) satellite positioned at a height of 400 km. As anticipated, the transmission probability decreases as the distance between ground stations increases, underlining its importance when interpreting the plots. We proceed to investigate different input parameters, such as varying memory coherence times, adjusting the minimum fidelity threshold, reducing the dark count probability p_{dark}, and considering memory multiplexing (or no multiplexing). Additionally, some plots are included to aid with interpreting the results. Finally, a plot showing the transmission probability as a function of distance is given for different satellite heights emphasising the significance of selecting a compatible height with the ground station distances that are considered. The bound on the error of the approximations made concerning simultaneous successes, as discussed in §3, is set to 1%.

In Fig. 4.1, we present the entanglement rate as a function of distance, considering a memory coherence time of 1 second and a minimum fidelity of 0.8. We compare the rates for generating 5 entangled pairs and 10 entangled pairs using both qubits ($m = 1$) and qudits ($m = 5$). With a coherence time of 1 second, the entanglement of 5 pairs demonstrates excellent results for the qudit protocol, as the minimum fidelity of 0.8 is surpassed across a wide range of squeezing parameters for any amount of multiplexing. The qudit protocol doesn't gain anything concerning the fidelity from multiplexing for entangling 5 qubits with $m = 5$ since only one successful generation is required so multiplexing will not affect the fidelity. However, multiplexing does increase the rate, as it allows for a higher number of entanglement generation units to be simultaneously used, thereby increasing the success probability. On the other hand, the qubit protocol benefits significantly from multiplexing for fidelity. Without multiplexing, the fidelity is too low to entangle 5 pairs even at a distance of 200 km. However, with higher levels of multiplexing, it becomes feasible to achieve the desired fidelity, enabling entanglement over larger distances. The qubit protocol will be hit most by the waiting time, since it will need to wait until 5 successful generations have taken place, the heralding time will become negligible. On the other hand, the qudit is affected mostly by the higher order terms resulting in more errors.

At a distance of 1250 km, the heralding time is approximately 4 ms, which ensures that heralding does not significantly contribute to decoherence with this coherence time of 1 s. Therefore, the rate and fidelity are primarily affected by the decrease in transmission probability resulting from the distance. The plots in Fig. 4.1 shows very encouraging results in favour of the qudit protocol. In both cases, the qudit protocol outperforms the qubit protocol in terms of rate. Additionally, the qudit protocol allows

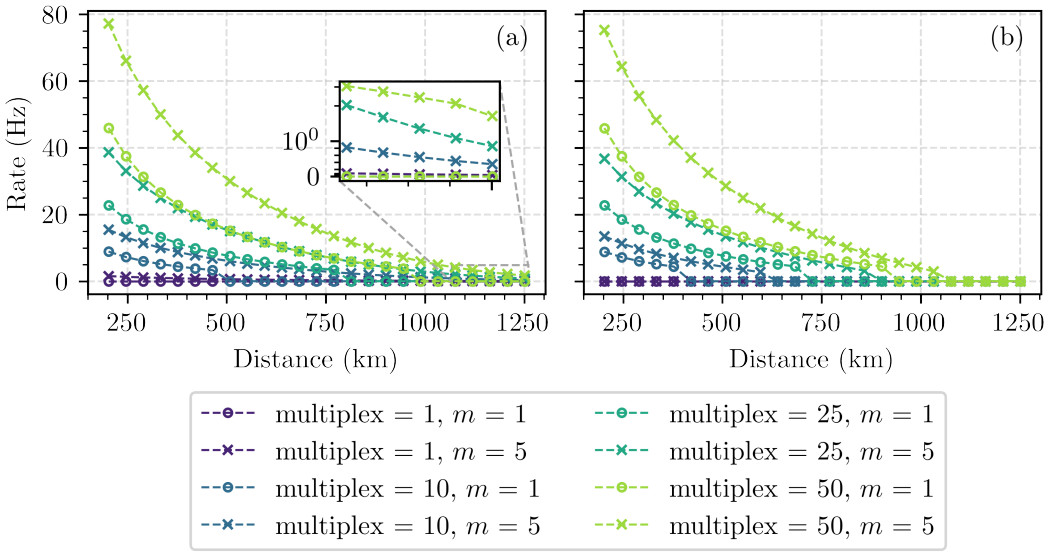

Fig. 4.1: Plots to compare the qubit protocol (circles) to the 2^5-dimensional qudit protocol (crosses) for the entanglement rate vs distance. The rates are plotted for a squeezing parameter (λ) that gives a fidelity greater than 0.8. Each plot uses four different numbers of multiplexing: 1, 10, 25 and 50. Here the other variables are fixed with the following values: $T_d = 1$ s, $p_{dark} = 1.6{\cdot}10^{-5}$, $\eta = 0.5$, $t_{rep} = 10^{-7}$ s. (a) The plot illustrates the entanglement of 5 pairs using both the qubit and qudit protocols. The inset provides a closer view of the results at the longest distances, showcasing the successful entanglement of 5 pairs in the qudit protocol, regardless of the level of multiplexing employed. To enhance clarity, the inset adopts a symmetrical log scale on the y-axis and maintains the same scaling for the x-axis as the main plot. (b) The plot depicts the entanglement of 10 pairs using both the qubit and qudit protocols. In this case, the use of multiplexing becomes essential for the qudit protocol as well. Notably, the qudit protocol exhibits an enhanced capability to achieve entanglement at greater distances, regardless of the level of multiplexing employed.

for entanglement generation with a minimum fidelity of 0.8 over further distances, showing the capability to reach 1250 km with any number of multiplexing for entangling 5 pairs. In the case of entangling 10 pairs the qudit also shows a significant increase in the capability to reach further distances than the qubit protocol although not being able to reach 1250 km even with 50 times multiplexing. Note that for entangling 10 pairs the 2^5-dimensional qudit will also gain from multiplexing for increasing the fidelity since now two successful generations are needed and multiplexing will thus decrease the storage time needed for the completion of the protocol. The qudit protocol will now also be impacted by the waiting time to get multiple successes as shown by the inability to succeed without multiplexing.

It is interesting to understand where the advantage of the qudit comes from. To find out, we will need to have a look at the average fidelity as a function of the squeezing parameter λ. From similar plots to Fig. 4.2a and b, we first find the λ for which the fidelity is greater than some minimum value. This is done for every distance we consider. Looking at the average fidelity as a function of the squeezing parameter we can see that for higher values of m (telling us the dimension of the 2^m-dimensional qudit) the peak fidelity increases and shifts towards smaller values for the squeezing parameter. This is because higher-dimensional qudits are impacted more by higher-order excitations, since more time bins can cause this type of error. Therefore, using a higher order requires the use of a smaller squeezing parameter to offset the effect of additional errors that decay the fidelity. The rate can then be derived from Fig. 4.2c or d by taking the maximum value of λ for which the fidelity is greater than some desired value and checking what the corresponding rate is. For $m = 5$, the fidelity gets very close to unity since all 5 pairs are entangled simultaneously at one successful detection. In case of a successful entanglement, the pairs therefore don't need to wait until additional pairs are successful which is the case for m $\leq$ 5. This is also reflected in the rate in Fig. 4.2c where there is a larger jump in rate between m = 5 and m = 4 than between the other values of m. This is because for lower dimensional qudits the protocol needs

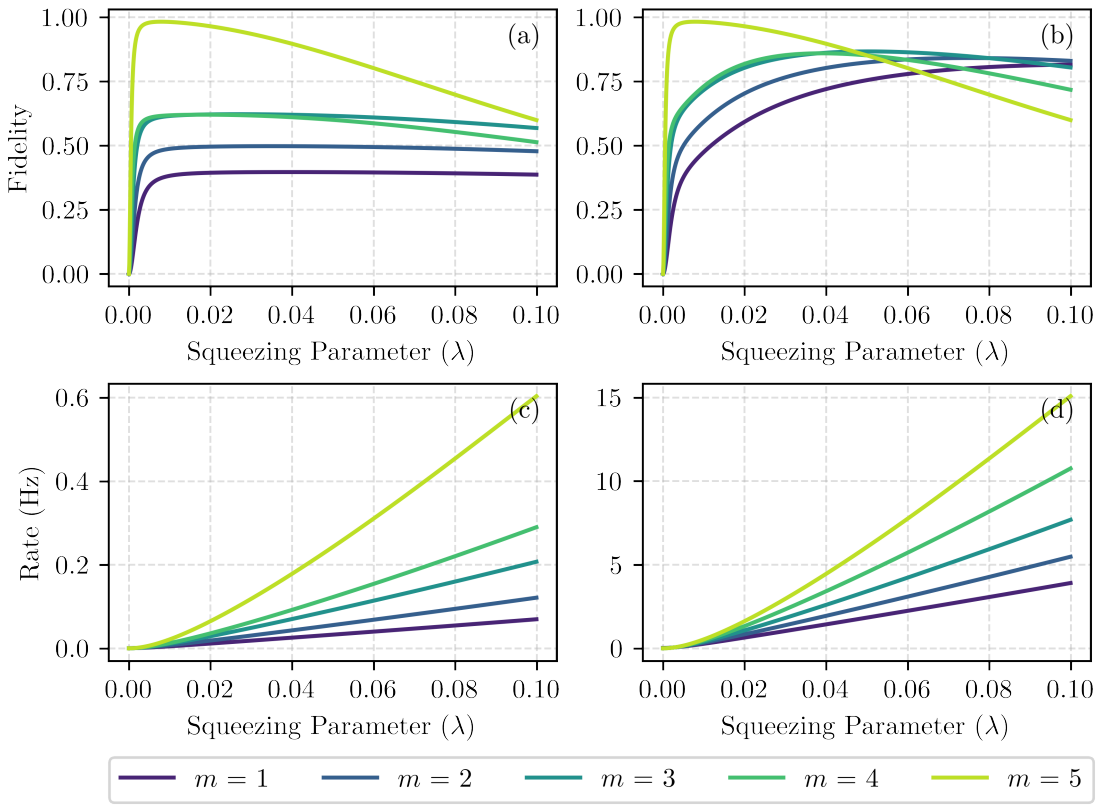

Fig. 4.2: Fidelity and rate for generating 5 entangled pairs as a function of the squeezing parameter λ for 2^m-dimensional qudits with $m \in \{1, 2, 3, 4, 5\}$ with and without multiplexing. The other parameters are given by: $T_d = 1$ s, $p_{dark} = 1.6 \cdot 10^{-5}$, $\eta = 0.5$, $t_{rep} = 1 \cdot 10^{-7}$ s, distance = 727 km. (a) Fidelity without multiplexing. (b) Fidelity with 25 times multiplexing. (c) Rate without multiplexing. (d) Rate with 25 times multiplexing.

to have more than 1 successful attempt to find at least the 5 desired entangled pairs. In Fig. 4.2b and d the fidelity and the rate are shown respectively with a multiplexing of 25 times. This increases the success probability since there are 25 times as many source and detector pairs trying to get a successful detection in parallel. Due to this higher probability, the pairs get successful entanglements with a higher rate and consequently need to wait for shorter times before all pairs are successfully entangled, thus mitigating the decoherence effect present without multiplexing. Interestingly, the rate for the $m = 5$ qudit is increased by 25 times by multiplexing 25 times while the rate for $m \leq 4$ is increased by more than 25 times which is because these pairs need multiple successful detections for the termination of the protocol and are therefore affected nonlinearly by the multiplexing.

We now continue our quest for understanding the dynamics of the high dimensional entanglement protocol by trying to find out the effect of memory decoherence times on the rate. We, therefore, plot Fig. 4.3 and Fig. 4.4 which show the rate as a function of distance for a decoherence time of 0.1 s and 10 s, respectively. These plots are in contrast to Figure 4.1, which showcases a decoherence time of 1 s, while keeping all other parameters constant. It is worth noting that the heralding time, even for a memory coherence time of 0.1 s, has a negligible effect on the decoherence of the stored states, as it remains on the order of milliseconds. Only a slight decay can be seen as represented by a slight overall decrease in rate for the qudit protocol in Fig. 4.3a, when compared to Fig. 4.1a and Fig. 4.4a, due to a smaller squeezing parameter needed to obtain the fidelity threshold. Therefore, the waiting time for stored entangled pairs until all desired pairs are entangled, continues to be the most significant contributing factor for any of the coherence times considered here. As depicted in Figure 4.3a, the qudit protocol experiences minimal impact when attempting to entangle a number of pairs (n_p) equal to the qudit dimension (m), regardless of the coherence time of the memory, as long as it remains significantly

larger than the heralding time. However, for scenarios where $n_p > m$, we can expect the coherence time to play a more prominent role. This is because the waiting time for successful pairs will be much longer than the heralding time alone. In such cases, the stored pairs will be subjected to decoherence for an extended duration, leading to a significant decrease in fidelity. This behaviour is evident in Figure 4.3, where the qudit protocol manages to entangle 5 pairs across varying distances. However, for entangling 10 pairs, the waiting time becomes more pronounced relative to the short coherence time of the memory. Consequently, the fidelity fails to surpass the threshold, even with 50 times multiplexing for distances beyond 350 km. The qubit protocol, in contrast, experiences a significant impact from a decreased coherence time for both entangling 5 pairs and 10 pairs. When comparing the maximum distance achieved by the qubit protocol for generating 10 pairs with 50 times multiplexing to that of generating 5 pairs, we observe a decrease of only 50 km in Fig. 4.3. This relatively diminished effect of increasing the desired number of pairs on the qubit protocol when compared to the large impact of increasing the number of desired pairs on the qudit protocol, is attributed to the fact that the protocol was already influenced by the waiting time in both cases.

In Fig. 4.4, the coherence time is sufficient for both the qubit and qudit protocols to operate effectively, although some multiplexing is required for the qubit protocol. In this scenario, the qudit protocol offers a slight advantage in terms of the entanglement rate. However, it is important to note that the setup for the qudit protocol is significantly more complex and challenging compared to the qubit protocol. Therefore, the marginal increase in rate may not justify opting for the qudit protocol when the coherence times are already excellent. The true advantage of the qudit protocol emerges when memory capabilities are inadequate to coherently store pairs during the waiting time of the protocol. If larger distances were considered, the qudit protocol can potentially outperform the qubit protocol even in such cases. However, it is crucial to acknowledge that the rate would become extremely low due to the reduced transmission probability.

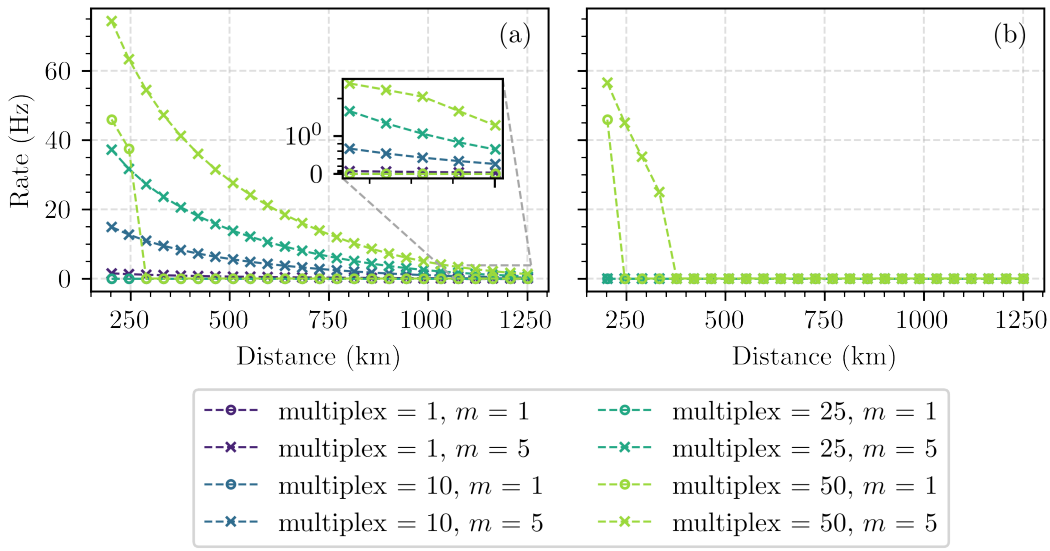

Fig. 4.3: Plots to compare the qubit protocol (circles) to the 2^5-dimensional qudit protocol (crosses) for the entanglement rate versus distance with a memory coherence time of $T_d = 0.1$ s. The rates are plotted for a squeezing parameter (λ) that ensures a fidelity greater than 0.8. Four different levels of multiplexing are considered: 1, 10, 25, and 50. The other variables are kept fixed with the following values: $p_{dark} = 1.6 \cdot 10^{-5}$, $\eta = 0.5$, $t_{rep} = 10^{-7}$ s. (a) The plot for the rate of entangling 5 pairs. (b) The plot for the rate of entangling 10 pairs.

We turn our attention to comprehending the impact of dark count probability, an aspect that can be mitigated through hardware upgrades and the use of superior detectors. In the experiment of entangling two ground stations at an unprecedented distance of 1200 km, Yin et al. reported a dark count probability of $1.6 \cdot 10^{-5}$ [20], which aligns with the value employed in our previous simulations. In Ref. [37] Wallnöfer et al. indicated that a dark count probability of 10^{-6} corresponds to a realistic range

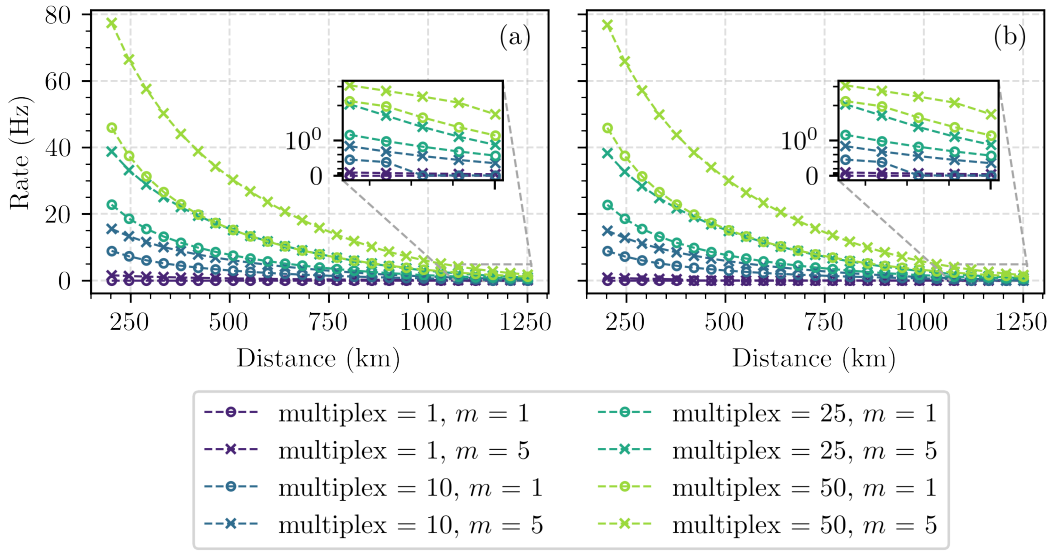

Fig. 4.4: Plots to compare the qubit protocol (circles) to the 2^5-dimensional qudit protocol (crosses) for the entanglement rate versus distance with a memory coherence time of $T_d = 10$ s. The rates are plotted for a squeezing parameter (λ) that ensures a fidelity greater than 0.8. Four different levels of multiplexing are considered: 1, 10, 25, and 50. The other variables are kept fixed with the following values: $p_{dark} = 1.6 \cdot 10^{-5}$, $\eta = 0.5$, $t_{rep} = 10^{-7}$ s. (a) The plot for the rate of entangling 5 pairs. (b) The plot for the rate of entangling 10 pairs.

for current or near-term implementations. Thus, we also adopt this value in our simulation to explore the effect of lowering the dark count probability. The fidelity of the entanglement protocol is influenced by the dark count probability, and its significance becomes more pronounced as the dimensionality increases. With higher-dimensional protocols, the number of possible error terms and noise sources increases, amplifying the weight of dark counts in the fidelity equation. As the dark count probability approaches or becomes comparable to the transmission probability, the effect of dark counts becomes more significant and potentially disruptive. This is particularly noticeable at larger distances, where dark counts carry more weight in the fidelity calculation and can have a greater impact on the overall performance of the protocol. To mitigate the influence of dark counts, it is crucial to minimise their probability through experimental design and the use of high-quality detectors with low dark count rates. By reducing the dark count probability, we can enhance the fidelity and improve the reliability of the entanglement protocol.

From an intuitive standpoint, the reduction in dark count rate is expected to yield a higher fidelity, enabling the protocol to extend its reach to greater distances. However, it should be noted that this reduction may also lead to a slightly lower overall success rate, primarily due to the decreased frequency of dark count clicks. The intricate interplay between fidelity, distance and success rate highlights the significance of minimising dark count rates to optimise the protocol's performance. This is particularly evident in Fig. 4.5c and d, which compares the performance for entangling 10 qubit pairs under the two different dark count probabilities, $1.6 \cdot 10^{-5}$ and 10^{-6} for the qubit and qudit protocol, respectively. In this regime, the lower dark count probability slightly increases the possible entanglement distance allowed by the protocol. For the other regimes considered in Fig. 4.5a and b, upgrading the detectors to achieve an order of magnitude lower dark count probability presents little to no advantage.

While it is conceivable that achieving an even lower dark count rate could offer further advantages, we will not explore that scenario in this context. Instead, we focus on the existing realistic range for dark count rates, such as the considered value of 10^{-6}, which is already challenging to attain in current or near-term implementations. By considering this realistic dark count rate, we can gain insight into the behaviour and performance of the entanglement protocol within practical constraints. It allows us to evaluate the protocol's feasibility and potential advantages under realistic conditions, without delving

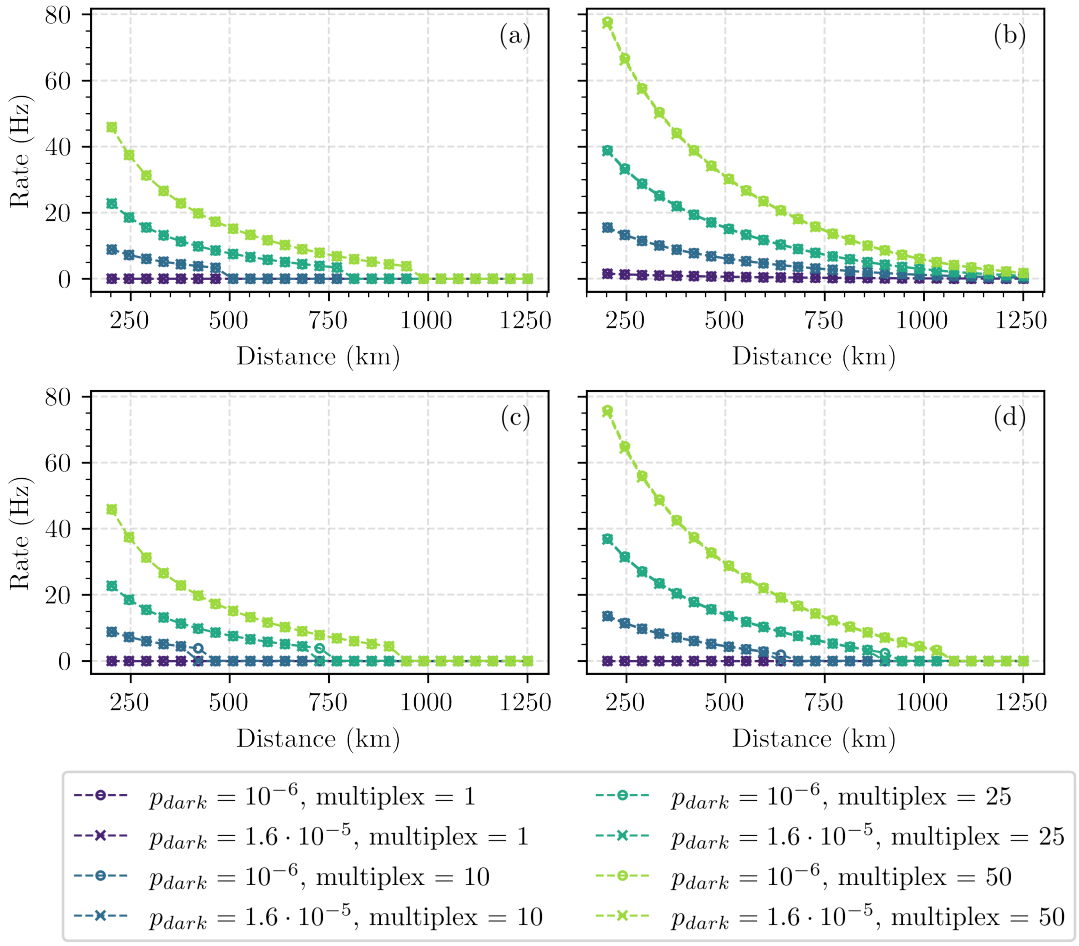

Fig. 4.5: Plots to compare the effect of a lower dark count probability on the rate. These plots are thus overlaying the plots for $p_{dark} = 1.6 \cdot 10^{-5}$ (crosses) and $p_{dark} = 10^{-6}$ (circles). Furthermore, four levels of multiplexing are considered: 1, 10, 25 and 50. Plots (a) and (b) show the plots for entangling 5 pairs using the qubit ($m = 1$) and qudit ($m = 5$) protocol, respectively. Plots (c) and (d) show the plots for entangling 10 pairs using the qubit and qudit protocol, respectively. The other parameters are again given by: $T_d = 1$ s, $\eta = 0.5$, $t_{rep} = 10^{-7}$ s.

into the realm of significantly lower dark count rates that may currently be beyond the reach of available technologies. This allows us to identify areas for improvement and optimisation within the context of current experimental capabilities.

In certain applications where entangled pairs with higher fidelity are required, it is indeed possible to achieve such a goal. However, it comes at the expense of both the rate of entanglement generation (due to a smaller squeezing parameter required) and the achievable distance. This trade-off is clearly demonstrated in Fig. 4.6, where the rate versus distance is simulated for a minimum fidelity of 0.95. The simulations are conducted with memory coherence times of 1 s and 10 s, highlighting the importance of better memory performance in such cases. Interestingly, for the plots with 10 s coherence times, the qubit protocol now outperforms the qudit protocol in terms of rate for a large range of distances. When entangling 5 pairs, the qubit protocol falls short of reaching the 1250 km distance achieved by the qudit protocol. However, in the plot for entangling 10 pairs, the marginal increase in distance by opting for the qudit protocol suggests that it may be more practical to choose the easier-to-implement qubit protocol. On the other hand, when considering entangling 5 pairs with short coherence times, the high-dimensional qudit protocol remains the preferred choice. The qubit protocol can then only surpass the fidelity threshold with 50 times multiplexing and at a distance of up to around 200 km. In the case

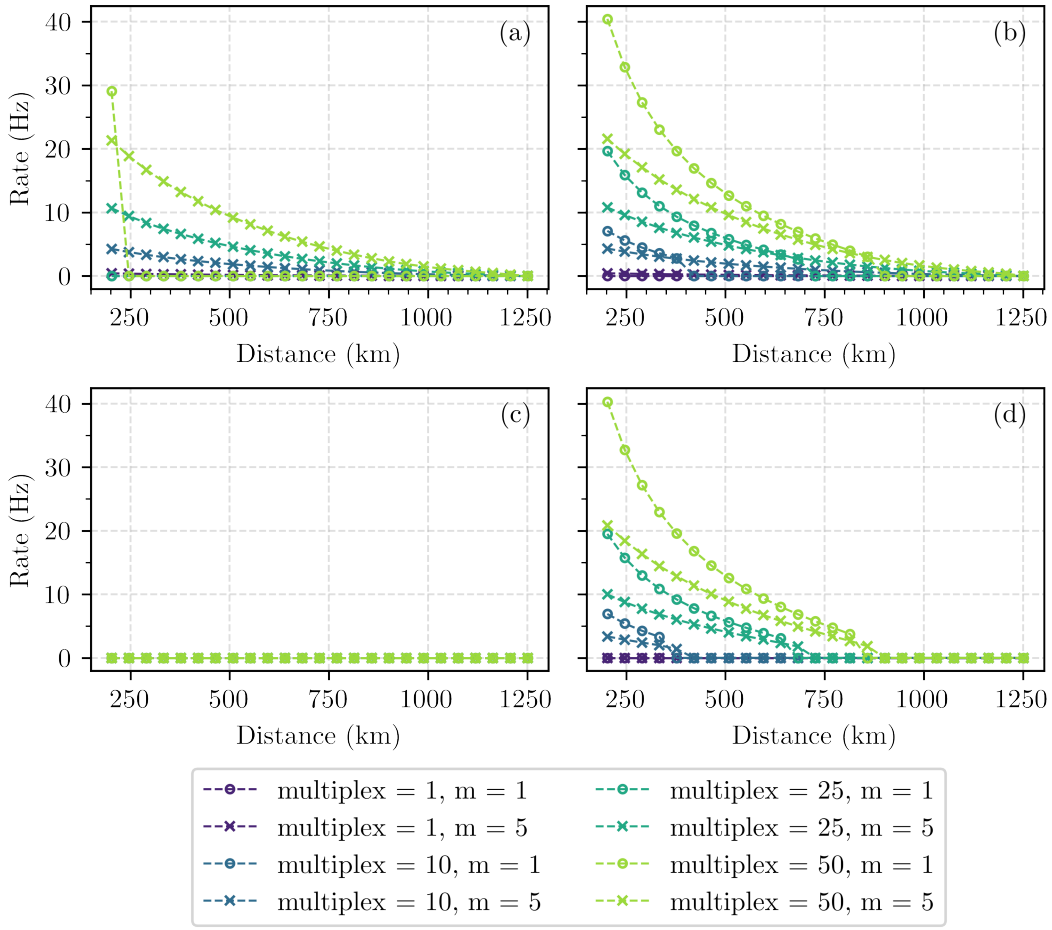

Fig. 4.6: Plots showing the effect of increasing the fidelity threshold to 0.95 and how increasing the coherence time of the memories can enable us to reach this fidelity. We plot the generation of 5 entangled pairs (top row) and 10 (bottom row) pairs using a coherence time of 1 s (left) and 10 s (right). We again compare the qubit protocol (circles) to the $m = 5$ qudit protocol (crosses). The other variables are kept fixed with the following values: $p_{dark} = 1.6 \cdot 10^{-5}$, $\eta = 0.5$, $t_{rep} = 10^{-7}$ s. (a) Entangling 5 pairs using a qubit and qudit protocol with $T_d = 1$ s. (b) Entangling 5 pairs using a qudit with $T_d = 10$ s. (c) Entangling 10 pairs with $T_d = 1$ s. (d) Entangling 10 pairs with $T_d = 10$ s.

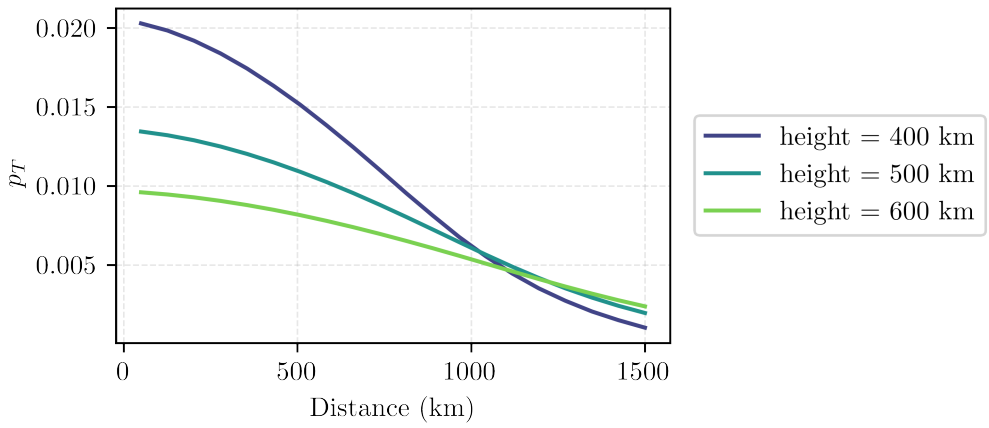

Fig. 4.7: Transmission probability as a function of the distance between ground stations for satellites at three different orbital heights: 400 km, 500 km and 600 km.

of entangling 10 pairs with high fidelity using memories with 1 s coherence time, both protocols are shown to be infeasible.

These observations emphasise the significance of considering the specific requirements of the application, including fidelity, rate, and memory coherence time, when choosing between the qubit and high-dimensional qudit protocols. While the qudit protocol may offer advantages in terms of distance and fidelity under certain conditions, the qubit protocol can be more suitable for scenarios where higher rates and fidelities are required at shorter distances. When faced with limitations in memory coherence time, the high-dimensional qudit protocol will be preferred especially when $n_p = m$, as shown in Fig. 4.3.

The significance of choosing the optimal height for the satellite orbit is demonstrated in Fig. 4.7, which explores different heights for the satellite orbit. The choice of satellite orbit height is crucial as it directly impacts the distances that can be effectively covered. The model takes into account factors such as line of sight and the distance travelled through the atmosphere, where loss due to absorption and reflection is higher. The plot reveals that for distances exceeding 1500 km, an orbit in the range of 600 km high would provide better transmission. This insight is derived from the model developed by Janice van Dam, whose calculations of realistic transmission probabilities have been instrumental in the simulations conducted in this thesis [21]. By considering the optimal satellite orbit height, we can optimise the transmission capabilities of the entanglement protocols. This knowledge is essential in practical implementations where efficient and reliable entanglement generation over long distances is required. Since a satellite height of 400 km provides a superior transmission probability for up to 900 km, we have chosen this orbital height for our simulations.

By carefully considering the optimal satellite orbital height and leveraging the insights from our simulations, we can pave the way for efficient and reliable entanglement generation over long distances by employing high-dimensional encoding. The findings presented in this section not only contribute to the practical implementation of high-dimensional entanglement protocols but also hold great promise for the development of robust and scalable quantum networks in the future.

5 Discussion

The primary objective of this thesis was to investigate the advantages of utilising high-dimensional encoding for entanglement generation in terms of its potential to entangle multiple pairs effectively. The focus was on achieving high-quality entanglement characterised by a high fidelity with the target Bell state, while also striving for a high rate of entanglement. The primary focus of the hardware analysis revolved around the coherence time of the quantum memories and the dark count probability of the detectors. Understanding and minimising the impact of dark counts is crucial for achieving high-quality entanglement. Additionally, a long coherence time for the quantum memory was examined as a critical hardware requirement although exhibiting much less importance for the high-dimensional qudit protocol when the amount of desired pairs corresponds to the dimensionality. The coherence time determines the duration during which the quantum states can be preserved and manipulated, directly affecting the quality and longevity of entanglement. By analysing the coherence time, the study aimed to identify the optimal conditions for generating and maintaining high-fidelity entangled pairs. While the hardware analysis primarily focused on dark count probability and coherence time, it is important to note that these parameters play fundamental roles in determining the feasibility and performance of entanglement protocols. By investigating these specific hardware requirements, this study provides valuable insights into the practical considerations and limitations of implementing high-dimensional entanglement schemes.

Significant progress has been made in achieving long storage times for quantum memories with an optical interface, enabling promising prospects for quantum network applications. For instance, the utilisation of long-lived nuclear spins in diamond has enabled storage times of up to a minute [49]. By leveraging high cooperativity in optical cavities, nearly deterministic photon-spin interfaces have been created, facilitating efficient interaction between photons and spin systems within defect centres [59]. Other recent advancements include the demonstration of coherent light storage for over 1 hour with a fidelity of 96.4% using atomic frequency combs, although with very low efficiency [60]. However, the authors have proposed various techniques to enhance efficiency in such systems. These achievements highlight the potential of quantum memories with long coherence times in the development of efficient quantum networks. To facilitate efficient entanglement distribution, optical memories should possess both long coherence times and high efficiency. Notably, cold atoms confined within a cavity have demonstrated both a retrieval efficiency of $76\pm5\%$ and a $1/e$ lifetime of 0.22 seconds [61]. The coherence times ranging from 0.1 to 10 seconds in this thesis, can therefore be justified, but careful consideration of the hardware is necessary. The progress in achieving long storage times and efficient quantum memories paves the way for the realisation of quantum networks with enhanced capabilities.

A much-researched potential solution for mitigating the impact of transmission loss is the use of quantum repeaters. These repeaters, analogous to classical network amplifiers, enable entanglement distribution over extended distances and at higher rates [37, 62]. Rather than amplification, quantum repeaters leverage entanglement swapping to connect short segments of transmission lines, effectively extending entanglement to the destination node. Introducing quantum repeaters in space-based systems holds great potential for achieving global-scale entanglement distribution, particularly considering the exponential increase in loss in optical fibres. In fact, quantum repeaters are considered essential for the realisation of a quantum internet [1].

The key findings discussed in §4 shed light on several important aspects of the entanglement protocol. Firstly, utilising a 2^m-dimensional qudit, where the dimensionality corresponds to the desired number of entangled pairs ($m = n_p$), enables entanglement over remarkably long distances of up to 1250 km, as demonstrated by our parameterised simulations. Such an advantage of using high dimensionality for reaching larger distances above a certain fidelity threshold was also shown in the simulations by Zheng et al. [15]. In contrast, lower-dimensional qudits would suffer from decoherence while waiting for all desired pairs to be successfully generated. If the decoherence time approaches the time interval between successful entanglement generations ($T_d \gg \tau_c/p_{ent}$), the stored pairs experience minimal decoherence during the waiting period. In such cases, the advantage offered by the qudit protocol over the qubit protocol becomes negligible. Another key aspect of the qudit protocol is that errors are correlated across all of the m pairs entangled by one 2^m-dimensional qudit. In contrast, when using the qudit protocol errors will only affect individual entangled pairs. An intriguing observation is that opting for the qubit protocol can significantly increase the rate of the protocol, compared to using the qudit protocol, when

the fidelity threshold is raised and in case good coherence times (10 s) are achievable as shown in Fig. 4.6. This is caused by the lower amount of squeezing necessary to suppress errors resulting from higher-order emissions when using a photonic qubit. However, this increase in rate comes at the expense of a slightly shorter achievable distance, as the qubit protocol still experiences more decoherence due to the long waiting time for stored pairs until all desired pairs are successfully generated.

It is important to note that certain approximations were employed in the simulations to ensure computational feasibility on a laptop. In the calculation of fidelity and rate, only non-simultaneous successes were considered, assuming that they carry the highest probability weight. While this approximation introduces an error in the overall probability weight of all possible combinations, the error was limited to 1%. Although considering all possible combinations would eliminate this error, it was not feasible given the aim of the thesis to be applicable for general dimensionality m and the amount of desired pairs n_p. Another approximation was made in the fidelity calculation, where the computation of waiting times was simplified by using the steady-state equation that represents the scenario when the detectors are open ($\pi_{(0,0)}$). This approximation allowed for the estimation of expected waiting times for each possible scenario without the need for a complex Markov chain analysis. Although the exact error associated with this approximation is difficult to predict, it is anticipated to be negligible. These approximations were necessary to strike a balance between computational feasibility and the generality of the model. While they introduce some degree of error, their impact on the overall results is expected to be minimal.

To enhance the fidelity of generated pairs in scenarios where the dimensionality is smaller than the number of desired entangled pairs ($m < n_p$), one approach is to impose a storage cutoff time that aligns with the coherence time of the utilised memories. This strategy improves the overall average fidelity of the entangled pairs at the expense of a reduced rate. Additionally, the inclusion of number-resolving detectors can significantly contribute to fidelity improvement in the entanglement protocol examined in this thesis. By post-selecting instances where only one photon is detected, errors arising from higher-order emissions can be mitigated. However, it is important to note that in the high loss regime certain errors associated with higher-order emissions may persist. For example, in cases of second-order emissions, if one photon is lost in both transmission arms, the detectors will erroneously register it as a combined successful detection of a single photon pair.

Additionally, we investigated the impact of decreasing the dark count probability from 1.6×10^{-5} to 10^{-6}. The gain obtained from this reduction is minimal, manifesting as a very slight increase in the achievable distance due to improved fidelity resulting from fewer errors caused by dark counts. To have a more significant impact on the protocol, further reduction in the errors attributed to dark counts is necessary, as the transmission probability at 1250 km is already on the order of 10^{-6} when considering both transmission arms (as shown in Table A1). Given that the dark count probability and the transmission probability are of the same order of magnitude in this regime, dark counts continue to exert substantial influence. Thus, to reach even greater distances with an acceptable fidelity, detector performance needs to be further enhanced when employing the proposed protocol. As the number of pairs to be entangled increases, the impact of reducing the dark count probability becomes more pronounced. This can be attributed to the requirement of a greater number of successful detections, making the fidelity more susceptible to errors arising from dark counts. Therefore, minimising dark count errors becomes increasingly important as the entanglement of multiple pairs is pursued.

The simulations conducted in this study involved different levels of multiplexing, ranging from 1 (no multiplexing) to 50 times. These simulations demonstrate the potential of multiplexing to enhance the rate and extend the achievable distances beyond a certain fidelity threshold. By implementing multiplexing, the success probability of the protocol is increased, leading to higher rates. Consequently, the average fidelity improves as well, as the stored pairs experience shorter waiting times. This effective strategy is clearly illustrated in Fig. 4.1b, where longer distances are obtained by increasing the amount of multiplexing. The simulations indicate that multiplexing may even be necessary to establish entanglement over long distances with a usable rate, particularly when aiming for a fidelity threshold of 0.8 or higher. It is important to acknowledge that multiplexing requires more resources and introduces greater complexity. In our analysis, we ensured that both the qudit and qubit protocols utilised the same total amount of memory resources. However, the qubit protocol would necessitate more photon pair sources to simultaneously transmit photonic qubits to multiple receivers in parallel. On the other hand, the high-dimensional qudit protocol achieves the entanglement of multiple pairs from a single

qudit emission, requiring fewer sources.

Although the hardware analysis did not encompass a comprehensive exploration of all possible hardware aspects, it significantly contributes to our understanding of the key factors influencing the generation of high-quality entanglement. Future research can build upon these findings and expand the analysis to include additional hardware considerations, such as noise sources, photon detection efficiency, and quantum memory storage capacity, to further refine and optimise the implementation of high-dimensional entanglement protocols. To begin with, the effect of photon detection efficiency can already be explored with the model set in place in this thesis. A photon detection efficiency of 50% was used in our analysis, which is already attainable using existing technology. As a result, the potential gain achieved by further improving photon detection efficiency is limited, offering only a two-fold increase in performance. In contrast, other hardware parameters have the potential to yield much more significant improvements. Although the immediate gains in performance by increased detector efficiency may be relatively modest, technological advancements in this area can still play a valuable role in enhancing the overall efficiency and reliability of entanglement protocols.

One important aspect to consider is that we have not explored the effect of changing the repetition rate of the source, which was fixed at a period of 10^{-7} s. Increasing the source rate directly translates to an enhanced rate for the protocol. However, there is an additional, less obvious benefit associated with a higher repetition rate, namely an increase in the overall fidelity and a larger achievable distance. This phenomenon arises because stored pairs would have to wait for shorter periods when pairs are created at a higher rate, leading to reduced decoherence effects. As a result, the entangled pairs would experience fewer errors and exhibit higher fidelities on average. Consequently, this improved fidelity enables entanglement over greater distances, making the protocol more robust and reliable. While the effect of the repetition rate was not explicitly investigated in this thesis, it thus also represents an important tool for the optimisation of the entanglement protocol. By adjusting the source rate, it is possible to achieve the desired rate of entanglement generation and consequently the average fidelity required for specific applications. This could lead to significant advancements in the overall performance and efficiency of the protocol. Increasing the rate alone cannot guarantee better performance, however, and its impact should be thoroughly investigated. While it is reasonable to expect that a higher rate would theoretically improve the system, there are several important considerations to keep in mind. As the rate increases, the time bin resolution decreases, which poses challenges for the detection mechanism. In order to handle the higher rate effectively, the detection system needs to become more efficient and capable of handling the increased data throughput. This may involve optimising the detector design, enhancing the signal-to-noise ratio, and improving timing synchronisation. Additionally, increasing the rate may also require more intricate operations, such as implementing advanced switching patterns to manage the data flow. These additional complexities introduce their own set of challenges, including the need for precise control and synchronisation of multiple components within the system. Therefore, while increasing the rate holds potential benefits, it is essential to consider the overall system requirements and ensure that the detection mechanism, timing resolution, and operational aspects are adequately addressed to fully capitalise on the advantages offered by a higher rate. A comprehensive analysis and thorough optimisation of all relevant factors are crucial to achieving the desired performance improvements when increasing the rate of the source.

Another intriguing aspect to consider is the number of memory modes connected to the receivers. This becomes particularly interesting when addressing the challenge of closed detectors. By employing a sufficient number of memory modes, it becomes possible to overcome this limitation effectively. However, it is important to note that implementing such a solution would require a more intricate detection scheme, possibly involving the utilisation of switches to map detected photons to unoccupied memories. In order for this scheme to function optimally in scenarios where the heralding time exceeds the time interval between successive photons reaching the receivers, a minimum of $N_{mem} \geq \lceil \tau_h p_{suc}/\tau_c \rceil$ memory modes per receiver is necessary. This criterion ensures that there are enough memory modes available to accommodate the temporal gaps between the arrival of successive photons, allowing for efficient mapping and utilisation of the memory resources. Implementing a detection scheme with multiple memory modes per receiver presents new opportunities for enhancing the scalability and flexibility of the entanglement generation process. By carefully designing the detection and memory allocation mechanisms, it becomes feasible to overcome the challenges associated with closed detectors and improve the overall efficiency of the entanglement protocol. It is worth noting that the consideration of memory modes

per receiver and the development of an appropriate detection scheme are areas that warrant further investigation and development. Future research can explore advanced techniques, such as employing optical switches or other strategies, to efficiently allocate and utilise memory resources for maximising the entanglement generation capabilities. By addressing the issue of closed detectors through the integration of multiple memory modes and implementing a sophisticated detection scheme, the potential for generating entangled pairs with higher rates and improved fidelity can be significantly enhanced.

Furthermore, the model employed in this study relies on certain assumptions to manage the computational complexity, which may not fully capture the intricacies of real-life experiments. It is important to acknowledge that different errors can potentially affect the qubit and qudit protocols differently, potentially counteracting the anticipated advantages of the qudit protocol observed in our simulations. For instance, errors arising from incorrect switching and asymmetric loss for different time bins are notable factors to consider. To enhance the accuracy of the current model, it is crucial to incorporate these errors and explore hardware improvements. By addressing these factors, we can strive towards a more precise representation of the experimental conditions and further evaluate the practical viability of the protocols.

The asymmetric loss for different time bins arises from the varying lengths of delay loops. Each earlier time bin passes through delay loops corresponding to its time bin number, while the latest time bin does not pass through any delay loop. As a result, the transmission loss through the delay loops can be expressed as η_l, and if a photon traverses k delay loops, the total loss is given by η_l^k. To address the asymmetric loss for different time bins, a straightforward approach is to introduce beam splitters for the later time bins. By increasing the loss introduced by the beam splitter as the time bin becomes later, the combined loss from the delay loops and beam splitters can be made equal for each time bin. This ensures symmetry in the loss experienced by photons across different time bins. Adjusting the beam splitter's properties for each time bin allows for compensation of the asymmetric loss, providing a more balanced performance in the protocol. Alternatively, the amplitude of different time bins can be adjusted at the source to counterbalance the asymmetric loss caused by the delay loops before the X-measurement. However, for SPDC sources, this solution may be challenging as increasing the pump laser intensity would also affect the squeezing parameter. Consequently, this approach may be more suitable when employing a different source.

The wrong switching error and switch transmission are also potential sources of errors in both the qubit and high-dimensional qudit protocols. However, the high-dimensional qudit protocol is particularly susceptible to this error due to the increased number of switches involved. In the case of high-dimensional qudits, a larger number of switches is required for tasks such as mapping photonic qudits to quantum memories and performing the QFT for X-measurement. Consequently, the impact of switch-related errors, including wrong switching and switch transmission, becomes more pronounced. To accurately model the protocol, it is crucial to consider the transmission efficiency of switches (denoted as η_{sw}) and the occurrence of wrong switching. Wrong switching represents the possibility of light being routed to an incorrect output port of the switch. We can quantify this error as e_{sw}. For instance, if a switch is intended to direct an incoming photon to output port 1, the realistic scenario can be expressed as:

$$|in\rangle \rightarrow \sqrt{1-e_{sw}}\,|out\rangle\,1 + \sqrt{e_{sw}}\,|out\rangle_2\,. \tag{5.1}$$

Each switch in the protocol will have an effective transmission of $\eta_{sw}(1-e_{sw})$, accounting for both transmission loss and errors due to wrong switching. These errors can be heralded, since the absence of detection indicates loss, and the occurrence of wrong switching leads to incorrectly timed detections. Therefore, the wrong switching error can be considered within the transmission loss, as wrong switching events result in heralded errors that are subsequently discarded, contributing to overall loss.

To map the photonic qudit to the qubit memories, m switches are used corresponding to the number of quantum memories. If a photon needs to interact with a cavity, it is switched to the cavity and then reflected back. This process requires the photon to pass through the switch an additional time. The number of times this interaction occurs, denoted by b_1, depends on the specific binary encoding of the time-bin. Each interaction with the cavity introduces further opportunities for errors in the protocol. The total number of switches passed during the process of mapping the photonic qudit to the quantum memories is therefore given by $m + b_1$. Additionally, the resources required for the detection step, such

as switches, beam splitters, and detectors, scale linearly with the dimensionality of the photonic qudit [15]. The temporal modes can thus be mapped to spatial modes by utilising $2^m - 1$ switches before the QFT operation. The total transmission loss resulting from the $2^{m+1} + 2m + 2b_1 - 2$ switches (accounting for both sides of the protocol) can be expressed as $(\eta_{sw}(1 - e_{sw}))^{2^{m+1}+2m+2b_1-2}$. However, it is possible to mitigate the need for switches by employing probabilistic implementations using linear optics. One approach is to use a single fibre loop combined with beam splitters to interfere multiple time bins, as demonstrated in Xiaoyu Liu's master thesis (Ref. [63]). Another strategy involves interfering the qudit photon with local single photons to erase the arrival time, as outlined in Ref. [3]. Employing both path and polarisation modes it has also been shown that the resources needed to construct a QFT interferometer can be reduced by 75% [39]. These alternative techniques provide potential solutions for reducing the reliance on switches while maintaining the functionality of the entanglement detection process. Furthermore, the QFT operation may experience additional phase errors depending on the dimension m. Although a detailed investigation is beyond the scope of this thesis, these errors could be modelled by introducing a dephasing channel with a decay factor of $e^{-\sigma_X^2/2}$, where $\sigma_X = \alpha m$. This formulation accounts for the increase in error with the dimension m [15]. It is worth mentioning that the modelling of decoherence in stored qubits can be significantly enhanced when the hardware details are known, particularly when the dephasing and relaxation times of a memory can be taken into account.

It would also be intriguing to explore methods for mitigating the increased error terms associated with the use of an SPDC source in generating high-dimensional time-bin qudits. A compelling approach was demonstrated in the context of wavelength-multiplexed time-bin entangled pairs, enabling the distribution of pair-wise entanglement across multiple network users using a single SPDC source [64]. This wavelength division multiplexing technique could potentially be used for entangling multiple qubit pairs in our scenario. Another avenue to enhance the quality of quantum entanglement is through the distillation of the two-mode squeezed state emitted by the SPDC source through photon subtraction techniques [28, 65]. This thesis primarily focused on the use of the SPDC source due to its convenience and the successful experimental demonstrations using this setup like in Ref. [20]. However, it is important to note that there are alternative sources of entangled photon pairs that could be employed. One such alternative is the utilisation of Rydberg atoms in cavity quantum electrodynamics (cQED) [66]. This approach allows for the creation of heralded hyper-entangled photon pairs, which could potentially enhance the fidelity of entangled pairs in our protocol. Semiconductor quantum dots are also a viable candidate for generating entangled photon pairs. These quantum dots can produce polarisation-entangled pairs by exciting a quantum dot that subsequently decays to a lower-energy state, emitting two photons. By employing a pulsed laser excitation, it is possible to create time-bin entangled pairs [67]. Additionally, four-wave mixing is an attractive method that can be integrated on-chip, reducing the size and weight of the satellite payload in our protocol [68, 69]. These examples serve to illustrate the diversity of sources and technologies available for generating entangled photon pairs, and many more techniques exist. By exploring these alternative sources, it may be possible to enhance the performance and capabilities of the entanglement protocol considered in this thesis, providing opportunities for further improvements in terms of fidelity, efficiency, and scalability.

This thesis aimed to bridge the gap between theoretical possibilities and experimental feasibility by investigating the potential advantages of high-dimensional encoding in entanglement generation. The findings shed light on the regimes where qudit-based approaches excel, particularly in enabling long-range entanglement distribution. The implications of these findings are significant, as they offer opportunities for various quantum network operations that require the simultaneous entanglement of multiple pairs with low coherence times. For instance, high-dimensional entanglement can enhance quantum metrology, allowing for more precise measurements and improved sensing capabilities [3]. Furthermore, it can be leveraged in blind quantum computing protocols, ensuring privacy and security in computation tasks [4, 5]. Entanglement-based quantum key distribution (QKD) protocols can also benefit from high-dimensional entanglement, enabling secure communication channels resistant to eavesdropping attacks [6, 7]. Moreover, the use of qudit-based entanglement opens up possibilities for teleportation protocols, enabling the transfer of quantum states between distant locations [8, 9].These are just a few examples of the potential applications of high-dimensional entanglement in various quantum network tasks. Overall, this thesis provides valuable insights into the advantages of qudit-based approaches for entanglement generation, paving the way for advancements in quantum communication, computation, and information processing.

6 Conclusion

In this thesis, we have embarked on an exploration of satellite-based entanglement distribution, focusing on the requirement of generating multiple entangled qubit pairs needed for various functionalities within a quantum network. Existing schemes for generating multiple entangled pairs have employed both parallel ([13, 14]) and sequential ([12]) protocols. These protocols typically rely on a register of quantum memories for the storage of successful pairs until all desired pairs are entangled. However, this storage phase poses stringent demands on the coherence time of the quantum memories employed. The challenges are further exacerbated by high transmission and switch loss, coupled with low detection efficiencies, which can lead to prolonged coherence times required for storing successful pairs until the protocol's completion. To address this issue a high-dimensional qudit protocol was proposed in Ref. [15] to enable the simultaneous entanglement of multiple pairs and effectively mitigate the waiting time, during which significant decoherence can occur. Inspired by this proposal, our objective was to model a similar protocol that utilises high-dimensional information encoding and simulate its operation within the context of satellite-based entanglement distribution. The protocol involves a single-photon-pair source that emits pairs of photons in different time bins defining the high-dimensional qudit. The two photons in each pair are then transmitted to two different ground stations. At the ground stations, the incoming photons are mapped to a qubit memory register based on their respective time bins. Subsequently, a generalised X-measurement of the photonic time-bin state is performed, heralding the success of the protocol and resulting in the projection of the memory registers onto multiple Bell pairs. By employing a parameterised model, we were able to compare the performance of the high-dimensional protocol with a comparable qubit-based protocol. Our goal was to identify the specific parameter regimes in which each protocol excels and outperforms the other. This comparative analysis has provided valuable insights into the strengths and limitations of high-dimensional protocols in satellite-based entanglement distribution scenarios.

In our analysis, we focused on two key metrics to compare the two protocols: the distance at which a desired number of entangled pairs could be generated above a specified fidelity threshold, and the rate at which this desired number of entangled pairs could be achieved. By setting a minimum fidelity threshold, we evaluated the protocol's performance at varying distances to determine the maximum achievable range while maintaining the desired fidelity. We then investigated how changing parameters such as the memory coherence time, detector dark count rate, and fidelity threshold influenced these metrics for each protocol. This analysis allows us to identify the parameter regimes in which either protocol demonstrated superior performance in generating the desired number of entangled pairs.

It is important to note that while our model aimed to be as general as possible, we assumed the use of a spontaneous parametric down-conversion (SPDC) source. The use of an SPDC source introduces significant errors in the form of unwanted higher-order emissions, which affect the high-dimensional protocol more severely since more emissions are used to form the high-dimensional time-bin encoding. The key findings of our study reveal that employing a 2^m-dimensional qudit protocol, with a dimensionality corresponding to the desired number of entangled pairs ($m = n_p$), yields the best overall results. This advantage stems from the high-dimensional encoding, which enables the generation of multiple entangled pairs simultaneously, eliminating the need to wait for additional successful pairs. The entangled pairs thus only decoherence during the heralding time. Such high-dimensional encoding allows for long-range entanglement distribution when lower-dimensional encoding proves insufficient. However, it is important to ensure that the coherence time remains longer than the heralding time. With heralding times reaching up to milliseconds for ranges up to 1250 km, achieving the required coherence time seems realistically possible [49]. In cases where longer coherence times are attainable, employing a lower dimensionality may become more attractive due to its easier implementation and the potential for higher rates, albeit at slightly shorter distances as shown in Fig. 4.6. This scenario holds true when the fidelity threshold is set to a high value since the high-dimensional protocol would require a very low squeezing parameter (λ) to minimise higher-order emissions and achieve high fidelities, thereby reducing the rate. Conversely, in scenarios with long coherence times and a lower fidelity threshold, the high-dimensional protocol may still outperform lower-dimensional alternatives. This is because it then does not necessitate an extremely low squeezing parameter to suppress errors, allowing for higher rates. Additionally, we investigated the impact of suppressing dark counts. While higher fidelities can be achieved by reducing dark count probabilities, the expected near-term achievable dark count

probability on the order of 10^{-6} is comparable to the transmission probability, resulting in minimal effects. Further reductions in dark count probabilities are required to observe significant improvements, although for entangling many pairs the reduction in dark counts from $1.6 \cdot 10^{-5}$ to 10^{-6} showed a slight increase in achievable distance in our simulations. Overall, these findings provide valuable insights into the performance and considerations of high-dimensional qudit protocols in satellite-based entanglement distribution.

An important aspect to note is that our simulations incorporated varying degrees of multiplexing. This investigation revealed that in scenarios where the protocol appeared challenging or infeasible, multiplexing emerged as a valuable technique to enhance both the transmission rate and achievable distance. It was observed that when dealing with lower memory coherence times or a higher desired number of entangled pairs, multiplexing offered a highly effective solution. However, it is worth noting that implementing multiplexing requires a more extensive setup, involving additional sources and receivers.

The analysis conducted in this study relied on certain computational approximations to ensure the tractability of the computations. Although these approximations are expected to introduce minimal errors, there is room for further enhancements to increase the accuracy of the model. Furthermore, the model assumed a perfect mapping of the qudit state to the memory register, as well as perfect execution of the generalised X-measurement. However, it is important to acknowledge that real-world implementations may encounter additional errors such as switching errors and asymmetrical loss due to potential delay loops needed to convert the temporal modes to spatial modes. These errors will depend on the specific hardware choices and the experimental setup and could thus be considered when the hardware choices are made. By addressing these considerations and refining the model, future studies can provide a more accurate depiction of the performance and feasibility of high-dimensional qudit protocols in practical satellite-based entanglement distribution scenarios.

The search for solutions to achieve entanglement distribution over global distances has encompassed various domains, particularly due to the impracticality of fibre-based transmission for both high-fidelity and high-rate communication over long distances. The exponential loss inherent in fibre-based systems severely restricts the achievable transmission rates. Satellite-based approaches have emerged as a viable solution to mitigate transmission losses, although they may still face challenges in covering extremely large distances. To address this, the concept of quantum repeaters has been introduced. Quantum repeaters break down the transmission path into smaller segments, allowing for enhanced fidelity and improved transmission rates. In this context, our proposed protocol contributes to the existing solutions, offering a promising pathway towards efficient entanglement distribution. By combining satellite-based approaches with quantum repeaters, we envision a future that holds great potential for the development of quantum networks and a quantum internet. These advancements pave the way for realising widespread entanglement distribution and fostering the growth of quantum technologies on a global scale.

Consideration of the numerous governing parameters poses a significant challenge, making it difficult to account for each one comprehensively. In future research, it would be beneficial to explore alternative approaches by incorporating various different sources, receiver setups, quantum memories, and alternative heralding measurements. Such investigations, involving different hardware configurations, have the potential to yield a more practical protocol with reduced error rates. By exploring these avenues, researchers can further optimise the entanglement distribution process and pave the way for more efficient and reliable implementations.

In conclusion, using a qudit with dimensionality corresponding to the desired amount of pairs ($m = n_p$) consistently yields the largest achievable distances. However, if higher fidelities are required, and the memory coherence times are good enough it may be advisable to consider lower-dimensional protocols. Improving the coherence time will have the most significant impact on the qubit protocol while decreasing the dark count probability of the detectors will slightly improve performance for both qubit and qudit protocols in terms of achievable distance. Lastly, one must consider the optimal orbital height of the satellite, as it depends on the desired entanglement distance. Selecting the appropriate orbital height is crucial for optimising the entanglement capabilities of the system. Overall, these findings provide valuable insights for the practical implementation of high-dimensional entanglement protocols and pave the way for future advancements in quantum networks.

The remarkable progress made in the quest for entanglement distribution over global distances, coupled with the integration of satellite-based approaches and quantum repeaters, presents a promising future for the realisation of a quantum internet. The advancements achieved through this study contribute to the ongoing pursuit of a robust and scalable infrastructure for quantum communication and pave the way for transformative applications in secure communication, quantum computing, and beyond. As the field of satellite-based entanglement distribution continues to evolve, we anticipate that further breakthroughs and innovative solutions will arise, bringing us closer to the seamless integration of quantum technologies into our everyday lives.

References

[1] Stephanie Wehner, David Elkouss, and Ronald Hanson. Quantum internet: A vision for the road ahead, 10 2018. ISSN 10959203. URL https://www.science.org/doi/10.1126/science.aam9288.

[2] Michael A. Nielsen and Isaac L. Chuang. *Quantum Computation and Quantum Information*. Cambridge University Press, 12 2012. ISBN 9780511976667. doi: 10.1017/cbo9780511976667.

[3] E T Khabiboulline, J Borregaard, K De Greve, and M D Lukin. Quantum-assisted telescope arrays. *Physical Review A*, 100(2), 2019. ISSN 24699934. doi: 10.1103/PhysRevA.100.022316.

[4] Joseph F. Fitzsimons. Private quantum computation: an introduction to blind quantum computing and related protocols. *npj Quantum Information*, 3(1):1–11, 6 2017. ISSN 20566387. doi: 10.1038/S41534-017-0025-3. URL https://www.nature.com/articles/s41534-017-0025-3.

[5] Rodney Van Meter and Simon J. Devitt. The Path to Scalable Distributed Quantum Computing. *Computer*, 49(9):31–42, 9 2016. ISSN 00189162. doi: 10.1109/MC.2016.291.

[6] Stefano Pironio, Antonio Acin, Nicolas Brunner, Nicolas Gisin, Serge Massar, and Valerio Scarani. Device-independent quantum key distribution secure against collective attacks. *New Journal of Physics*, 11, 4 2009. ISSN 13672630. doi: 10.1088/1367-2630/11/4/045021.

[7] Valerio Scarani, Helle Bechmann-Pasquinucci, Nicolas J. Cerf, Miloslav Dušek, Norbert Lütkenhaus, and Momtchil Peev. The security of practical quantum key distribution. *Reviews of Modern Physics*, 81(3):1301–1350, 9 2009. ISSN 00346861. doi: 10.1103/RevModPhys.81.1301. URL https://journals.aps.org/rmp/abstract/10.1103/RevModPhys.81.1301.

[8] Charles H. Bennett, Gilles Brassard, Claude Crépeau, Richard Jozsa, Asher Peres, and William K. Wootters. Teleporting an unknown quantum state via dual classical and Einstein-Podolsky-Rosen channels. *Physical Review Letters*, 70(13):1895–1899, 3 1993. ISSN 00319007. doi: 10.1103/PhysRevLett.70.1895. URL https://journals.aps.org/prl/abstract/10.1103/PhysRevLett.70.1895.

[9] Dik Bouwmeester, Jian Wei Pan, Klaus Mattle, Manfred Eibl, Harald Weinfurter, and Anton Zeilinger. Experimental quantum teleportation. *Nature*, 390(6660):575–579, 12 1997. ISSN 00280836. doi: 10.1038/37539. URL https://www.nature.com/articles/37539.

[10] H J Kimble. The quantum internet, 2008. ISSN 14764687. URL http://www.qubitapplications.com.

[11] Sumeet Khatri, Anthony J. Brady, Renée A. Desporte, Manon P. Bart, and Jonathan P. Dowling. Spooky action at a global distance: analysis of space-based entanglement distribution for the quantum internet. *npj Quantum Information*, 7(1), 2021. ISSN 20566387. doi: 10.1038/s41534-020-00327-5. URL http://dx.doi.org/10.1038/s41534-020-00327-5.

[12] N. Kalb, A. A. Reiserer, P. C. Humphreys, J. J.W. Bakermans, S. J. Kamerling, N. H. Nickerson, S. C. Benjamin, D. J. Twitchen, M. Markham, and R. Hanson. Entanglement distillation between solid-state quantum network nodes. *Science*, 356(6341):928–932, 6 2017. ISSN 10959203. doi: 10.1126/science.aan0070. URL https://www.science.org/doi/10.1126/science.aan0070.

[13] Liang Jiang, J M Taylor, Kae Nemoto, W J Munro, Rodney Van Meter, and M D Lukin. Quantum repeater with encoding. *Physical Review A*, 79(3), 2009. ISSN 1050-2947. doi: 10.1103/physreva.79.032325.

[14] William J. Munro, Koji Azuma, Kiyoshi Tamaki, and Kae Nemoto. Inside Quantum Repeaters, 5 2015. ISSN 15584542.

[15] Yunzhe Zheng, Hemant Sharma, and Johannes Borregaard. Entanglement Distribution with Minimal Memory Requirements Using Time-Bin Photonic Qudits. *PRX Quantum*, 3(4), 2022. ISSN 26913399. doi: 10.1103/PRXQuantum.3.040319.

[16] Zhihao Xie, Yijie Liu, Xiang Mo, Tao Li, and Zhenhua Li. Quantum entanglement creation for distant quantum memories via time-bin multiplexing. *Physical Review A*, 104(6):062409, 12 2021. ISSN 24699934. doi: 10.1103/PhysRevA.104.062409. URL https://journals.aps.org/pra/abstract/10.1103/PhysRevA.104.062409.

[17] I. Marcikic, H. De Riedmatten, W. Tittel, H. Zbinden, M. Legré, and N. Gisin. Distribution of time-bin entangled qubits over 50 km of optical fiber. *Physical Review Letters*, 93(18):1–5, 2004. ISSN 00319007. doi: 10.1103/PhysRevLett.93.180502.

[18] Yoshiaki Tamura, Hirotaka Sakuma, Keisei Morita, Masato Suzuki, Yoshinori Yamamoto, Kensaku Shimada, Yuya Honma, Kazuyuki Sohma, Takashi Fujii, and Takemi Hasegawa. Lowest-Ever 0.1419-dB/km loss optical fiber. In *Optics InfoBase Conference Papers*, volume Part F40-O, page Th5D.1. Optica Publishing Group, 3 2017. ISBN 9781943580231. doi: 10.1364/OFC.2017.Th5D.1. URL https://opg.optica.org/abstract.cfm?uri=OFC-2017-Th5D.1.

[19] Markus Aspelmeyer, Thomas Jennewein, Anton Zeilinger, Martin Pfennigbauer, and Walter Leeb. Long-Distance Quantum Communication with Entangled Photons using Satellites. 2003.

[20] Juan Yin, Yuan Cao, Yu Huai Li, Sheng Kai Liao, Liang Zhang, Ji Gang Ren, Wen Qi Cai, Wei Yue Liu, Bo Li, Hui Dai, Guang Bing Li, Qi Ming Lu, Yun Hong Gong, Yu Xu, Shuang Lin Li, Feng Zhi Li, Ya Yun Yin, Zi Qing Jiang, Ming Li, Jian Jun Jia, Ge Ren, Dong He, Yi Lin Zhou, Xiao Xiang Zhang, Na Wang, Xiang Chang, Zhen Cai Zhu, Nai Le Liu, Yu Ao Chen, Chao Yang Lu, Rong Shu, Cheng Zhi Peng, Jian Yu Wang, and Jian Wei Pan. Satellite-based entanglement distribution over 1200 kilometers. *Science*, 356(6343):1140–1144, 2017. ISSN 10959203. doi: 10.1126/science.aan3211.

[21] Janice Van Dam. Analytical Model of Satellite Based Entanglement Distribution, 2022. URL http://resolver.tudelft.nl/uuid:ad64c61c-99a3-42e8-8451-9758b11261e6.

[22] Juan Yin, Yu Huai Li, Sheng Kai Liao, Meng Yang, Yuan Cao, Liang Zhang, Ji Gang Ren, Wen Qi Cai, Wei Yue Liu, Shuang Lin Li, Rong Shu, Yong Mei Huang, Lei Deng, Li Li, Qiang Zhang, Nai Le Liu, Yu Ao Chen, Chao Yang Lu, Xiang Bin Wang, Feihu Xu, Jian Yu Wang, Cheng Zhi Peng, Artur K Ekert, and Jian Wei Pan. Entanglement-based secure quantum cryptography over 1,120 kilometres. *Nature*, 582(7813):501–505, 2020. ISSN 14764687. doi: 10.1038/s41586-020-2401-y. URL https://doi.org/10.1038/s41586-020-2401-y.

[23] Alessandro Fedrizzi, Rupert Ursin, Thomas Herbst, Matteo Nespoli, Robert Prevedel, Thomas Scheidl, Felix Tiefenbacher, Thomas Jennewein, and Anton Zeilinger. High-fidelity transmission of entanglement over a high-loss free-space channel. *Nature Physics*, 5(6):389–392, 2009. ISSN 17452481. doi: 10.1038/nphys1255.

[24] Charles H. Bennett and Stephen J. Wiesner. Communication via one- and two-particle operators on Einstein-Podolsky-Rosen states. *Physical Review Letters*, 69(20):2881, 11 1992. ISSN 00319007. doi: 10.1103/PhysRevLett.69.2881. URL https://journals.aps.org/prl/abstract/10.1103/PhysRevLett.69.2881.

[25] Noah Linden and Sandu Popescu. Good Dynamics versus Bad Kinematics: Is Entanglement Needed for Quantum Computation? *Physical Review Letters*, 87(4):047901, 7 2001. ISSN 10797114. doi: 10.1103/PhysRevLett.87.047901. URL https://journals.aps.org/prl/abstract/10.1103/PhysRevLett.87.047901.

[26] B Hensen, H Bernien, A. E. Dreaú, A Reiserer, N Kalb, M S Blok, J Ruitenberg, R. F.L. Vermeulen, R N Schouten, C Abellán, W Amaya, V Pruneri, M W Mitchell, M Markham, D J Twitchen, D Elkouss, S Wehner, T H Taminiau, and R Hanson. Loophole-free Bell inequality violation using electron spins separated by 1.3 kilometres. *Nature*, 526(7575):682–686, 2015. ISSN 14764687. doi: 10.1038/nature15759.

[27] Martin B. Plenio and Shashank Virmani. An introduction to entanglement measures, 4 2007. ISSN 15337146. URL https://arxiv.org/abs/quant-ph/0504163v3.

[28] Yury Kurochkin, Adarsh S. Prasad, and A. I. Lvovsky. Distillation of the two-mode squeezed state. *Physical Review Letters*, 112(7):0–4, 2018. ISSN 00319007. doi: 10.1103/PhysRevLett.112.070402.

[29] Christopher Gerry and Peter Knight. *Introductory Quantum Optics*. Cambridge University Press, 10 2004. ISBN 9780521527354. doi: 10.1017/cbo9780511791239. URL https://www.cambridge.org/core/books/introductory-quantum-optics/B9866F1F40C45936A81D03AF7617CF44.

[30] J. Brendel, N. Gisin, W. Tittel, and H. Zbinden. Pulsed energy-time entangled twin-photon source for quantum communication. *Physical Review Letters*, 82(12):2594–2597, 3 1999. ISSN 10797114. doi: 10.1103/PhysRevLett.82.2594. URL https://journals.aps.org/prl/abstract/10.1103/PhysRevLett.82.2594.

[31] Ali Anwar, Chithrabhanu Perumangatt, Aitor Villar, Alexander Lohrmann, and Alexander Ling. Development of compact entangled photon-pair sources for satellites. *Applied Physics Letters*, 121 (22), 11 2022. ISSN 00036951. doi: 10.1063/5.0109702. URL /aip/apl/article/121/22/220503/2834573/Development-of-compact-entangled-photon-pair.

[32] Sören Wengerowsky, Siddarth Koduru Joshi, Fabian Steinlechner, Julien R. Zichi, Bo Liu, Thomas Scheidl, Sergiy M. Dobrovolskiy, René van der Molen, Johannes W.N. Los, Val Zwiller, Marijn A.M. Versteegh, Alberto Mura, Davide Calonico, Massimo Inguscio, Anton Zeilinger, André Xuereb, and Rupert Ursin. Passively stable distribution of polarisation entanglement over 192 km of deployed optical fibre. *npj Quantum Information*, 6(1):1–5, 1 2020. ISSN 20566387. doi: 10.1038/s41534-019-0238-8. URL https://www.nature.com/articles/s41534-019-0238-8.

[33] Takahiro Inagaki, Nobuyuki Matsuda, Osamu Tadanaga, Masaki Asobe, and Hiroki Takesue. Entanglement distribution over 300 km of fiber. *Optics Express*, 21(20):23241, 10 2013. ISSN 10944087. doi: 10.1364/oe.21.023241. URL https://opg.optica.org/viewmedia.cfm?uri=oe-21-20-23241&seq=0&html=true.

[34] W. K. Wootters and W. H. Zurek. A single quantum cannot be cloned. *Nature*, 299(5886):802–803, 1982. ISSN 00280836. doi: 10.1038/299802a0. URL https://www.nature.com/articles/299802a0.

[35] Hemani Kaushal, V.K. Jain, and Subrat Kar. Free space optical communication, 2002. URL http://link.springer.com/10.1007/978-81-322-3691-7.

[36] Mustafa Gündoğan, Jasminder S Sidhu, Victoria Henderson, Luca Mazzarella, Janik Wolters, Daniel K.L. Oi, and Markus Krutzik. Proposal for space-borne quantum memories for global quantum networking. *npj Quantum Information*, 7(1), 2021. ISSN 20566387. doi: 10.1038/s41534-021-00460-9. URL https://doi.org/10.1038/s41534-021-00460-9.

[37] Julius Wallnöfer, Frederik Hahn, Mustafa Gündoğan, Jasminder S. Sidhu, Fabian Wiesner, Nathan Walk, Jens Eisert, and Janik Wolters. Simulating quantum repeater strategies for multiple satellites. *Communications Physics*, 5(1):1–8, 6 2022. ISSN 23993650. doi: 10.1038/s42005-022-00945-9. URL https://www.nature.com/articles/s42005-022-00945-9.

[38] Stephan Ritter, Christian Nölleke, Carolin Hahn, Andreas Reiserer, Andreas Neuzner, Manuel Uphoff, Martin Mücke, Eden Figueroa, Joerg Bochmann, and Gerhard Rempe. An elementary quantum network of single atoms in optical cavities. *Nature*, 484(7393):195–200, 4 2012. ISSN 00280836. doi: 10.1038/nature11023. URL https://www.nature.com/articles/nature11023.

[39] Zu En Su, Yuan Li, Peter P. Rohde, He Liang Huang, Xi Lin Wang, Li Li, Nai Le Liu, Jonathan P. Dowling, Chao Yang Lu, and Jian Wei Pan. Multiphoton Interference in Quantum Fourier Transform Circuits and Applications to Quantum Metrology. *Physical Review Letters*, 119(8):080502, 8 2017. ISSN 10797114. doi: 10.1103/PhysRevLett.119.080502. URL https://journals.aps.org/prl/abstract/10.1103/PhysRevLett.119.080502.

[40] Ronen Barak and Yacob Ben-Aryeh. Quantum fast Fourier transform and quantum computation by linear optics. *Journal of the Optical Society of America B*, 24(2):231, 2 2007. ISSN 0740-3224. doi: 10.1364/josab.24.000231. URL https://opg.optica.org/viewmedia.cfm?uri=josab-24-2-231&seq=0&html=true.

[41] P. Törmä, I. Jex, and S. Stenholm. Beam splitter realizations of totally symmetric mode couplers. *Journal of Modern Optics*, 43(2):245–251, 1996. ISSN 13623044. doi: 10.1080/09500349608232738. URL https://www.tandfonline.com/doi/abs/10.1080/09500349608232738.

[42] Yuchen Wang, Zixuan Hu, Barry C. Sanders, and Sabre Kais. Qudits and High-Dimensional Quantum Computing, 11 2020. ISSN 2296424X.

[43] V. V. Zemlyanov, N. S. Kirsanov, M. R. Perelshtein, D. I. Lykov, O. V. Misochko, M. V. Lebedev, V. M. Vinokur, and G. B. Lesovik. Phase estimation algorithm for the multibeam optical metrology. *Scientific Reports*, 10(1):1–8, 5 2020. ISSN 20452322. doi: 10.1038/s41598-020-65466-3. URL https://www.nature.com/articles/s41598-020-65466-3.

[44] Andreas Reiserer, Norbert Kalb, Gerhard Rempe, and Stephan Ritter. A quantum gate between a flying optical photon and a single trapped atom. *Nature*, 508(7495):237–240, 4 2014. ISSN 14764687. doi: 10.1038/nature13177. URL https://www.nature.com/articles/nature13177.

[45] T. G. Tiecke, J. D. Thompson, N. P. De Leon, L. R. Liu, V. Vuletić, and M. D. Lukin. Nanophotonic quantum phase switch with a single atom. *Nature*, 508(7495):241–244, 4 2014. ISSN 14764687. doi: 10.1038/nature13188. URL https://www.nature.com/articles/nature13188.

[46] Norbert Kalb, Andreas Reiserer, Stephan Ritter, and Gerhard Rempe. Heralded storage of a photonic quantum bit in a single atom. *Physical Review Letters*, 114(22):220501, 6 2015. ISSN 10797114. doi: 10.1103/PhysRevLett.114.220501. URL https://journals.aps.org/prl/abstract/10.1103/PhysRevLett.114.220501.

[47] Shuo Sun, Hyochul Kim, Zhouchen Luo, Glenn S. Solomon, and Edo Waks. A single-photon switch and transistor enabled by a solid-state quantum memory. *Science*, 361(6397):57–60, 7 2018. ISSN 10959203. doi: 10.1126/science.aat3581. URL https://www.science.org/doi/10.1126/science.aat3581.

[48] E. Togan, Y. Chu, A. S. Trifonov, L. Jiang, J. Maze, L. Childress, M. V.G. Dutt, A. S. Sørensen, P. R. Hemmer, A. S. Zibrov, and M. D. Lukin. Quantum entanglement between an optical photon and a solid-state spin qubit. *Nature*, 466(7307):730–734, 8 2010. ISSN 00280836. doi: 10.1038/nature09256. URL https://www.nature.com/articles/nature09256.

[49] C. E. Bradley, J. Randall, M. H. Abobeih, R. C. Berrevoets, M. J. Degen, M. A. Bakker, M. Markham, D. J. Twitchen, and T. H. Taminiau. A Ten-Qubit Solid-State Spin Register with Quantum Memory up to One Minute. *Physical Review X*, 9(3), 5 2019. ISSN 21603308. doi: 10.1103/PhysRevX.9.031045. URL http://arxiv.org/abs/1905.02094http://dx.doi.org/10.1103/PhysRevX.9.031045.

[50] C T Nguyen, D D Sukachev, M K Bhaskar, B. MacHielse, D S Levonian, E N Knall, P Stroganov, C Chia, M J Burek, R Riedinger, H Park, M Lončar, and M D Lukin. An integrated nanophotonic quantum register based on silicon-vacancy spins in diamond. *Physical Review B*, 100(16):165428, 2019. ISSN 24699969. doi: 10.1103/PhysRevB.100.165428.

[51] L. M. Duan and H. J. Kimble. Scalable photonic quantum computation through cavity-assisted interactions. *Physical Review Letters*, 92(12):127902, 3 2004. ISSN 00319007. doi: 10.1103/PhysRevLett.92.127902. URL https://journals.aps.org/prl/abstract/10.1103/PhysRevLett.92.127902.

[52] Shuo Sun and Edo Waks. Deterministic generation of entanglement between a quantum-dot spin and a photon. *Physical Review A - Atomic, Molecular, and Optical Physics*, 90(4):042322, 10 2014. ISSN 10941622. doi: 10.1103/PHYSREVA.90.042322/FIGURES/4/MEDIUM. URL https://journals.aps.org/pra/abstract/10.1103/PhysRevA.90.042322.

[53] Ali Anwar, Chithrabhanu Perumangatt, Fabian Steinlechner, Thomas Jennewein, and Alexander Ling. Entangled photon-pair sources based on three-wave mixing in bulk crystals, 4 2021. ISSN 10897623. URL https://pubs.aip.org/aip/rsi/article/92/4/041101/961170/Entangled-photon-pair-sources-based-on-three-wave.

[54] Cody Jones, Kristiaan De Greve, and Yoshihisa Yamamoto. A high-speed optical link to entangle quantum dots. 10 2013. URL https://arxiv.org/abs/1310.4609v1http://arxiv.org/abs/1310.4609.

[55] J. Borregaard, P. Kómár, E. M. Kessler, M. D. Lukin, and A. S. Sørensen. Long-distance entanglement distribution using individual atoms in optical cavities. *Physical Review A - Atomic, Molecular, and Optical Physics*, 92(1):012307, 7 2015. ISSN 10941622. doi: 10.1103/PhysRevA.92.012307. URL https://journals.aps.org/pra/abstract/10.1103/PhysRevA.92.012307.

[56] Nadja K. Bernardes, Ludmiła Praxmeyer, and Peter Van Loock. Rate analysis for a hybrid quantum repeater. *Physical Review A - Atomic, Molecular, and Optical Physics*, 83(1):012323, 1 2011. ISSN 10502947. doi: 10.1103/PhysRevA.83.012323. URL https://journals.aps.org/pra/abstract/10.1103/PhysRevA.83.012323.

[57] Geoffrey Grimmett and Dominic Welsh. *Probability: an introduction*. Oxford University Press, 2014. ISBN 019870996X.

[58] Ifan Hughes and Thomas Hase. *Measurements and their uncertainties: a practical guide to modern error analysis*. OUP Oxford, 2010. ISBN 0191576565.

[59] C T Nguyen, D D Sukachev, M K Bhaskar, B. MacHielse, D S Levonian, E N Knall, P Stroganov, R Riedinger, H Park, M Lončar, and M D Lukin. Quantum Network Nodes Based on Diamond Qubits with an Efficient Nanophotonic Interface. *Physical Review Letters*, 123(18), 2019. ISSN 10797114. doi: 10.1103/PhysRevLett.123.183602.

[60] Yu Ma, You Zhi Ma, Zong Quan Zhou, Chuan Feng Li, and Guang Can Guo. One-hour coherent optical storage in an atomic frequency comb memory. *Nature Communications*, 12(1):1–6, 4 2021. ISSN 20411723. doi: 10.1038/s41467-021-22706-y. URL https://www.nature.com/articles/s41467-021-22706-y.

[61] Sheng Jun Yang, Xu Jie Wang, Xiao Hui Bao, and Jian Wei Pan. An efficient quantum light-matter interface with sub-second lifetime. *Nature Photonics*, 10(6):381–384, 4 2016. ISSN 17494893. doi: 10.1038/nphoton.2016.51. URL https://www.nature.com/articles/nphoton.2016.51.

[62] M K Bhaskar, R Riedinger, B Machielse, D S Levonian, C T Nguyen, E N Knall, H Park, D Englund, M Lončar, D D Sukachev, and M D Lukin. Experimental demonstration of memory-enhanced quantum communication. *Nature*, 580(7801):60–64, 2020. ISSN 14764687. doi: 10.1038/s41586-020-2103-5. URL https://doi.org/10.1038/s41586-020-2103-5.

[63] Xiaoyu Liu. Entanglement distribuition with high-dimensional photonic encoding for entanglement purification and quantum error correction, 2023.

[64] Jin Hun Kim, Jin Woo Chae, Youn Chang Jeong, and Yoon Ho Kim. Quantum communication with time-bin entanglement over a wavelength-multiplexed fiber network. *APL Photonics*, 7(1): 16106, 1 2022. ISSN 23780967. doi: 10.1063/5.0073040. URL https://pubs.aip.org/aip/app/article/7/1/016106/2835124/Quantum-communication-with-time-bin-entanglement.

[65] Tim J. Bartley, Philip J.D. Crowley, Animesh Datta, Joshua Nunn, Lijian Zhang, and Ian Walmsley. Strategies for enhancing quantum entanglement by local photon subtraction. *Physical Review A - Atomic, Molecular, and Optical Physics*, 87(2):022313, 2 2013. ISSN 10502947. doi: 10.1103/PhysRevA.87.022313. URL https://journals.aps.org/pra/abstract/10.1103/PhysRevA.87.022313.

[66] Sutapa Ghosh, Nicholas Rivera, Gadi Eisenstein, and Ido Kaminer. Creating heralded hyper-entangled photons using Rydberg atoms. *Light: Science and Applications*, 10(1):1–9, 5 2021. ISSN 20477538. doi: 10.1038/s41377-021-00537-2. URL https://www.nature.com/articles/s41377-021-00537-2.

[67] N Akopian, N H Lindner, E Poem, Y Berlatzky, J Avron, D Gershoni, B D Gerardot, and P M Petroff. Entangled photon pairs from semiconductor quantum dots. *Physical Review Letters*, 96 (13), 2006. ISSN 00319007. doi: 10.1103/PhysRevLett.96.130501.

[68] Chengyuan Wang, Chung-Hyun Lee, Yosep Kim, and Yoon-Ho Kim. Generation of hyper-entangled photons in a hot atomic vapor. *Optics Letters*, 45(7):1802, 4 2020. ISSN 0146-9592. doi: 10.1364/ol.384567. URL https://opg.optica.org/viewmedia.cfm?uri=ol-45-7-1802&seq=0&html=true.

[69] Hatam Mahmudlu, Robert Johanning, Anahita Khodadad Kashi, Albert van Rees, Jörn P Epping, Raktim Haldar, Klaus-J Boller, and Michael Kues. Fully on-chip photonic turnkey quantum source for entangled qubit/qudit state generation. *Nature Photonics* —, 17:518–524, 2022. ISSN 17494893. doi: 10.1038/s41566-023-01193-1. URL https://doi.org/10.1038/s41566-023-01193-1http://arxiv.org/abs/2206.08715.

Appendices

Appendix 1 Calculations for $m = 2$

In this appendix, we will show the calculation of the fidelity with a concrete example for the 4-dimensional qudit case. We begin at the SPDC source that we use to emit at different time bins, we will find the following state:

$$\begin{aligned}
|\Psi\rangle_{A,B} =&(1-\lambda^2)^2 \sum_{n=0}^{\infty} \lambda^n |n,n\rangle_1 \otimes \sum_{n=0}^{\infty} \lambda^n |n,n\rangle_2 \otimes \sum_{n=0}^{\infty} \lambda^n |n,n\rangle_3 \otimes \sum_{n=0}^{\infty} \lambda^n |n,n\rangle_4 \\
\approx&(1-\lambda^2)^2 \Big[|0,0\rangle + \lambda(|1,1\rangle_1 + |1,1\rangle_2 + |1,1\rangle_3 + |1,1\rangle_4) \\
&+ \lambda^2 \left(|2,2\rangle_1 + |2,2\rangle_2 + |2,2\rangle_3 + |2,2\rangle_4 \right. \\
&+ |1_1 1_2, 1_1 1_2\rangle + |1_1 1_3, 1_1 1_3\rangle + |1_1 1_4, 1_1 1_4\rangle + |1_2 1_3, 1_2 1_3\rangle + |1_2 1_4, 1_2 1_4\rangle + |1_3 1_4, 1_3 1_4\rangle) \\
&+ \mathcal{O}(\lambda^3) \Big]
\end{aligned} \tag{A1}$$

By incorporating a beam splitter with a transmittance of $\sqrt{p_T \eta}$ we can find the state after transmission while including the detection efficiency for the final heralding detection. This give us Eq. A2:

$$\begin{aligned}
|\Psi\rangle_{A,B,l_A,l_B} =&(1-\lambda^2)^2 \Big\{ p_T \eta \lambda \Big[|1,1,0,0\rangle_1 + |1,1,0,0\rangle_2 + |1,1,0,0\rangle_3 + |1,1,0,0\rangle_4 \Big] \\
&+ p_T^2 \eta^2 \lambda^2 \Big[|2,2,0,0\rangle_1 + |2,2,0,0\rangle_2 + |2,2,0,0\rangle_3 + |2,2,0,0\rangle_4 \\
&+ |1_1 1_2, 1_1 1_2, 0,0\rangle + |1_1 1_3, 1_1 1_3, 0,0\rangle + |1_1 1_4, 1_1 1_4, 0,0\rangle \\
&+ |1_2 1_3, 1_2 1_3, 0,0\rangle + |1_2 1_4, 1_2 1_4, 0,0\rangle + |1_3 1_4, 1_3 1_4, 0,0\rangle \Big] \\
&+ \sqrt{p_T \eta (1-p_T \eta)} \lambda \Big[|1,0,0,1\rangle_1 + |1,0,0,1\rangle_2 + |1,0,0,1\rangle_3 + |1,0,0,1\rangle_4 \\
&+ |0,1,1,0\rangle_1 + |0,1,1,0\rangle_2 + |0,1,1,0\rangle_3 + |0,1,1,0\rangle_4 \Big] \\
&+ p_T \eta (1-p_T \eta) \lambda^2 \Big[|2,0,0,2\rangle_1 + |0,2,2,0\rangle_1 + |2,0,0,2\rangle_2 + |0,2,2,0\rangle_2 \\
&+ |2,0,0,2\rangle_3 + |0,2,2,0\rangle_3 + |2,0,0,2\rangle_4 + |0,2,2,0\rangle_4 \\
&+ 2\big(|1,1,1,1\rangle_1 + |1,1,1,1\rangle_2 + |1,1,1,1\rangle_3 + |1,1,1,1\rangle_4\big) \\
&+ |1_1 1_2, 0,0, 1_1 1_2\rangle + |0, 1_1 1_2, 1_1 1_2, 0\rangle + |1_1, 1_1, 1_2, 1_2\rangle \\
&+ |1_1, 1_2, 1_2, 1_1\rangle + |1_2, 1_1, 1_1, 1_2\rangle + |1_2, 1_2, 1_1, 1_1\rangle \\
&+ |1_1 1_3, 0,0, 1_1 1_3\rangle + |0, 1_1 1_3, 1_1 1_3, 0\rangle + |1_1, 1_1, 1_3, 1_3\rangle \\
&+ |1_1, 1_3, 1_3, 1_1\rangle + |1_3, 1_1, 1_1, 1_3\rangle + |1_3, 1_3, 1_1, 1_1\rangle \\
&+ |1_1 1_4, 0,0, 1_1 1_4\rangle + |0, 1_1 1_4, 1_1 1_4, 0\rangle + |1_1, 1_1, 1_4, 1_4\rangle \\
&+ |1_1, 1_4, 1_4, 1_1\rangle + |1_4, 1_1, 1_1, 1_4\rangle + |1_4, 1_4, 1_1, 1_1\rangle \\
&+ |1_2 1_3, 0,0, 1_2 1_3\rangle + |0, 1_2 1_3, 1_2 1_3, 0\rangle + |1_2, 1_2, 1_3, 1_3\rangle \\
&+ |1_2, 1_3, 1_3, 1_2\rangle + |1_3, 1_2, 1_2, 1_3\rangle + |1_3, 1_3, 1_2, 1_2\rangle \\
&+ |1_2 1_4, 0,0, 1_2 1_4\rangle + |0, 1_2 1_4, 1_2 1_4, 0\rangle + |1_2, 1_2, 1_4, 1_4\rangle \\
&+ |1_2, 1_4, 1_4, 1_2\rangle + |1_4, 1_2, 1_2, 1_4\rangle + |1_4, 1_4, 1_2, 1_2\rangle \\
&+ |1_3 1_4, 0,0, 1_3 1_4\rangle + |0, 1_3 1_4, 1_3 1_4, 0\rangle + |1_3, 1_3, 1_4, 1_4\rangle \\
&+ |1_3, 1_4, 1_4, 1_3\rangle + |1_4, 1_3, 1_3, 1_4\rangle + |1_4, 1_4, 1_3, 1_3\rangle \Big] \\
&+ p_T \eta \sqrt{p_T \eta (1-p_T \eta)} \lambda^2 \Big[\sqrt{2}(|2,1,0,1\rangle_1 + |1,2,1,0\rangle_1 + |2,1,0,1\rangle_2 + |1,2,1,0\rangle_2 \\
&+ |2,1,0,1\rangle_3 + |1,2,1,0\rangle_3 + |2,1,0,1\rangle_4 + |1,2,1,0\rangle_4)
\end{aligned}$$

$$
\begin{aligned}
&+ |1_1 1_2, 1_1, 0, 1_2\rangle + |1_1 1_2, 1_2, 0, 1_1\rangle + |1_1, 1_1 1_2, 1_2, 0\rangle + |1_2, 1_1 1_2, 1_1, 0\rangle \\
&+ |1_1 1_3, 1_1, 0, 1_3\rangle + |1_1 1_3, 1_3, 0, 1_1\rangle + |1_1, 1_1 1_3, 1_3, 0\rangle + |1_3, 1_1 1_3, 1_1, 0\rangle \\
&+ |1_1 1_4, 1_1, 0, 1_4\rangle + |1_1 1_4, 1_4, 0, 1_1\rangle + |1_1, 1_1 1_4, 1_4, 0\rangle + |1_4, 1_1 1_4, 1_1, 0\rangle \\
&+ |1_2 1_3, 1_2, 0, 1_3\rangle + |1_2 1_3, 1_3, 0, 1_2\rangle + |1_2, 1_2 1_3, 1_3, 0\rangle + |1_3, 1_2 1_3, 1_2, 0\rangle \\
&+ |1_2 1_4, 1_2, 0, 1_4\rangle + |1_2 1_4, 1_4, 0, 1_2\rangle + |1_2, 1_2 1_4, 1_4, 0\rangle + |1_4, 1_2 1_4, 1_2, 0\rangle \\
&+ |1_3 1_4, 1_3, 0, 1_4\rangle + |1_3 1_4, 1_4, 0, 1_3\rangle + |1_3, 1_3 1_4, 1_4, 0\rangle + |1_4, 1_3 1_4, 1_3, 0\rangle\Big] \\
&+ \sqrt{p_T\eta(1-p_T\eta)}(1-p_T\eta)\lambda^2\Big[\sqrt{2}\big(|1,0,1,2\rangle_1 + |0,1,2,1\rangle_1 + |1,0,1,2\rangle_2 + |0,1,2,1\rangle_2 \\
&+ |1,0,1,2\rangle_3 + |0,1,2,1\rangle_3 + |1,0,1,2\rangle_4 + |0,1,2,1\rangle_4\big) \\
&+ |1_1, 0, 1_2, 1_1 1_2\rangle + |1_2, 0, 1_1, 1_1 1_2\rangle + |0, 1_2, 1_1 1_2, 1_2\rangle + |0, 1_2, 1_1 1_2, 1_1\rangle \\
&+ |1_1, 0, 1_3, 1_1 1_3\rangle + |1_3, 0, 1_1, 1_1 1_3\rangle + |0, 1_1, 1_1 1_3, 1_3\rangle + |0, 1_3, 1_1 1_3, 1_1\rangle \\
&+ |1_1, 0, 1_4, 1_1 1_4\rangle + |1_4, 0, 1_1, 1_1 1_4\rangle + |0, 1_1, 1_1 1_4, 1_4\rangle + |0, 1_4, 1_1 1_4, 1_4\rangle \\
&+ |1_2, 0, 1_3, 1_2 1_3\rangle + |1_3, 0, 1_2, 1_2 1_3\rangle + |0, 1_2, 1_2 1_3, 1_3\rangle + |0, 1_3, 1_2 1_3, 1_2\rangle \\
&+ |1_2, 0, 1_4, 1_2 1_4\rangle + |1_4, 0, 1_2, 1_2 1_4\rangle + |0, 1_2, 1_2 1_4, 1_4\rangle + |0, 1_4, 1_2 1_4, 1_2\rangle \\
&+ |1_3, 0, 1_4, 1_3 1_4\rangle + |1_4, 0, 1_3 1_4, 1_3\rangle + |0, 1_3, 1_3 1_4, 1_4\rangle + |0, 1_4, 1_3 1_4, 1_4\rangle\Big] \\
&+ (1-p_T\eta)^2\lambda^2\Big[|0,0,2,2\rangle_1 + |0,0,2,2\rangle_2 + |0,0,2,2\rangle_3 + |0,0,2,2\rangle_4 \\
&+ |0, 0, 1_1 1_2, 1_1 1_2\rangle + |0, 0, 1_1 1_3, 1_1 1_3\rangle + |0, 0, 1_1 1_4, 1_1 1_4\rangle \\
&+ |0, 0, 1_2 1_3, 1_2 1_3\rangle + |0, 0, 1_2 1_4, 1_2 1_4\rangle + |0, 0, 1_3 1_4, 1_3 1_4\rangle\Big] \\
&+ (1-p_T\eta)\lambda\Big[|0,0,1,1\rangle_1 + |0,0,1,1\rangle_2 + |0,0,1,1\rangle_3 + |0,0,1,1\rangle_4\Big] \\
&+ |0,0,0,0\rangle + \mathcal{O}(\lambda^3)\Big\}
\end{aligned}
\tag{A2}
$$

This state is still normalised up to the truncation. We will now include the dark count probability via the mapping $|0\rangle \to \sqrt{p_{dark}}\,|click\rangle$ and we will subsequently post-select the cases in which at least one photon is detected at both sides. We model the use of non-number-resolving detectors and as such they cannot distinguish between single or multiple photon detections. We thus throw away the terms in which at least one side did not receive any photons, the heralding step can recognise that as an unsuccessful attempt. The state should be written as a density matrix as it involves a mixed state based on successful detection probabilities if we include this post-selection. We will nonetheless use the state ket notation for the convenience of writing such a large state. After the dark count probability has been added and the post-selection is done the state can be written as Eq. A3. After post-selection this state is no longer normalised, we will however, not care to do so since the normalisation will not be important for the fidelity calculation that we wish to perform (as it will be divided out when normalising). We will leave the states where a dark count provides the probability for a false successful detection unchanged since the real mapping is of no importance in our calculations. All erroneous terms together will later be viewed as one garbage state.

$$
\begin{aligned}
|\Psi\rangle_{A,B,l_A,l_B} =&(1-\lambda^2)^2\Big\{p_T\eta\lambda\Big[|1,1,0,0\rangle_1 + |1,1,0,0\rangle_2 + |1,1,0,0\rangle_3 + |1,1,0,0\rangle_4\Big] \\
&+ p_T^2\eta^2\lambda^2\Big[|2,2,0,0\rangle_1 + |2,2,0,0\rangle_2 + |2,2,0,0\rangle_3 + |2,2,0,0\rangle_4 \\
&+ |1_1 1_2, 1_1 1_2, 0, 0\rangle + |1_1 1_3, 1_1 1_3, 0, 0\rangle + |1_1 1_4, 1_1 1_4, 0, 0\rangle \\
&+ |1_2 1_3, 1_2 1_3, 0, 0\rangle + |1_2 1_4, 1_2 1_4, 0, 0\rangle + |1_3 1_4, 1_3 1_4, 0, 0\rangle\Big] \\
&+ \sqrt{p_T\eta(1-p_T\eta)}\lambda\sqrt{p_{dark}}\Big[|1,0,0,1\rangle_1 + |1,0,0,1\rangle_2 + |1,0,0,1\rangle_3 + |1,0,0,1\rangle_4
\end{aligned}
$$

$$
\begin{aligned}
&+ |0,1,1,0\rangle_1 + |0,1,1,0\rangle_2 + |0,1,1,0\rangle_3 + |0,1,1,0\rangle_4\Big] \\
&+ p_T\eta(1-p_T\eta)\lambda^2\Big[\sqrt{p_{dark}}(|2,0,0,2\rangle_1 + |0,2,2,0\rangle_1 + |2,0,0,2\rangle_2 + |0,2,2,0\rangle_2 \\
&+ |2,0,0,2\rangle_3 + |0,2,2,0\rangle_3 + |2,0,0,2\rangle_4 + |0,2,2,0\rangle_4 \\
&+ |1_1 1_2,0,0,1_1 1_2\rangle + |0,1_1 1_2,1_1 1_2,0\rangle + |1_1 1_3,0,0,1_1 1_3\rangle + |0,1_1 1_3,1_1 1_3,0\rangle \\
&+ |1_1 1_4,0,0,1_1 1_4\rangle + |0,1_1 1_4,1_1 1_4,0\rangle + |1_2 1_3,0,0,1_2 1_3\rangle + |0,1_2 1_3,1_2 1_3,0\rangle \\
&+ |1_2 1_4,0,0,1_2 1_4\rangle + |0,1_2 1_4,1_2 1_4,0\rangle + |1_3 1_4,0,0,1_3 1_4\rangle + |0,1_3 1_4,1_3 1_4,0\rangle) \\
&+ 2\big(|1,1,1,1\rangle_1 + |1,1,1,1\rangle_2 + |1,1,1,1\rangle_3 + |1,1,1,1\rangle_4\big) \\
&+ |1_1,1_1,1_2,1_2\rangle + |1_1,1_2,1_2,1_1\rangle + |1_2,1_1,1_1,1_2\rangle + |1_2,1_2,1_1,1_1\rangle \\
&+ |1_1,1_1,1_3,1_3\rangle + |1_1,1_3,1_3,1_1\rangle + |1_3,1_1,1_1,1_3\rangle + |1_3,1_3,1_1,1_1\rangle \\
&+ |1_1,1_1,1_4,1_4\rangle + |1_1,1_4,1_4,1_1\rangle + |1_4,1_1,1_1,1_4\rangle + |1_4,1_4,1_1,1_1\rangle \\
&+ |1_2,1_2,1_3,1_3\rangle + |1_2,1_3,1_3,1_2\rangle + |1_3,1_2,1_2,1_3\rangle + |1_3,1_3,1_2,1_2\rangle \\
&+ |1_2,1_2,1_4,1_4\rangle + |1_2,1_4,1_4,1_2\rangle + |1_4,1_2,1_2,1_4\rangle + |1_4,1_4,1_2,1_2\rangle \\
&+ |1_3,1_3,1_4,1_4\rangle + |1_3,1_4,1_4,1_3\rangle + |1_4,1_3,1_3,1_4\rangle + |1_4,1_4,1_3,1_3\rangle\Big] \\
&+ p_T\eta\sqrt{p_T\eta(1-p_T\eta)}\lambda^2\Big[\sqrt{2}(|2,1,0,1\rangle_1 + |1,2,1,0\rangle_1 + |2,1,0,1\rangle_2 + |1,2,1,0\rangle_2 \\
&+ |2,1,0,1\rangle_3 + |1,2,1,0\rangle_3 + |2,1,0,1\rangle_4 + |1,2,1,0\rangle_4) \\
&+ |1_1 1_2,1_1,0,1_2\rangle + |1_1 1_2,1_2,0,1_1\rangle + |1_1,1_1 1_2,1_2,0\rangle + |1_2,1_1 1_2,1_1,0\rangle \\
&+ |1_1 1_3,1_1,0,1_3\rangle + |1_1 1_3,1_3,0,1_1\rangle + |1_1,1_1 1_3,1_3,0\rangle + |1_3,1_1 1_3,1_1,0\rangle \\
&+ |1_1 1_4,1_1,0,1_4\rangle + |1_1 1_4,1_4,0,1_1\rangle + |1_1,1_1 1_4,1_4,0\rangle + |1_4,1_1 1_4,1_1,0\rangle \\
&+ |1_2 1_3,1_2,0,1_3\rangle + |1_2 1_3,1_3,0,1_2\rangle + |1_2,1_2 1_3,1_3,0\rangle + |1_3,1_2 1_3,1_2,0\rangle \\
&+ |1_2 1_4,1_2,0,1_4\rangle + |1_2 1_4,1_4,0,1_2\rangle + |1_2,1_2 1_4,1_4,0\rangle + |1_4,1_2 1_4,1_2,0\rangle \\
&+ |1_3 1_4,1_3,0,1_4\rangle + |1_3 1_4,1_4,0,1_3\rangle + |1_3,1_3 1_4,1_4,0\rangle + |1_4,1_3 1_4,1_3,0\rangle\Big] \\
&+ \sqrt{p_T\eta(1-p_T\eta)}(1-p_T\eta)\lambda^2\sqrt{p_{dark}}\Big[\sqrt{2}\big(|1,0,1,2\rangle_1 + |0,1,2,1\rangle_1 + |1,0,1,2\rangle_2 \\
&+ |0,1,2,1\rangle_2 + |1,0,1,2\rangle_3 + |0,1,2,1\rangle_3 + |1,0,1,2\rangle_4 + |0,1,2,1\rangle_4\big) \\
&+ |1_1,0,1_2,1_1 1_2\rangle + |1_2,0,1_1,1_1 1_2\rangle + |0,1_2,1_1 1_2,1_2\rangle + |0,1_2,1_1 1_2,1_1\rangle \\
&+ |1_1,0,1_3,1_1 1_3\rangle + |1_3,0,1_1,1_1 1_3\rangle + |0,1_1,1_1 1_3,1_3\rangle + |0,1_3,1_1 1_3,1_1\rangle \\
&+ |1_1,0,1_4,1_1 1_4\rangle + |1_4,0,1_1,1_1 1_4\rangle + |0,1_1,1_1 1_4,1_4\rangle + |0,1_4,1_1 1_4,1_4\rangle \\
&+ |1_2,0,1_3,1_2 1_3\rangle + |1_3,0,1_2,1_2 1_3\rangle + |0,1_2,1_2 1_3,1_3\rangle + |0,1_3,1_2 1_3,1_2\rangle \\
&+ |1_2,0,1_4,1_2 1_4\rangle + |1_4,0,1_2,1_2 1_4\rangle + |0,1_2,1_2 1_4,1_4\rangle + |0,1_4,1_2 1_4,1_2\rangle \\
&+ |1_3,0,1_4,1_3 1_4\rangle + |1_4,0,1_3 1_4,1_3\rangle + |0,1_3,1_3 1_4,1_4\rangle + |0,1_4,1_3 1_4,1_4\rangle\Big] \\
&+ (1-p_T\eta)^2\lambda^2 p_{dark}\Big[|0,0,2,2\rangle_1 + |0,0,2,2\rangle_2 + |0,0,2,2\rangle_3 + |0,0,2,2\rangle_4 \\
&+ |0,0,1_1 1_2,1_1 1_2\rangle + |0,0,1_1 1_3,1_1 1_3\rangle + |0,0,1_1 1_4,1_1 1_4\rangle \\
&+ |0,0,1_2 1_3,1_2 1_3\rangle + |0,0,1_2 1_4,1_2 1_4\rangle + |0,0,1_3 1_4,1_3 1_4\rangle\Big] \\
&+ (1-p_T\eta)\lambda p_{dark}\Big[|0,0,1,1\rangle_1 + |0,0,1,1\rangle_2 + |0,0,1,1\rangle_3 + |0,0,1,1\rangle_4\Big] \\
&+ p_{dark}\,|0,0,0,0\rangle + \mathcal{O}(\lambda^3)\Big\}
\end{aligned}
\tag{A3}
$$

Now we have modelled the state that we could expect to receive at the detectors without incorporating the mapping to the qubit memory register and the QFT. To address this we will trace out the loss channels and extract the part of the state that represents the desired Bell state together with its probability amplitude. We can do this since for calculating the fidelity we only care about the desired

state and we can view everything else as an erroneous state. For our fidelity calculation, we can thus use only the desired part to map it to the qubit memory register and subsequently perform the QFT and the X-measurement. We start with the part of the state that we want to receive:

$$|\Psi\rangle_0 = \eta p_T \lambda (1-\lambda^2)^2 (|1,1\rangle_1 + |1,1\rangle_2 + |1,1\rangle_3 + |1,1\rangle_4). \tag{A4}$$

Now we can map this qudit state to the qubit memories, using the following mapping:

$$\begin{aligned} |1\rangle &\longrightarrow |00\rangle \\ |2\rangle &\longrightarrow |01\rangle \\ |3\rangle &\longrightarrow |10\rangle \\ |4\rangle &\longrightarrow |11\rangle \end{aligned} \tag{A5}$$

We will find the following state:

$$|\Psi\rangle_0 \longrightarrow \eta p_T \lambda (1-\lambda^2)^2 [\, |1,1\rangle_1 |00,00\rangle + |1,1\rangle_2 |01,01\rangle + |1,1\rangle_3 |10,10\rangle + |1,1\rangle_4 |11,11\rangle \,] \tag{A6}$$

Both sides of the protocol receive we same state, so we can compute the QFT for one side and derive the full state from there. The QFT will result in the following mapping:

$$\begin{aligned} |1\rangle \rightarrow &\quad \frac{1}{\sqrt{4}}(|X_1\rangle + |X_2\rangle + |X_3\rangle + |X_4\rangle) \\ |2\rangle \rightarrow &\quad \frac{1}{\sqrt{4}}(|X_1\rangle + e^{-2\pi i/4}|X_2\rangle + e^{-4\pi i/4}|X_3\rangle + e^{-6\pi i/4}|X_4\rangle) \\ |3\rangle \rightarrow &\quad \frac{1}{\sqrt{4}}(|X_1\rangle + e^{-4\pi i/4}|X_2\rangle + e^{-8\pi i/4}|X_3\rangle + e^{-12\pi i/4}|X_4\rangle) \\ |4\rangle \rightarrow &\quad \frac{1}{\sqrt{4}}(|X_1\rangle + e^{-6\pi i/4}|X_2\rangle + e^{-12\pi i/4}|X_3\rangle + e^{-18\pi i/4}|X_4\rangle) \end{aligned} \tag{A7}$$

By applying this mapping we can find the state after the QFT to be given as:

$$\begin{aligned} &\eta p_T \lambda (1-\lambda^2)^2 [\, |1,1\rangle_1 |00,00\rangle + |1,1\rangle_2 |01,01\rangle + |1,1\rangle_3 |10,10\rangle + |1,1\rangle_4 |11,11\rangle \,] \rightarrow \\ &\frac{\eta p_T \lambda (1-\lambda^2)^2}{4} [(|X_1\rangle + |X_2\rangle + |X_3\rangle + |X_4\rangle) \otimes (|X_1\rangle + |X_2\rangle + |X_3\rangle + |X_4\rangle) |00,00\rangle \\ &+ (|X_1\rangle + e^{-i\pi/2}|X_2\rangle + e^{-2i\pi/2}|X_3\rangle + e^{-3i\pi/2}|X_4\rangle) \otimes (|X_1\rangle + e^{-i\pi/2}|X_2\rangle + e^{-2i\pi/2}|X_3\rangle \\ &+ e^{-3i\pi/2}|X_4\rangle) |01,01\rangle + (|X_1\rangle + e^{-2i\pi/2}|X_2\rangle + e^{-4i\pi/2}|X_3\rangle + e^{-6i\pi/2}|X_4\rangle) \otimes (|X_1\rangle + e^{-2i\pi/2}|X_2\rangle \\ &+ e^{-4i\pi/2}|X_3\rangle + e^{-6i\pi/2}|X_4\rangle) |10,10\rangle + (|X_1\rangle + e^{-3i\pi/2}|X_2\rangle + e^{-6i\pi/2}|X_3\rangle + e^{-9i\pi/2}|X_4\rangle) \otimes (|X_1\rangle \\ &+ e^{-3i\pi/2}|X_2\rangle + e^{-6i\pi/2}|X_3\rangle + e^{-9i\pi/2}|X_4\rangle) |11,11\rangle \,] \end{aligned} \tag{A8}$$

We will now measure in the generalised X-basis on both sides to herald the arrival of a photon. If we then measure $|X_k\rangle_A \otimes |X_l\rangle_B$ we will find that the desired state has collapsed to the following state:

$$\begin{aligned} |\Psi\rangle_0 = \eta p_T \lambda (1-\lambda^2)^2 (&|00,00\rangle + e^{-ik\pi/2} e^{-il\pi/2} |01,01\rangle \\ &+ e^{-2ik\pi/2} e^{-2il\pi/2} |10,10\rangle + e^{-3ik\pi/2} e^{-3il\pi/2} |11,11\rangle) \end{aligned} \tag{A9}$$

If we know k and l we can then correct for the phases with single qubit RZ-gates.

If we thus measure the qudit at Alice and Bob after the QFT and correct for the phases we find.

$$\eta p_T \lambda (1-\lambda^2)^2 (|00\rangle_A |00\rangle_B + |01\rangle_A |01\rangle_B + |10\rangle_A |10\rangle_B + |11\rangle_A |11\rangle_B) \tag{A10}$$

This can be rewritten to:

$$\eta p_T \lambda (1-\lambda^2)^2 (|0\rangle_{A1}|0\rangle_{B1} + |1\rangle_{A1}|1\rangle_{B1}) \otimes (|0\rangle_{A2}|0\rangle_{B2} + |1\rangle_{A2}|1\rangle_{B2}) \tag{A11}$$

To calculate the average fidelity of the two entangled pairs we can trace out one of the pairs and calculate the fidelity of a single pair due to the symmetry. We can use Eq. 2.4 to calculate the fidelity but we will need to normalise the equation by dividing by the total weight of probability amplitudes considered in the calculation.

$$F_{A_1,B_1} = \frac{\langle\phi^+| Tr_{A_2,B_2}(\rho_{final}) |\phi^+\rangle}{Tr(\rho_{total})} \tag{A12}$$

We use the density matrix of the state that we found, which is given by:

$$\begin{aligned}
\rho_{A1A2B1B2,final} =& \eta^2 p_T^2 \lambda^2 (1-\lambda^2)^4 \big\{ |0000\rangle\langle 0000| + |0000\rangle\langle 0101| \\
&+ |0000\rangle\langle 1010| + |0000\rangle\langle 1111| \\
&+ |0101\rangle\langle 0000| + |0101\rangle\langle 0101| \\
&+ |0101\rangle\langle 1010| + |0101\rangle\langle 1111| \\
&+ |1010\rangle\langle 0000| + |1010\rangle\langle 0101| \\
&+ |1010\rangle\langle 1010| + |1010\rangle\langle 1111| \\
&+ |1111\rangle\langle 0000| + |1111\rangle\langle 0101| \\
&+ |1111\rangle\langle 1010| + |1111\rangle\langle 1111| \big\}
\end{aligned} \tag{A13}$$

$$\begin{aligned}
Tr_{A_2,B_2}(\rho) = \rho_{A_1,B_1} =& \sum_{i,j} (I_{A_1} \otimes I_{B_1} \otimes \langle i|_{A_2} \langle j|_{B_2}) \rho (I_{A_1} \otimes I_{B_1} |i\rangle_{A_2} |j\rangle_{B_2}) \\
=& \eta^2 p_T^2 \lambda^2 (1-\lambda^2)^4 (2|00\rangle\langle 00| + 2|00\rangle\langle 11| + 2|11\rangle\langle 00| + 2|11\rangle\langle 11|)
\end{aligned} \tag{A14}$$

Up till now, we have not considered decoherence yet in our calculation. Since we only consider decoherence in the memories we can apply the depolarising channel given by Eq. 2.27 to our state to arrive at the following equation:

$$\langle\phi^+| \bar{\rho} |\phi^+\rangle = 2\alpha[(p_1 + (1-p_1)\epsilon_1)(p_2 + (1-p_2)\epsilon_1) + (1-p_1)(1-p_2)(\epsilon_x^2 + \epsilon_y^2 + \epsilon_z^2)] \tag{A15}$$

Since the depolarising channel is trace preserving the trace over the full density matrix considered will remain the same. From equation A3 we can find the normalisation of the fidelity, representing the success probability.

$$\begin{aligned}
Tr(\rho_{total}) =& (1-\lambda^2)^4 \Big\{ 4p_T^2\eta^2\lambda^2 + 10p_T^4\eta^4\lambda^4 + 8\lambda^2 p_T\eta(1-p_T\eta)p_{dark} \\
&+ p_T^2\eta^2(1-p_T\eta)^2\lambda^4 \Big(20p_{dark} + 40\Big) \\
&+ 40p_T^3\eta^3(1-p_T\eta)\lambda^4 + 40p_T\eta(1-p_T\eta)^3\lambda^4 p_{dark} \\
&+ p_{dark}^2 \Big(10(1-p_T\eta)^4\lambda^4 + 4(1-p_T\eta)^2\lambda^2 + 1\Big) + \mathcal{O}(\lambda^6) \Big\}
\end{aligned} \tag{A16}$$

From equation 1.8 we can now find the fidelity as the fraction of the previous two equations.

$$
\begin{aligned}
F_{A_1,B_1} =& 4\eta^2 p^2 \lambda^2 ((p_1 + (1-p_1)\epsilon_1)(p_2 + (1-p_2)\epsilon_1) + (1-p_1)(1-p_2)(\epsilon_x^2 + \epsilon_y^2 + \epsilon_z^2))/ \\
& \Big\{ 4p^2\lambda^2\eta^2 + 10p^4\lambda^4\eta^4 + 8\lambda^2 p\eta(1-p\eta)p_{dark} \\
& + p^2\eta^2(1-p\eta)^2\lambda^4\Big(20p_{dark} + 40\Big) \\
& + 40p^3\eta^3(1-p\eta)\lambda^4 + 40p\eta(1-p\eta)^3\lambda^4 p_{dark} \\
& + p_{dark}^2\Big(10(1-p\eta)^4\lambda^4 + 4(1-p\eta)^2\lambda^2 + 1\Big) + \mathcal{O}(\lambda^6)\Big\} \\
=& 4\eta^2 p^2 \lambda^2 ((e^{-t/T_1} + (1-e^{-t/T_1})\epsilon_1)(e^{-t/T_2} + (1-e^{-t/T_2})\epsilon_1) \\
& + (1-e^{-t/T_1})(1-e^{-t/T_2})(\epsilon_x^2 + \epsilon_y^2 + \epsilon_z^2))/ \\
& \Big\{ 4p^2\lambda^2\eta^2 + 10p^4\lambda^4\eta^4 + 8\lambda^2 p\eta(1-p\eta)p_{dark} \\
& + p^2\eta^2(1-p\eta)^2\lambda^4\Big(20p_{dark} + 40\Big) \\
& + 40p^3\eta^3(1-p\eta)\lambda^4 + 40p\eta(1-p\eta)^3\lambda^4 p_{dark} \\
& + p_{dark}^2\Big(10(1-p\eta)^4\lambda^4 + 4(1-p\eta)^2\lambda^2 + 1\Big) + \mathcal{O}(\lambda^6)\Big\}
\end{aligned}
\tag{A17}
$$

Appendix 2 Pseudo-code

Here, a pseudo-code used for modelling the high-dimensional entanglement protocol is presented. This serves as a quick guide to how the code works and as an overview of the protocol.

Algorithm 1 Rate versus Distance

Input: $m, n_p, \eta, p_{dark}, t_{rep}, M, T_d$, distances, p_T at each distance, fidelity threshold, precision
Initialise list of rates at each distance all set to 0
for every distance **do**
    Find corresponding heralding time
    Calculate the average fidelity for each $\lambda \in (0, 0.1)$
    if fidelity $>$ threshold **then**
        Find the greatest value of λ that satisfies the condition
        Calculate rate for this λ and replace corresponding value in rate list
    else
        Leave rate value set to 0
    end if
end for
Return List of rates corresponding to each distance

For the full code including all functions describing how to calculate the average fidelity and rate see: https://github.com/mcalvind/Master_Thesis_Calvin_Dijksman.

Appendix 3 List of parameters

Finally we present the table of distances with their corresponding transmission probabilities used in our simulations in Table A1. These can all be recovered by running the full code that can be found online.

Table A1: Table with the values of p_T corresponding to the distances used in the simulations. These values were calculated using the analytical model from Ref. [21] with a Low Earth Orbit satellite at a height of 400 km.

Distance (km)	p_T
202.3748	0.019197
246.0651	0.018753
289.7554	0.018258
333.4458	0.017714
377.1361	0.017131
420.8265	0.016504
464.5168	0.015842
508.2071	0.015143
551.8975	0.014405
595.5878	0.013642
639.2782	0.012849
682.9685	0.012039
726.6588	0.011209
770.3492	0.010373
814.0395	0.009534
857.7299	0.008707
901.4202	0.007895
945.1105	0.007117
988.8009	0.006372
1032.491	0.005682
1076.182	0.00504
1119.872	0.004442
1163.562	0.003894
1207.253	0.003388
1250.943	0.00293

Furthermore, we provide an unordered list of important parameters encountered in this thesis, which is presented in Table A2.

Table A2: Non-ordered list of many of the important recurring parameters in this thesis.

Parameter	Description
m	Dimensionality of 2^m-dimensional qudit
n_p	Number of desired entangled pairs
M	Number of times that we multiplex
N	Number of entanglement generation units in parallel scheme
D	Number of entanglement generation units after applying multiplexing
p_{suc}	Success probability of the heralded pair
p_{ent}	Success probability including the steady-state probability of the detectors
p_{approx}	Sum of probability weights considered in our approximations
$\pi_{(0,0)}$	Probability for the detectors to be open
τ_c	Period of qudit formation ($2^m \tau_{rep}$)
τ_h	Heralding time between the two ground stations
τ_{rep}	Repetition period of the source
L	Distance between the two ground stations
c	Speed of light ($2.998 \cdot 10^8$ m/s)
p_T	Transmission probability
η	Detector efficiency
p_{dark}	Dark count probability
λ	Squeezing parameter of the SPDC source
T_d	Coherence time of the qubit memories
$\langle n \rangle$	Average number of trials needed for culmination of the protocol
ϵ_1	Pauli error rate in I basis
ϵ_X	Pauli error rate in X basis
ϵ_Y	Pauli error rate in Y basis
ϵ_Z	Pauli error rate in Z basis